INTERIM
IN-92-CR
OCIT
198226
103 P

Science Applications International Corporation

An Employee-Owned Company

SAIC-93/1224:APPAT-158
16 December 1993

SECOND YEAR PROGRESS REPORT

DETERMINATION OF CORONAL MAGNETIC FIELDS FROM VECTOR MAGNETOGRAMS

Science Applications International Corporation
An Employee-Owned Company

Second year progress report on work performed under contract
NASW-4728
with NASA (Solar Physics Supporting Research and Technology)

ZORAN MIKIĆ, Principal Investigator

10260 Campus Point Drive, San Diego, California 92121 (619) 546-6000
Other SAIC Offices: Albuquerque, Boston, Colorado Springs, Dayton, Huntsville, Las Vegas, Los Angeles, McLean, Oak Ridge, Orlando, Palo Alto, Seattle, and Tucson

1. INTRODUCTION

This report covers technical progress during the second year of the contract entitled "Determination of Coronal Magnetic Fields from Vector Magnetograms," NASW-4728, between NASA and Science Applications International Corporation, and covers the period January 1, 1993 to December 31, 1993. Under this contract SAIC has conducted research into the determination of coronal magnetic fields from vector magnetograms, including the development and application of algorithms to determine force-free coronal fields above selected observations of active regions. The contract began on June 30, 1992 and has a completion date of December 31, 1994. This contract is a continuation of work started in a previous contract, NASW-4571, which covered the period November 15, 1990 to December 14, 1991.

During this second year we have concentrated on studying additional active regions and in using the estimated coronal magnetic fields to compare to coronal features inferred from observations. The following is a summary of our research during the past year:

- We have redone the force-free field (FFF) fit to active region 5747 on October 20, 1989 using the (new) non-periodic version of the code;
- We have documented the coronal field structure of AR5747 and compared it to the morphology of footpoint emission in a flare, showing that the "high-pressure" Hα footpoints are connected by coronal field lines (Mikić & McClymont 1994);
- We have shown that the variation of magnetic field strength along current-carrying field lines is significantly different from the variation in a potential field, and that the resulting near-constant area of elementary flux tubes is consistent with observations of coronal loop in soft X-rays (McClymont & Mikić 1994);
- We applied the evolutionary technique to an exact analytic force-free field of Low and Lou (1990), showing that the scheme converges when data for an exact field is supplied (Mikić & Barnes 1994);
- We generated realistic models of force-free fields which model active regions. These models will be used to study the performance of the evolutionary technique to measurement errors and inconsistencies in the data, as well as to study the effect of photospheric shear on active regions, and their possible role as flare triggers (Mikić 1993).
- We deduced coronal fields for two additional vector magnetograms, of AR6919 on 15 November, 1991, and of AR7260 on 18 August, 1992. These regions had coincident soft X-ray Yohkoh observations.
- In conjunction with an NSF-funded grant, we studied the theoretical properties of an arcade field in spherical geometry. We found that photospheric shear can lead to magnetic nonequilibrium, causing an

arcade to disrupt. This effect may explain how coronal mass ejections are initiated (Mikić & Linker 1994).

During this year we have presented our research results at the following scientific meetings, workshops, and seminars: Seminar at the University of Hawaii, April 1994; Invited talk at the Physics Computing `93 Conference, Albuquerque, June, 1993; Talk and Poster at the AAS/Solar Physics Division, Palo Alto, July, 1993; Invited talk at the Gordon Conference, Plymouth, New Hampshire, August 1993; Talk at the Sacramento Peak Workshop on Active Region Evolution, Sunspot, August/September, 1993; Invited talk at the American Geophysical Union Conference, San Francisco, December 1993.

All the vector magnetograms used so far have been obtained at Mees Solar Observatory (MSO) of the University of Hawaii using the Haleakala Stokes Polarimeter. This project has benefited tremendously from cooperation with the staff of the Institute for Astronomy, University of Hawaii. Dr. Alexander McClymont has been our point-of-contact and principal collaborator during this project.

Section 2 of this report contains an brief account of progress during the research performed under this contract. Section 3 contains the proposed statement of work for the third year of the project.

2. TECHNICAL PROGRESS

2.1 Active region 5747 on October 20, 1989

As described in last year's progress report, we have developed a non-periodic version of the computer code which implements the evolutionary technique. This represents a major advance in the realism with which we can model the coronal magnetic field. Previously, for numerical convenience, we had assumed that the transverse dimensions (the x–y plane, which is parallel to the photosphere) were periodic. We have been able to remove this constraint by using a more sophisticated numerical algorithm. We have redone our estimate of the coronal field for AR5747 using this new code. The analysis described below is based on this improved estimate.

2.2 The Coronal Field above AR5747: Comparison with Observations

We have made use of the coronal field computed from the magnetogram of AR5747 in two studies of relevance to flare and active-region physics. First, we compare the connectivity implied by the coronal field with Hα data obtained at Mees Solar Observatory (University of Hawaii) during an M2 flare (Leka *et al.* 1993) which occurred 3 hours after the magnetogram scan was completed. Secondly, we studied the area variation along current-carrying elementary flux tubes, and showed that the presence of current in the corona can account for the observed constant thickness of soft X-ray loops (McClymont & Mikić 1994).

Figure 1 shows observed Hα flare features superimposed on the magnetogram of AR5747. The three small pseudo-circular features in Fig. 1(*a*) enclose areas in which specific Hα signatures were detected. The small feature on the neutral line at position (3.0,5.0) showed the signature of particle precipitation and coincided temporally with hard X-ray emission. Figs. 1(*b*) and (*c*) (refer to the caption) show that the footpoints of a coronal loop in the estimated force-free coronal field are in much closer agreement with the observed high-pressure regions than footpoints of a loop in the potential magnetic field (Mikić & McClymont 1994).

It is unfortunate that there are no soft X-ray observations of AR5747 to confirm the existence of a high-pressure coronal loop joining the Hα footpoints. However, we have made use of this dataset in a generic way, by examining the variation of cross-sectional area along elementary flux tubes which carry substantial currents through the corona [principally from the positive spot at (3,4) to the negative spot at (6,8) in Figure 1(*a*)], and comparing the results with recent soft X-ray observations. Since the Skylab era it has been noted that images of coronal loops seen in soft X-rays or extreme ultraviolet emission appear to be of remarkably uniform thickness, a result recently confirmed by high-resolution observations (Golub 1991; Klimchuk *et al.* 1992). If the emitting volume outlines a bundle of field lines, or flux tube, the implication is that the magnetic field does

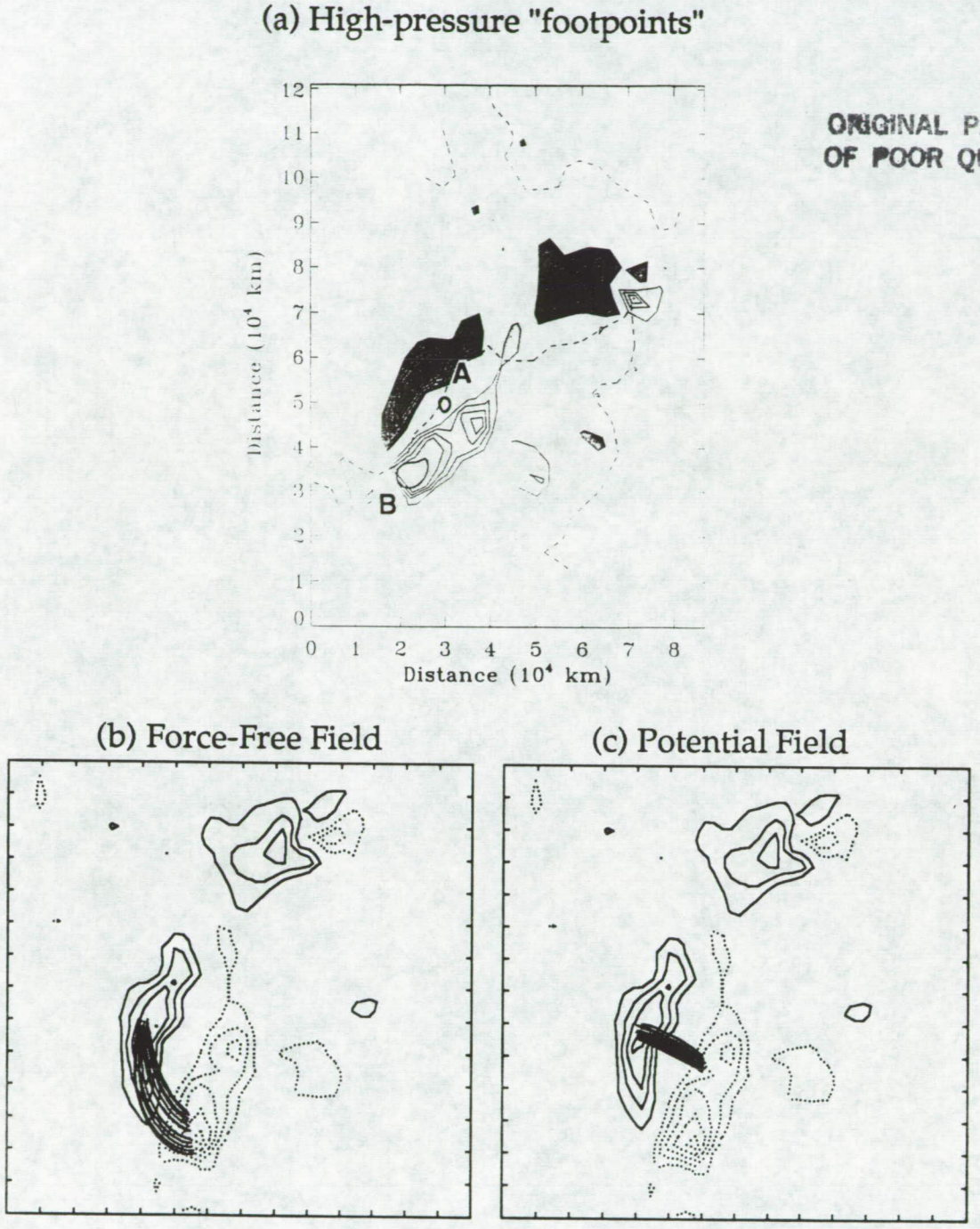

Figure 1.—(*a*) Hα flare features superimposed on the magnetogram of AR5747 (from Leka *et al.* 1993). The neutral line is marked by a broken line; regions of strong vertical current are shown as shaded contours, and the three small pseudo-circular features enclose areas in which specific Hα signatures were detected. The features marked "A" at position (2.9,5.6) and "B" at (2.2,3.4) mark sites of high pressure "footpoints." (*b*) Field line traces in the estimated *force-free* coronal field, showing that the high-pressure sites A and B are close to the footpoints of a coronal loop. (*c*) Field line traces in the *potential* coronal field, with the same initial footpoint positions (at A) as in (*b*), showing that the agreement between the high-pressure sites and coronal loop footpoints is much better for the estimated force-free field than for a potential field. The contours in (*b*) and (*c*) show the vertical current density in the photosphere.

not expand in height as it would if the field were potential. Recently Klimchuk *et al.* (1992) have quantified this characteristic, finding for several loops observed by the Soft X-ray Telescope on the Yohkoh spacecraft a thickness variation along their lengths of only 10–20%. We have demonstrated that this observation is consistent with the characteristics of current-carrying field lines in a highly sheared active region. By tracing field lines in the computed coronal field for AR5747 we have shown that magnetic loops which are highly sheared do not expand rapidly in height, as they would in a potential field (McClymont & Mikić 1994; this preprint is attached in Appendix A).

2.3 Low and Lou's Exact Force-Free Field

We have verified that the evolutionary technique can correctly estimate the coronal field when the boundary data corresponding to an analytic force-free field is used. The boundary data from the analytic force-free field of Low and Lou (1990) was used to specify B_z and J_z at $z = 0$ in the evolutionary technique, which was then used to estimate the coronal field. Figure 2 shows a comparison between the field lines in the analytic solution and those in the coronal field determined from the boundary data. This simulates the application of the evolutionary technique to a vector magnetogram, albeit to one with perfectly consistent data. The good agreement between the estimated coronal magnetic field and the analytic solution verifies that the evolutionary technique is based on a well-posed formulation (Mikić & Barnes 1994).

2.4 Realistic Force-Free Field Models of Active Regions

In order to study the effect of inconsistencies in the boundary data on the coronal field estimates obtained with the evolutionary algorithm, it is first necessary to create exact force-free coronal fields against which the estimates can be compared. We require models which have the properties of observed active region fields (complexity, no symmetries, compact flux and current distributions, three-dimensional variation). We have created an idealized model of a force-free field whose properties are similar to those of active region 5747 of 20 October 1989 (Mikić 1993). This solution will be used for the additional purpose of constructing a realistic model of an active region to study flare triggers.

We first construct a flux distribution $B_z(x,y)$ in the photosphere which captures the essential features seen in the vector magnetogram of AR5747. We construct the vertical flux B_z by superimposing four Gaussian distributions to match the two sunspots with negative flux and the one sunspot with positive flux; the net flux is zero. This flux distribution is used to compute a potential field in the corona. The flux distribution and the corresponding potential field lines are shown in Figure 3(*a*).

A force-free field was generated by subjecting this potential field to specified footpoint displacements. The dynamical MHD equations were solved using our 3D resistive MHD code. An equilibrium was found by introducing finite viscosity, a small amount of resistivity, and relaxing the field after the footpoints

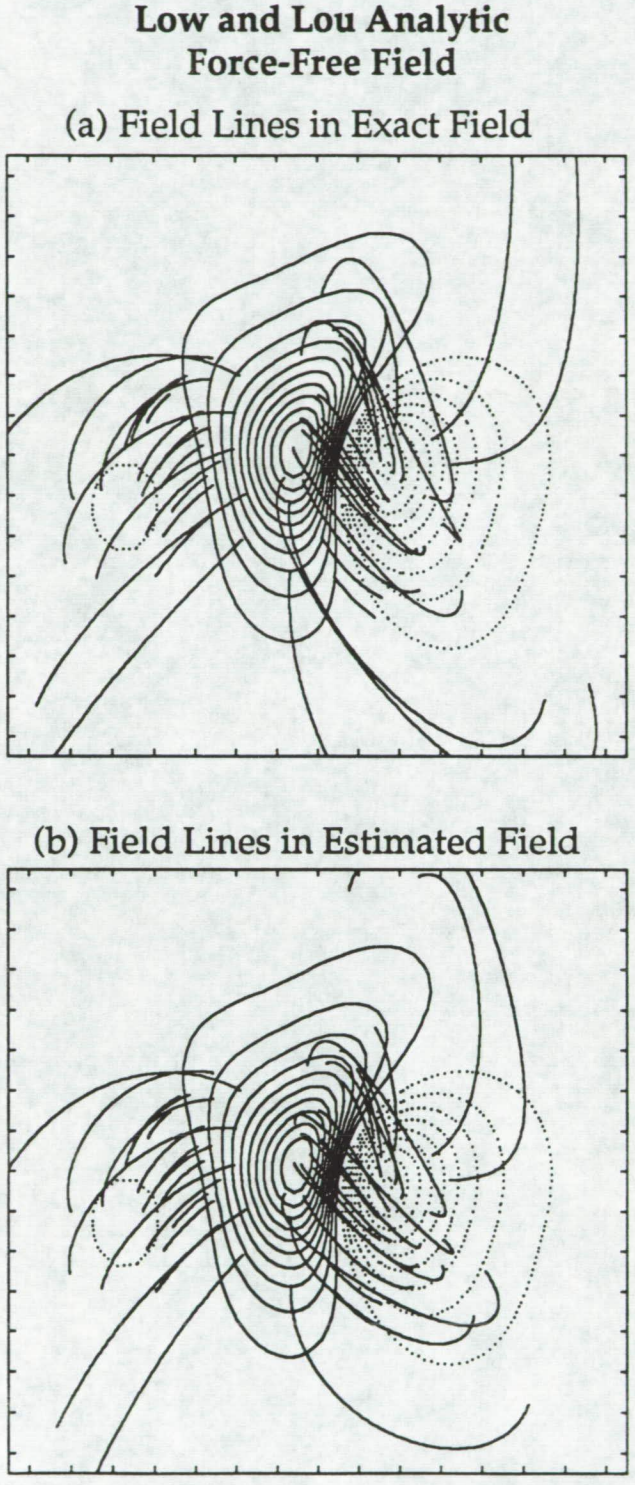

Figure 2.—Comparison between field lines in (*a*) the analytic force free field of Low & Lou (1990), and (*b*) the coronal field estimated using the evolutionary technique from the boundary data at $z = 0$. The contours show the vertical magnetic field. The good agreement shows that the evolutionary technique is based on a well-posed mathematical formulation.

of the field lines were displaced. The displacement was introduced by applying flow on the photospheric boundary (which was ramped on and off gradually). The choice of footpoint displacements (*i.e.*, the applied photospheric flow profile) was guided by the observed topology of the estimated coronal force-free field. We chose a flow profile to twist the fields in a manner which reproduced the observed global twist in the coronal field. Figure 3(*b*) shows the applied flow profile in the photosphere.

The resulting field relaxes to a force-free field with an energy that is 40% above that of the potential field, consistent with that estimated for AR5747. Figure 4 shows a comparison between the observed vector magnetogram data and the photospheric profiles from this model. The vertical current density profile J_z is remarkably similar to that deduced from the observations. In addition, the photospheric values of the transverse magnetic fields B_x and B_y are similar to those from the observations. Figure 5 shows the field lines for the model field and those for the estimated coronal field for AR5747. It is apparent that the global features seen in the model are similar to those observed in the data. This is therefore quite a realistic model of the field above an active region.

2.5 Active Region 6919 on 15 November, 1991

We have determined the coronal field above NOAA active region 6919 on 15 November, 1991, a region of intense interest with an extensive database of coincident Yohkoh and MSO observations. Figure 6 shows a projection of traces of the estimated coronal field above this active region, compared to the potential field. Note the complicated nature of this active region, which consists of several sunspots. The topology of the computed coronal field is consistent with the morphology deduced from soft and hard X-ray Yohkoh images during an X class flare at ~ 22:40 UT (McClymont & Mikić 1993)

2.6 Active Region 7260 on 18 August, 1992

We have determined the coronal field above NOAA active region 7260 on 18 August, 1992. This region was observed with Yohkoh as it made its transit across the solar disk during the period August 9–22. It was associated with several flares, and had evidence of emerging flux. This active region was the subject of intense coordinated study during a recent workshop in Hawaii (November 29–December 3, 1993). Our calculations of the coronal field were presented at this workshop.

Figure 7 shows a projection of traces of the estimated coronal field above this active region, compared to the potential field. Note that the field lines are significantly nonpotential.

2.7 Disruption of Coronal Magnetic Arcades

The ideal and resistive properties of isolated large-scale coronal magnetic arcades were studied using axisymmetric solutions of the time-dependent magnetohydrodynamic (MHD) equations in spherical geometry. We examined

(a) Potential Magnetic Field Lines

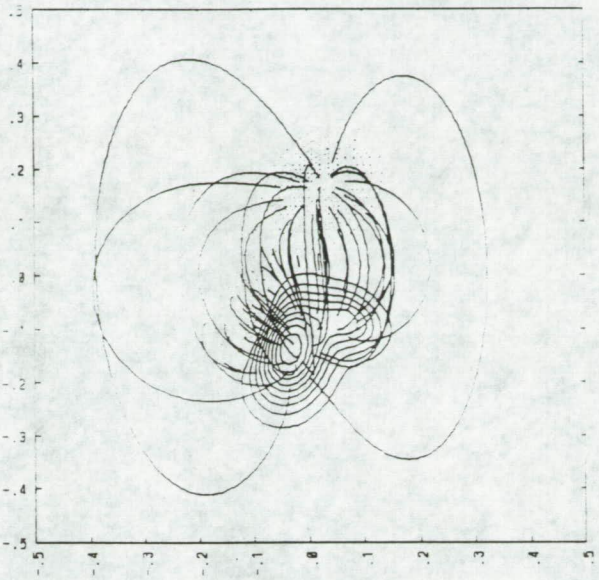

(b) Applied Photospheric Flow

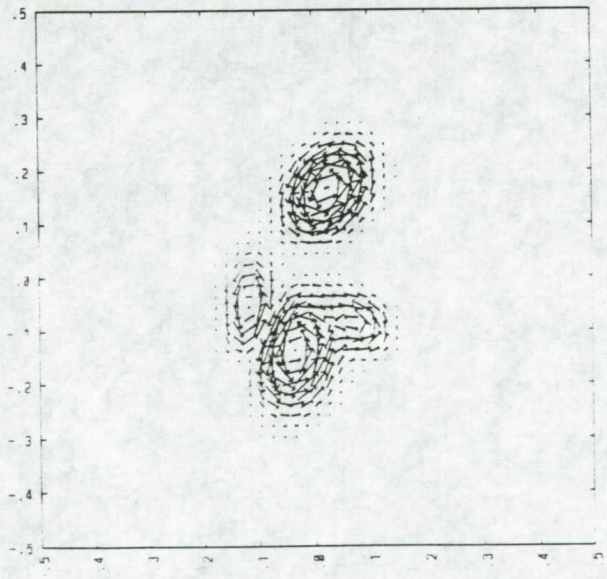

Figure 3.—(a) Contours of the vertical magnetic field $B_z(x,y)$ in the photosphere $z = 0$, with traces of the potential magnetic field lines for an idealized model of an active region. (b) Projection of the transverse photospheric shear velocity that is applied to the magnetic field footpoints at $z = 0$ in (a) to create a force-free field.

A Model Force-Free Field Matching Magnetic Fields Measured with a Vector Magnetograph

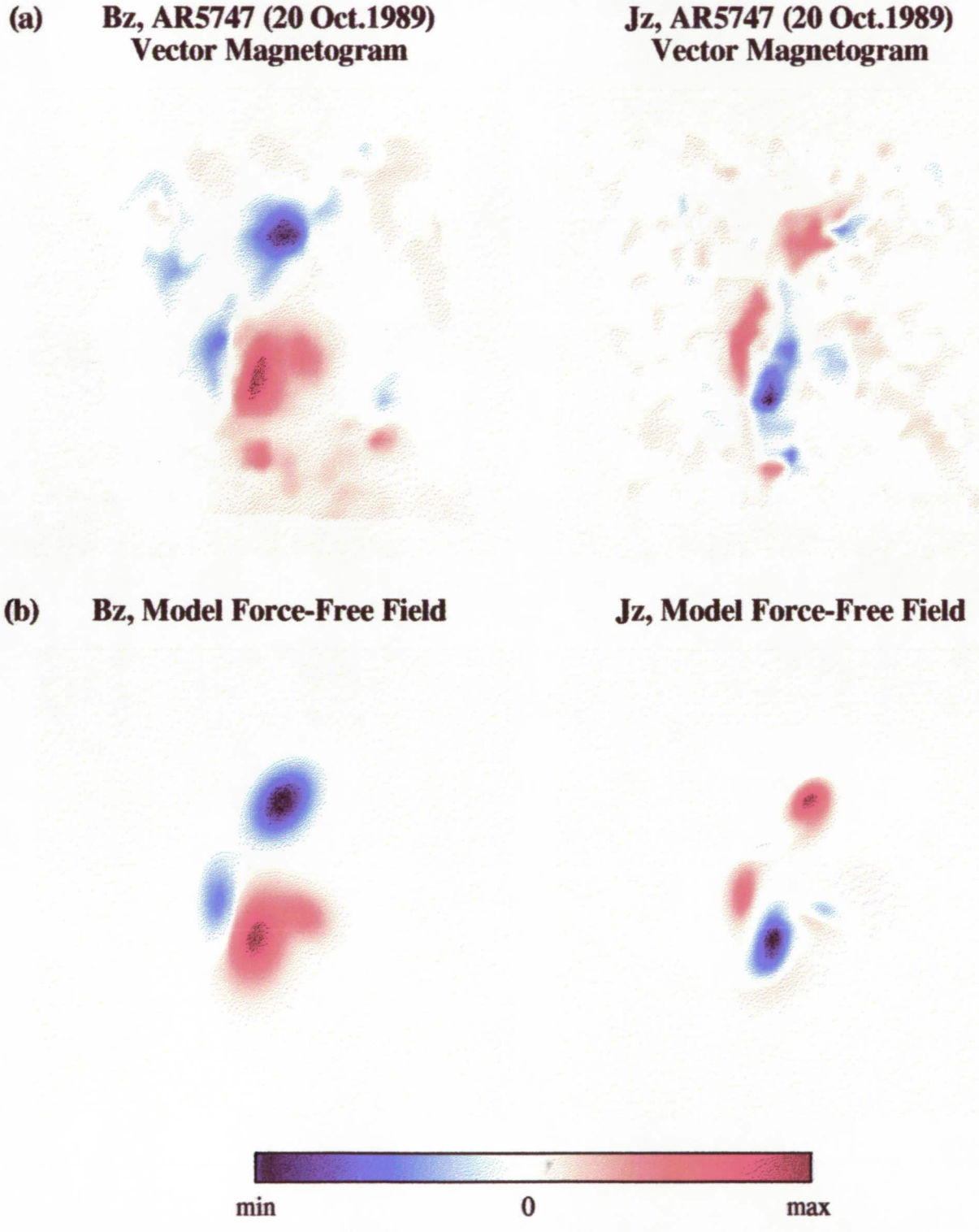

Figure 4.—Comparison of the normal magnetic field and current density at $z = 0$ between (*a*) the vector magnetogram of AR5747 on 20 October 1989 and (*b*) an idealized force-free field model. The similarity between the main features in the magnetogram and the model indicate that this is a realistic model of an active region.

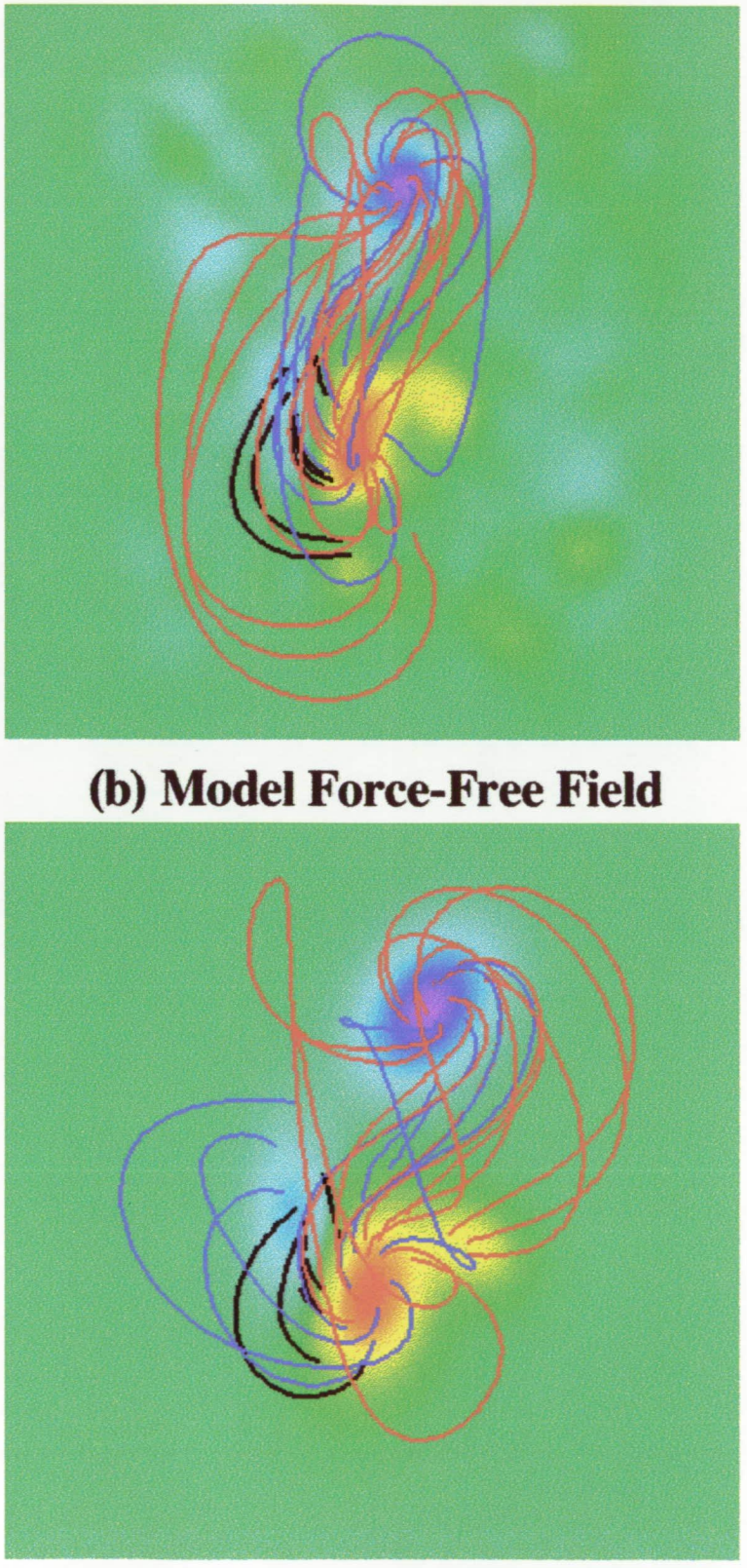

Figure 5.—Traces of the field lines in (*a*) the estimated coronal field of active region 5747, and (*b*) the idealized force-free model of this active region. Note that the model field is qualitatively similar to the field of AR5747.

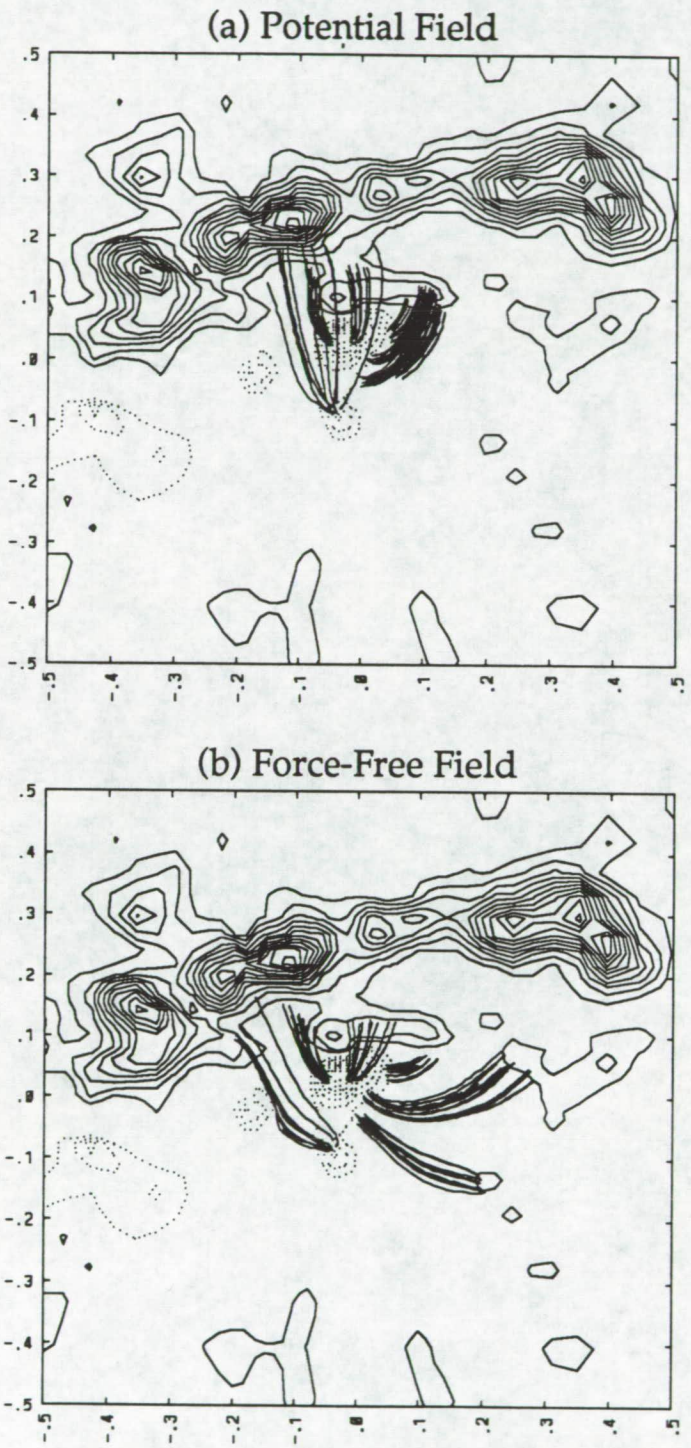

Figure 6.—Traces of the field lines in (*a*) the potential coronal field of active region 6919 on 15 November, 1991, and (*b*) the estimated force-free field as determined from a vector magnetogram of this region.

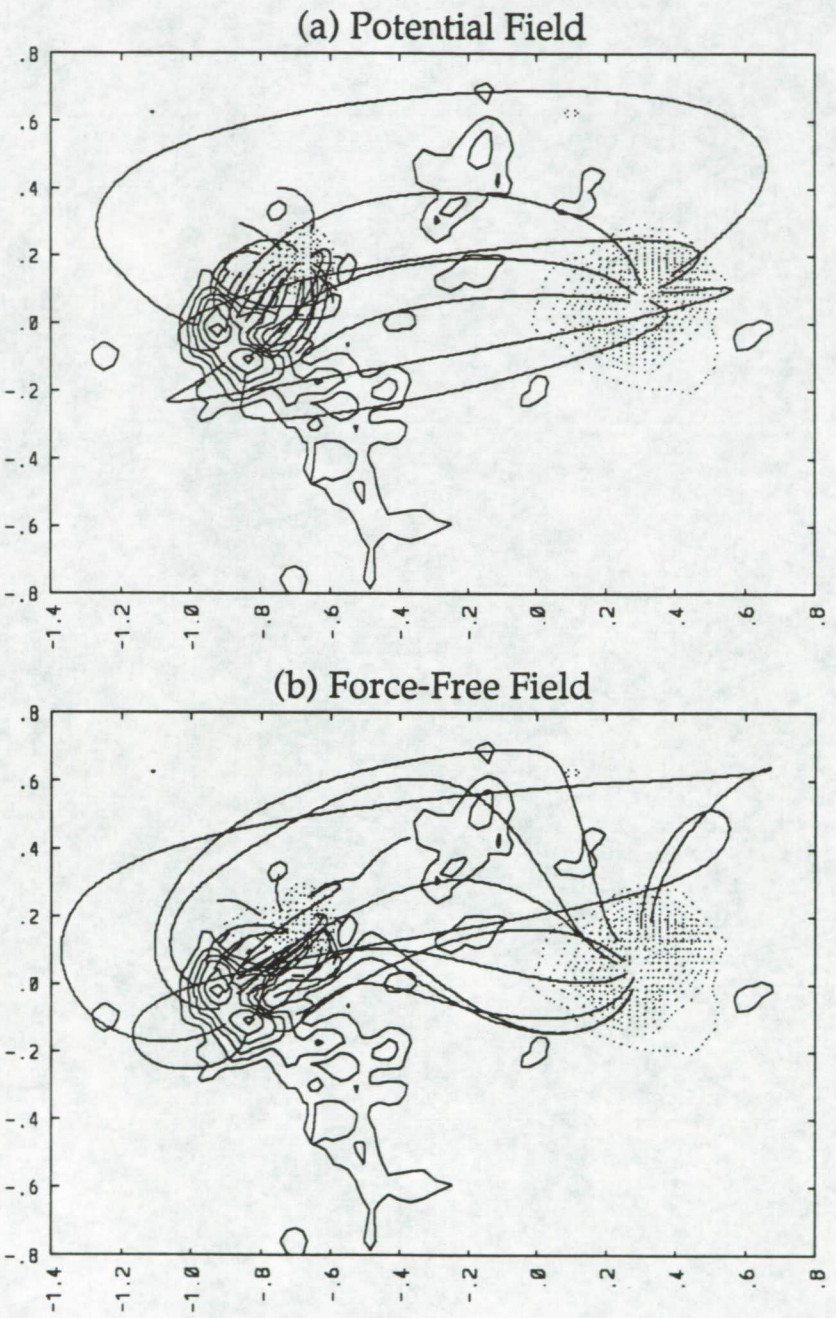

Figure 7.—Traces of the field lines in (*a*) the potential coronal field of active region 7260 on 18 August, 1992, and (*b*) the estimated force-free field as determined from a vector magnetogram of this region.

how flares and coronal mass ejections may be initiated by sudden disruptions of the magnetic field. The evolution of coronal arcades in response to applied shearing photospheric flows indicates that disruptive behavior can occur beyond a critical shear. The disruption can be traced to ideal MHD magnetic nonequilibrium. The magnetic field expands outward in a process that opens the field lines and produces a tangential discontinuity in the magnetic field. In the presence of plasma resistivity, the resulting current sheet is the site of rapid reconnection, leading to an impulsive release of magnetic energy, fast flows, and the ejection of a plasmoid. These results are related to previous studies of force-free fields and to the properties of the "open-field" configuration. The field lines in an arcade are forced open when the magnetic energy approaches (but is still below) the open-field energy, creating a partially open field in which most of the field lines extend away from the solar surface. Preliminary application of this model to helmet streamers indicates that it is relevant to the initiation of coronal mass ejections. Appendix B contains a preprint of this article (Mikić & Linker 1994).

3. STATEMENT OF WORK (3RD YEAR)

During the third year of this project we intend to continue development and application of the "evolutionary technique" for the determination of coronal magnetic fields. Next year's plan is centered around the following principal goals:

3.1 Comparison of Estimated Fields with Coronal Observations

We will continue to compare the properties of the estimated coronal magnetic fields with observations. Initially we will compare the magnetic fields already computed for AR6919 on 15 November, 1991, and AR7260 on 18 August, 1992 (as described in Sections 2.5 and 2.6) to Yohkoh soft X-ray images of these regions, and also to Yohkok hard X-ray emissions and Hα brightening during flares.

3.2 Application to Additional Vector Magnetograms

We are in the process of using the excellent data from the Advanced Stokes Polarimeter (ASP), which was built at HAO, and is presently used for solar observations at the Sacramento Peak Observatory in Sunspot, New Mexico. This instrument has very high spatial resolution, and is a "next-generation" polarimeter with the capability of measuring photospheric and chromospheric magnetic fields with high accuracy. We will be analyzing magnetograms taken in June 1992, and also those taken recently in November 1993.

3.3 Effect of Emerging Flux

We will continue a theoretical effort, which was begun this Fall, to study the effect of emerging flux. Significant emergence of magnetic flux was observed during the evolution of AR7260 in August 1992. (Recall that we have estimated the coronal field above this region on August 18, as described in Section 2.6.) The theoretical role of emerging flux is not well know. We are developing our code to include the effect of emerging flux, and we will study its effect during the next year.

3.4 Accuracy of Computed Coronal Fields

We will continue to study the accuracy and limitations of the evolutionary technique. The effect of errors will be studied by applying the technique to "synthesized magnetograms," which will be constructed by adding random errors to fields with known solutions. The solutions we will use are those described in Sections 2.3 and 2.4.

4. REFERENCES

Golub, L. 1991, in *Mechanisms of Chromospheric and Coronal Heating*, P. Ulmschneider, E. R. Priest, & R. Rosner (eds.), (Berlin: Springer-Verlag), p. 115.

Klimchuk, J. A., Lemen, J. R., Feldman, U., Tsuneta, S., & Uchida, Y. 1992, *PASJ.*, **44**, L181.

Leka, K. D., Canfield, R. C., McClymont, A. N., de La Beaujardière, J.-F., Fan, Y., & Tang, F. 1993, *Ap. J.*, **411**, 370.

Low, B. C., & Lou, Y. Q. 1990, *Ap. J.*, **352**, 343.

McClymont, A. N., & Mikić, Z. 1993, Solar Physics Divison Meeting, Palo Alto, CA, July 13–16.

McClymont, A. N., & Mikić, Z. 1994, *Ap. J.*, to appear Jan. 20. This preprint is attached as Appendix A.

Mikić, Z. 1993, Solar Physics Divison Meeting, Palo Alto, CA, July 13–16.

Mikić, Z., & Barnes, D. C. 1994, in preparation.

Mikić, Z., & McClymont, A. N. 1994, in preparation.

Mikić, Z., & Linker, J. A. 1994, *Ap. J.*, accepted for publication. This preprint is attached as Appendix B.

APPENDIX A:

PREPRINT

McClymont, A. N., & Mikić, Z., "Thickness Variations along Coronal Loops Inferred from Vector Magnetograph Data," to appear in *Astrophysical Journal*, January 20, 1994.

Thickness Variations along Coronal Loops Inferred from Vector Magnetograph Data

A. N. McClymont
Institute for Astronomy
University of Hawaii, HI 96822

and

Z. Mikic
Science Applications International Corp.
San Diego, CA 92121

Submitted to Astrophysical Journal; to appear January 20, 1994

Received _____; Accepted _____

ABSTRACT

It has been noted for many years that images of active region coronal loops seen in soft X-rays or extreme ultraviolet emission suggest a pipe-like appearance. Recently Klimchuk et al. (1992) have quantified this characteristic, finding for several loops observed by the Soft X-ray Telescope on the Yohkoh spacecraft a thickness variation along their lengths of only 10—20%. We demonstrate here that this observation is consistent with the characteristics of current-carrying field lines in a highly sheared active region. Vector magnetogram data on NOAA active region 5747, taken with the Stokes Polarimeter at Mees Solar Observatory on 1989 October 20, provided photospheric boundary conditions from which a force-free coronal magnetic field was computed. By tracing field lines, we show that magnetic loops which are highly sheared do not expand rapidly in height, as they would in a potential field. In addition, the expanding sections close to the footpoints of current-carrying twisted loops tend to be more vertical than in a potential field, so that when seen projected against the solar disk, the loops appear to terminate more abruptly. Consequently current-carrying loops exhibit a near-uniform cross-section with thickness variations of order 30% along their lengths.

Subject headings: Sun: Corona — Sun: Magnetic Fields — Sun: X-Rays, Gamma Rays

1. INTRODUCTION

Coronal soft X-ray emitting loop structures are generally believed to identify the paths of magnetic field lines. Since the Skylab era it has been noted that some coronal loops appear to be of remarkably uniform thickness, a result recently confirmed by high-resolution observations (Golub 1991, Klimchuk et al. 1992.) If the emitting volume outlines a bundle of field lines, or flux tube, the implication is that the magnetic field does not expand in height as it would if the field were potential. An alternative interpretation is that the emitting volume does not outline a flux tube, but that emission near the footpoints of the loop encompasses a thicker bundle of field lines than emission from the upper part of the loop. The temperature/density structure of a loop in energetic equilibrium (Craig, McClymont & Underwood 1978, Rosner, Tucker & Vaiana 1978) could reduce the diameter of the emitting region which is above the threshold for detection as height increases. However, it seems very unlikely that the distribution of emissivity along the loop would compensate so precisely for the change in magnetic cross-section, or that the apparent constant thickness of the loop would be preserved in observations sensitive to different temperatures. Here we assume that the emission outlines a flux tube, and show that the coronal field of a highly sheared active region, reconstructed from actual vector magnetograph data, is consistent with this interpretation.

The variation of magnetic field strength along a flux tube is of interest from several other points of view. One is the effect of area variation on the thermal conductive energy balance of the plasma in a quasi-static hot loop (e.g., Dowdy, Emslie & Moore 1987). Area variation may also have important effects on mass flows, particularly in the context of blue-shifted soft X-ray emission in the impulsive phase of flares, which can be interpreted as the signature of chromospheric evaporation (see Doschek 1990, Antonucci, Dodero & Martin 1990). Another important consequence of area variation is the magnetic mirroring of high energy particles accelerated in the impulsive phase of a flare (e.g. Petrosian 1985, LaRosa & Emslie 1988, Lu & Petrosian 1990). Theoretical investigations of these effects to date have adopted simple ad hoc models of the area variation. The results of these studies also seem to be contradictory to some extent. For instance, LaRosa & Emslie (1988) conclude that to explain the low brightness of the chromosphere relative to coronal emission in the impulsive phase of a flare, a loop

into which nonthermal electrons are injected must narrow considerably towards its footpoints. On the other hand, Petrosian (1985) suggests that the field must be nearly uniform to explain impulsive γ-ray directivity.

We present here the first theoretical study of area variation along magnetic flux tubes based on observational data. The reduction of the vector magnetograph data is described in § 2, and the interpretation of these data in terms of photospheric boundary conditions on the coronal magnetic field is discussed in § 3. The method for constructing a force-free representation of the coronal field is described in § 4, and the analysis of loop thickness variations is presented in § 5. Our results are described in § 6, and our conclusions summarized in § 7.

2. OBSERVATIONS

The data used in this analysis were obtained with the Stokes Polarimeter at Mees Solar Observatory on Haleakala (Mickey 1985). NOAA active region 5747, which produced a series of major flares, was observed 1989 October 18—22. Here we use the data obtained on October 20 (scanned from 17:41 to 18:33 UT), which are of superior quality compared to the other days.

A full account of the observations and data reduction techniques has been given by Canfield et al. (1993) and Leka et al. (1993). Briefly, the Stokes Polarimeter obtained full Stokes profiles in the magnetically sensitive Fe I lines at 6301.5 and 6302.5 Å, building up a raster by scanning point-by-point over the active region, in steps of 5.6", with a field of view at each pixel of 6". The data were reduced using the least-squares fitting code of Skumanich & Lites (1987). Raster points at which the polarization was too low for a least-squares fit were reduced using the integral method (Ronan, Mickey & Orrall 1987). The ambiguity in direction of the transverse magnetic field in the resulting vector magnetogram was resolved as described by Canfield et al. (1993), and the magnetogram transformed to disk center. The vertical magnetic field and current density, computed from the curl of the horizontal field, define the photospheric boundary conditions needed to reconstruct the coronal force-free field.

We have also used observations of a near-potential active region for comparison with the highly nonpotential AR 5747. These observations, of AR 7490, magnetic classification α, were scanned with the Haleakala Stokes Polarimeter on 1993 April 28 from 17:31 to 19:03 UT, and reduced using the same procedure outlined above.

3. INTERPRETATION OF OBSERVATIONS

Since the photosphere is probably not force-free at the observed level (i.e. the depth of formation of the spectrum lines used in the analysis), is it then possible to use this data to compute a force-free field? The effect of mechanical forces can be considered in the limit of two spatial scales: (1) individual flux tubes which are much smaller than both the spatial resolution of the instrument and the global size scales of the active region, and (2) the large scale field of sunspots.

Outside sunspots, the magnetic field at the photosphere does not vary smoothly, but occurs in flux tubes of high field strength (≈1500 G) but very small size scale (≈150 km), separated by field-free photosphere (Stenflo 1989). Therefore the field lines fan out rapidly as they leave the pressure-confining photosphere. Since the field spreads out to become force-free only a few hundred km above the photosphere, the discrete nature of the field at the lower level should not affect the global structure of the corona. The "spread-out" field is the appropriate one to use as a boundary condition in computing the coronal field. The question is

whether we can approximate this field using the data available. Since the spatial resolution of the polarimeter, 4–5 Mm, is much coarser than the fine scale photospheric structure and is of order the smaller size scales important to the global structure of the active region, the polarimeter does indeed yield a suitably smoothed field, provided it correctly measures the average field strength. The circular polarization signal is proportional to the longitudinal field strength, and so measures the average field directly. The linear polarization signal, however, is proportional to the square of the transverse field, and thus overestimates the average transverse field when the filling factor is low (Stenflo 1985). In strong field regions (sunspot umbrae), this is not a problem, since the filling factor is very close to unity. Over most of the area of significant flux in the active region (penumbrae, plage), we can use the information in the line profiles to determine the filling factor (Skumanich & Lites 1987), so that the average transverse field over a pixel can be derived, at least to first order. In weak field regions (where there is little visual indication of the presence of magnetic field), the polarization signal is too small for a least-squares fit, and we use the integral method (Ronan, Mickey & Orrall 1987), which does not yield a correction for the filling factor. Since the filling factor is generally small in these areas, the transverse field may be overestimated. However, the contribution to the active region flux from these weak field regions is of order 1% in the present dataset, so these errors will not have an appreciable effect on the accuracy of the force-free solution.

Turning to the large scale mechanical forces present in the photosphere, i.e. the gas pressure confining sunspots, the distribution of the photospheric magnetic field must satisfy a number of constraints to be compatible with an overlying force-free field (e.g. Low 1985, Aly 1989). First, in order for the region to be considered isolated, the magnetic flux and vertical current must balance within the field of view. In the present case, both balance to within a few percent. Second, the total force and torque exerted on the photosphere by the overlying magnetic field must vanish. For this dataset, the horizontal forces and the vertical torque are of order a few percent (normalized by the mean magnetic pressure integrated over the photosphere, and in the case of torque multiplied by the size of the active region), but the vertical force and horizontal torque are of order 10%. These particular discrepancies are not unexpected however, since the photosphere is manifestly not force-free, in the sense that the magnetic field in sunspots would be expelled from the photosphere by the buoyancy force if it was not attached to a subphotospheric flux tube. The total vertical force on the photosphere is given by $F_n = \int (B_n^2 - B_t^2)\, dA/8\pi$, where B_n and B_t are the magnetic field components normal to and parallel to the photosphere. In a sunspot, the field lines are pushed together into a more vertical orientation than if they were force-free, yielding a positive F_n. However, the currents associated with this force circulate horizontally around the flux tubes, extending at most a few pressure scale heights (a few hundred km) above the observed level. They do not enter the corona, and therefore do not influence in a direct way the global structure of the coronal magnetic field. These currents cannot be detected in a vector magnetogram made at one level in the atmosphere, which can measure only the vertical component (J_n) of the current. The non-force-free nature of sunspots is not expected to change the structure of the coronal field in any substantial way (Aly 1989).

Another constraint which the photospheric field must satisfy if the coronal field is to be force-free concerns the distribution of $\alpha = J_n/B_n$. Since α is conserved along each field line, there must be the same number of footpoints of field lines with a given value of α in each magnetic polarity. A study of this same magnetogram (Canfield et al. 1991) revealed discrepancies in the distributions of flux over α which seemed to be significantly above the noise. One of our long-term aims is to investigate the response of the numerical model to such discrepancies in the data.

4. COMPUTATION OF THE CORONAL MAGNETIC FIELD

To compute the coronal magnetic field, a 3D resistive MHD code (Mikic, Barnes & Schnack 1988, Mikic & Barnes 1993) is used to evolve the field until it satisfies the desired boundary conditions at the photosphere. The magnetogram, which does not map onto a rectangular region of the solar surface, is first interpolated onto a Cartesian grid. This is embedded in a larger field-free region to isolate the active region from the effect of the computational boundaries. The grid is nonuniform in the horizontal dimensions, to remove the boundaries as far as possible while maintaining resolution in the region of interest. The grid is also nonuniform in the vertical direction, to resolve rapid variations in the field close to the photosphere. The 3D grid (60×60×40 mesh points) forms a cuboid 366 Mm on a side, roughly four times the extent of the strong-field region of the spot group, and 244 Mm high. The potential field defined by the normal component of the photospheric field, B_n, is computed first, then voltages are applied at the photosphere to drive currents through the corona. The voltages are ramped up over time and adjusted adaptively to drive the currents towards the desired normal current density, J_n. Resistivity allows the evolving field lines to change their topology as required to reach a force-free state. Once the field is close to its final configuration, the resistivity can be reduced, and if the boundary data are perfectly consistent, a force-free field will ensue.

In practice, data imperfections, the effect of discretization, and possibly mechanical forces in the photosphere, prevent a completely force-free state from being attained. We have found that a small remnant J×B force is present near the photosphere, although it decreases rapidly with height. The corresponding steady state solution has finite flows, with steady electric fields at the boundary to balance the resistive dissipation; the J×B force is balanced by (artificially large) viscous forces. In order to obtain a completely force-free field we have also tried a different prescription. Starting from the abovementioned steady state solution, we reduce the resistivity to zero while fixing the positions of the magnetic field footpoints, without applying boundary potentials, and allow the field to relax. We find that the field then relaxes to a force-free state in which the normal electric current density at the photosphere does not match exactly that deduced from the vector magnetogram. For the data reported here, the normal electric current density is within 20–30% of the magnetogram current density. The two magnetic fields produced by this technique can be considered as two (equally good) approximations to the true field. At heights greater than ≈5 Mm above the photosphere, the two coronal fields do not differ significantly. The latter field is used in the analysis described in this paper.

5. ANALYSIS OF LOOP THICKNESS VARIATIONS

To extract the information used in this study from the computed coronal field, we trace field lines by integrating the equation $d\mathbf{r}/ds = \mathbf{B}/|B|$, where $\mathbf{r}$ is the position vector and s is arclength along the field line, from selected photospheric footpoints. An adaptive-step second order Runge-Kutta algorithm, with trilinear interpolation to obtain the magnetic field between mesh points, proves to be of adequate accuracy (r.m.s. error in footpoint position of approximately 0.03 mesh points when tested on a dipole field).

For the purposes of this study, we adopt the simple "microscopic" definition of flux tube cross-sectional area, $A = \Phi/B$, where Φ is the (infinitesimal) magnetic flux in an elementary flux tube. The variation in diameter (width) along an elementary flux tube, assuming, to a first approximation, a circular cross-section, is then given by $w \propto B^{-1/2}$. The variation of w along a field line (of interest for particle mirroring studies) can be studied by plotting w against s. The apparent thickness of soft X-ray emitting loops, seen in projection against the solar disk, can be studied by plotting w as a function of distance along the loop projected onto the

photosphere. We have not evaluated quantitatively the actual width of a "macroscopic" flux tube. A more detailed investigation would have to account for the changing shape of the bundle of field lines along the length of the loop. We do, however, compare qualitatively macroscopic flux tubes in the highly nonpotential AR 5747 with similar macroscopic flux tubes in the near-potential region AR 7490.

In the complicated three-dimensional structure of the active region magnetic field, many of the variables are correlated (e.g. the magnetic field falls with increasing height, strong currents only occur in regions of strong field, etc.), and it is difficult to demonstrate directly that field-aligned currents are responsible for changes in the shape of flux tubes. Here we adopt three approaches:

First, we compare the thickness variation along field lines traced in the computed force-free field with field lines traced in the potential field computed from the same boundary data, but ignoring currents entering the corona. We choose footpoints in the areas of strong photospheric current density. Here we deal with the morphology of only one active region, but a drawback of this approach is that the potential field can be criticized as unphysical: for instance, force-free field lines starting from footpoints in a sunspot may end in a sunspot of opposite polarity, while potential field lines starting from the same footpoints may end in a weak field region.

Second, we have studied the correlation between current density at the footpoints of the field lines and the "expansion factor" (following the definition of Klimchuk et al. 1992, but applied to "microscopic" flux tubes). Klimchuk et al. "straighten" observed loops, seen projected against the photosphere, and define the expansion factor as the ratio of apparent loop thickness at the midpoint between the footpoints to the apparent thickness at the narrower footpoint. They define the "footpoints" to be the locations at which the soft X-ray intensity drops to half of the maximum intensity along the loop. Since we do not have a measure of the X-ray brightness of our model loops, we take the "footpoints" to be 15% of the loop length (projected) in from the true photospheric footpoints. This corresponds to the average distance between the half-intensity points and the apparent ends of the observed loops (Klimchuk, private communication). Because of the correlation of strong current with strong field, and stronger fields with lower heights, careful interpretation of these scatter plots is necessary.

Third, to achieve a comparison with physically realistic potential field lines, and also to examine the characteristics of "macroscopic" flux tubes, we compare the shapes of flux tubes in the force-free field of AR 5747 (again rooted in strong current regions) with those in a different active region which is close to potential (AR 7490, observed with the Haleakala Stokes Polarimeter 1993 April 28). Although the potential field lines are physically realistic in this case, the active region has a very different character from AR 5747.

6. RESULTS

Figure 1 shows the magnetogram of AR 5747 with field lines projected against the photosphere. Contours show the vertical component of the photospheric magnetic field. In the left panel, the field lines were computed using the reconstructed force-free field, while the field lines in the right panel were computed from the potential field obtained by ignoring the currents entering the corona. The same footpoint positions, chosen to lie in the areas of strong vertical current (in both magnetic polarities), were used in tracing both sets of field lines. It will be noted that in the potential field calculation, field lines originating in the left part of the positive spot cross the neutral line in a perpendicular direction, while in the force-free calculation, the same field lines are strongly sheared, running a long distance parallel to the neutral

line, to end in the upper of the two negative spots.

Figure 2 shows the width (diameter) of elementary flux tubes (assuming that the cross-section remains circular) as a function of distance along the loop, projected onto the photosphere. The widths are normalized to unity at the footpoint with the stronger field. This simulates the measured width of soft X-ray loops seen in projection against the solar disk. On the left are field lines from the computed force-free field; on the right, for comparison, are field lines from the potential field. computed by ignoring the currents entering the corona from the photosphere. The difference is striking. Most of the force-free flux tubes are of remarkably uniform diameter over most of their lengths, narrowing only close to their photospheric footpoints (cf. Golub 1991). The potential field lines, in contrast, show no such attribute. The variation in thickness of the force-free flux tubes may be estimated by eye as being of order 10—20% over most of their length, as observed by Klimchuk et al. (1992). A comparison of the computed shapes with the observed shape shown in Figure 2 of Klimchuk et al. (1992) seems compelling.

To gain insight into the difference between the force-free and potential fields, it is useful to consider the variation in area along each field line as a function of arclength from each footpoint. Figure 3 shows such a plot, in which each curve represents the portion of a field line from its footpoint to its widest point. In both the force-free and potential fields, the initial rate of increase in diameter with distance from the footpoint is about the same up to a distance of $\approx$10 Mm, which corresponds roughly to the radius of the large spots. Therefore, close to the footpoints the decrease in field strength is controlled largely by the fanning out of field lines as they leave the sunspots, independent of the character of the active region on the global scale. At greater heights, there is a significant difference, with the diameter of current-carrying flux tubes increasing much less rapidly than in the potential field case.

We have attempted to quantify the effect of field-aligned current on the shape of flux tubes by using the "expansion factor" as defined by Klimchuk et al. (1992). As mentioned in § 5, it is difficult to unambiguously relate the shape of the flux tube to current density, since, for example, the strongest currents occur only in the strongest magnetic fields; because the sunspot group is relatively compact in this case, these field lines are low-lying. Therefore scatter plots of expansion factors of selected field lines against current density at the photosphere (Fig. 4a), and of expansion factor against maximum height attained by the field line (Fig. 4b), both show a correlation. The plot of expansion factor against field strength at the photosphere (Fig. 4c) shows less correlation. In these plots, we have averaged the current densities and field strengths between the two footpoints, and normalized them to the peak values of approximately 27.2 mA m^{-2} and 2840 G present in the magnetogram. The maximum heights were normalized to 50 Mm, the distance between the centers of the two largest sunspots. The set of field lines used here is larger than the set shown in Figure 1, and includes field lines from regions of low photospheric current density. We excluded from the set a few field lines with apices higher than the maximum height shown in Figure 4b; some of these have much larger expansion factors than shown here, and the highest tend to be distorted by the upper computational boundary,

Can we conclude that current-carrying field lines are of more constant cross-section than non-current-carrying field lines, or should we conclude that lower-lying field lines are of more constant cross-section? It is clear from Figure 4a that on average the expansion factor decreases with increasing current density. For field lines carrying significant currents ($\geq$ 1/4 of the maximum current density), the expansion factor is below 1.5, regardless of the height the field line reaches. The average expansion factor in the high-current range is approximately 1.3, somewhat larger than the value of 1.13±0.10 found by Klimchuk et al., but nevertheless

suggesting a significant result. However, some loops carrying only small currents also exhibit small expansion factors (lower left area of Fig. 4a.)

In Figure 4b we see that the smallest expansion factors of all occur for very lowlying loops ($H \leq 0.1$, or 5 Mm.) These are short loops (average length around 15 Mm) bridging the neutral line. Because of their small size compared to the global scale of the active region, the magnetic field strength does not vary much along these loops. Their small expansion factors are due to their situation in a two dimensional arcade field, while higher field lines expand in three dimensions. Although these field lines are strongly sheared in this case, they would have relatively constant cross-sections even in a potential field. If the potential field of an active region could be represented by a single buried horizontal dipole, at depth D, (not a good approximation in general) the field strength at the loop tops (for field lines lying in the vertical plane above the dipole) would fall off with height H, as $(D+H)^{-3}$, implying an increase in flux tube diameter at the apex with height of $(D+H)^{3/2}$. Measured along an individual field line, the flux tube diameter would increase linearly with height, h, except close to the apex ($h=H$):

$$w \propto (D+h)\ \{1-\tfrac{3}{4}[(D+h)/(D+H)]^{2/3}\}^{-1/4}. \tag{1}$$

This yields the expansion factor

$$\begin{aligned} f &\approx 1+(5/3)H/D \quad H \ll D \\ f &\approx \sqrt{2}(1+H/D) \quad H \geq D \end{aligned} \tag{2}$$

Estimating a dipole depth of 50 Mm, the distance between the biggest spots, then leads us to conclude that field lines (in the vertical plane) with apex heights below 10 Mm (0.2 normalized units) will have expansion factors of less than 1.33 solely because their lengths are short compared to the scale size of the global field. This is consistent with the behavior seen in Figure 4b. For higher-lying field lines (those with $0.2<H<0.7$, corresponding to maximum heights of 10 Mm to 35 Mm) we attribute small expansion factors to the presence of field-aligned currents. For $H>0.7$ (35 Mm) the lower limit on the expansion factor seems to drift upwards, becoming greater than 1.5 for field lines reaching heights of 50 Mm. The largest expansion factors shown in Figure 4b are consistent with the result of equation (2) for $H \approx D$.

To clarify the relationship implied by these correlations, we have constructed a scatter plot of the expansion factors, f, against the linear combination of the variables, $u=aJ+bB+cH$, where a, b, and c are constants to be adjusted to minimize the scatter of points in a least squares sense. The function fitted to the data was chosen to be a curve defined parametrically by cubic polynomials $u(t)$ and $f(t)$. The best correlation between u and f, shown in Figure 4d, was found for the combination of variables, $u=J-0.18H-0.09B$. Figure 4d also shows the fitted curve. This confirms the results suggested in Figure 4a–c: the magnetic field strength at the footpoint does not greatly influence the expansion factor; the height reached by the field line has a greater effect; but the primary determinant of expansion factor is the current density.

So far we have considered elementary flux tubes, assumed to be of circular cross-section. Lastly, we compare "macroscopic" flux tubes which carry substantial currents in the highly nonpotential active region AR 5747, with similar flux tubes traced in a near-potential active region, AR 7490. The differing appearances of the "loops" shown in Figure 5 supports our assertion that field-aligned currents are responsible for the near-invariant cross-sections of soft X-ray loops. The loops shown in the nonpotential active region probably have expansion factors of no more than 2, while the expansion factors of the loops in the potential active region

are clearly greater than 2.

7. CONCLUSIONS

The intriguing observation that many soft X-ray emitting loops, whose emissions probably outline bundles of magnetic field lines, appear to be of near-constant cross-section, can be explained if the loops lie on strongly sheared, current-carrying field lines. Not only does the magnetic field strength fall less rapidly with height when current is present in the corona, but the twist in the field lines tends to make the force-free field lines enter the photosphere at a steeper angle, foreshortening the tapered section of the flux tubes seen in projection against the solar disk. For the dataset examined here, the variations in loop thickness are of order 30%. While larger than the 13% variation observed by Klimchuk et al. (1992), the variations are significantly less than those of a potential field. We find also that field lines in the nonpotential active region which do not carry significant currents exhibit area variations more like the potential field than like the current-carrying field lines illustrated here. Thus the observation that bright soft X-ray loops tend to be of uniform width suggests, as mentioned by Klimchuk et al., that coronal heating is associated with strong field-aligned currents. Lowlying loops which are short compared to the global length scales of the active region form an exception to this statement, since they can have near-constant field strength along their lengths. A goal for the future will be to model the coronal magnetic field in an active region for which cotemporal soft X-ray observations are available. We anticipate that the techniques of modeling 3D force-free coronal fields employed here will answer many other questions regarding active region magnetic topology and energetics.

This research was supported by NSF grant ATM-9108369 to SAIC and by NSF grant ATM-9106052 to the University of Hawaii. We thank Jim Klimchuk for helpful information and comments, and Bob Rosner for constructive criticisms which have greatly improved the analysis.

REFERENCES

Aly, J. J. 1989, Solar Phys., 120, 19

Antonucci, E., Dodero, M. A., & Martin, R. 1990, Ap. J. Supp., 73, 147

Canfield, R. C., Fan, Y., Leka, K. D., McClymont, A. N., Wülser, J.-P., Lites, B. W., and Zirin, H. 1991, in *Solar Polarimetry*, ed. L. November, (Sunspot: NSO/SP), p. 296

Canfield, R. C., de la Beaujardiere, J.-F., Fan, Y., Leka, K. D., McClymont, A. N., Metcalf, T. R., Mickey, D. L., and Wülser, J.-P. 1993, Ap. J. (1 July 1993)

Craig, I. J. D., McClymont, A. N., & Underwood, J. H. 1978, Astron. Astrophys., 70, 1

Doschek, G. A. 1990, Ap. J. Supp., 73, 117

Dowdy, J. F., Emslie, A. G., & Moore, R. L. 1987, Solar Phys., 112, 255

Fisher, G. H., Canfield, R. C., and McClymont, A. N. 1985, Ap. J., 289, 425

Golub, L. 1991, in *Mechanisms of Chromospheric and Coronal Heating*, P. Ulmschneider, E. R. Priest & R. Rosner (eds.), (Berlin: Springer-Verlag), p. 115

Klimchuk, J. A., Lemen, J. R., Feldman, U., Tsuneta, S., & Uchida, Y. 1992, PASJ, 44, L181

LaRosa, T. N., & Emslie, A. G. 1988, Ap. J., 326, 997

Leka, K. D., Canfield, R. C., McClymont, A. N., Fan, Y., and Tang, F. 1993, Ap. J. (1 July 1993)

Low, B. C. 1985, in *Measurements of Solar Vector Magnetic Fields*, ed. M. J. Hagyard, (NASA Conf. Pub. 2374), p. 49

Lu, E. T., & Petrosian, V. 1990, Ap. J., 354, 735
Mickey, D. L. 1985, Solar Phys., 97, 223
Mikic, Z., Barnes, D. C., & Schnack, D. D. 1988, Ap. J., 328, 830
Mikic, Z., & Barnes, D. C. 1993, in preparation
Petrosian, V. 1985, Ap. J., 299, 987
Ronan, R. S., Mickey, D. L., & Orrall, F. Q. 1987, Solar Phys., 113, 353
Rosner, R., Tucker, W. H., & Vaiana, G. S. 1978, Ap. J., 220, 643
Skumanich, A. & Lites, B. W. 1987, Ap. J., 233, 473
Stenflo, J. O. 1985, in *Measurements of Solar Vector Magnetic Fields*, ed. M. J. Hagyard, (NASA Conf. Pub. 2374), p. 263
Stenflo, J. O. 1989, Astron. Astrophys. Rev., 1, 3

FIGURE CAPTIONS

Fig. 1 — Magnetogram of NOAA active region 5747 on 20 October 1989, after resolution of the ambiguity in the azimuth angle of the transverse field and rotation to disk center. Solar North is approximately 20° anticlockwise from the top. Contours (at approximately 160×2^n Gauss, n=0,1,2,3,4) show the vertical component of the magnetic field, with solid lines marking positive polarity and broken lines negative polarity. In the left panel field lines with footpoints in areas of high photospheric current density are shown projected against the photosphere. In the right panel field lines with the same starting footpoints, traced in the potential field obtained by ignoring the currents entering the corona, are shown for comparison.

Fig. 2 — Diameters of elementary flux tubes along each of the field lines shown in Figure 1, as a function of distance along the field lines, projected onto the photosphere. The left panel, showing the field lines computed from the reconstructed force-free field, illustrates the widths of coronal loops seen in projection against the solar disk (if the active region was at disk center). The right panel shows the diameters of flux tubes on the potential field lines with the same set of starting footpoints. While the potential field exhibits the expected variation, the force-free flux tubes are of remarkably constant thickness over most of their lengths (cf. Fig. 2 of Klimchuk et al. 1992).

Fig. 3 — Diameters of flux tubes as a function of arclength, measured along the field lines from each footpoint, for the force-free field (left panel) and the potential field (right panel). The potential field flux tubes clearly expand much more rapidly than the force-free flux tubes.

Fig. 4 — Expansion factor (the ratio of flux tube width at the apex of the loop divided by the width near the narrower footpoint), for a set of field lines traced in the nonpotential force-free field, with a range of magnetic field strengths and current densities at their footpoints, and a range of apex heights. Current densities and field strengths represent averages over the two footpoints, and are normalized to peak values of 27.2 mA m^{-2} and 2840 G. The apex heights are normalized to 50 Mm, the distance between the main spots. The expansion factor decreases with increasing footpoint current density [panel (a)], and increases with increasing apex height [panel (b)], but there is little correlation between expansion factor and field strength [panel (c)]. The combination of these parameters shown on the abscissa of panel (d) gives, in a simple linear model, the tightest correlation. The line represents the least-squares fit of a cubic parametric curve, $\{u(t),f(t)\}$. For current densities $\geq$ 1/4 of the maximum footpoint current density in the active region, the loops expand only about 30%. While this is larger than the expansion factor of 13±10% found by Klimchuk et al (1992), it is considerably less than expected if the field were potential. Small expansion factors are also seen for lowlying field lines in panel (b), even where the current density is small [the points to the lower left in panel (a)].

Fig. 5 — "Macroscopic" magnetic loops, formed by tracing bundles of field lines in (a) the strongly nonpotential active region AR 5747, and (b) the near-potential active region AR 7490, superposed on the photospheric magnetograms showing contours of the vertical magnetic field strength. The nonpotential loops appear to have a more uniform thickness than the potential loops.

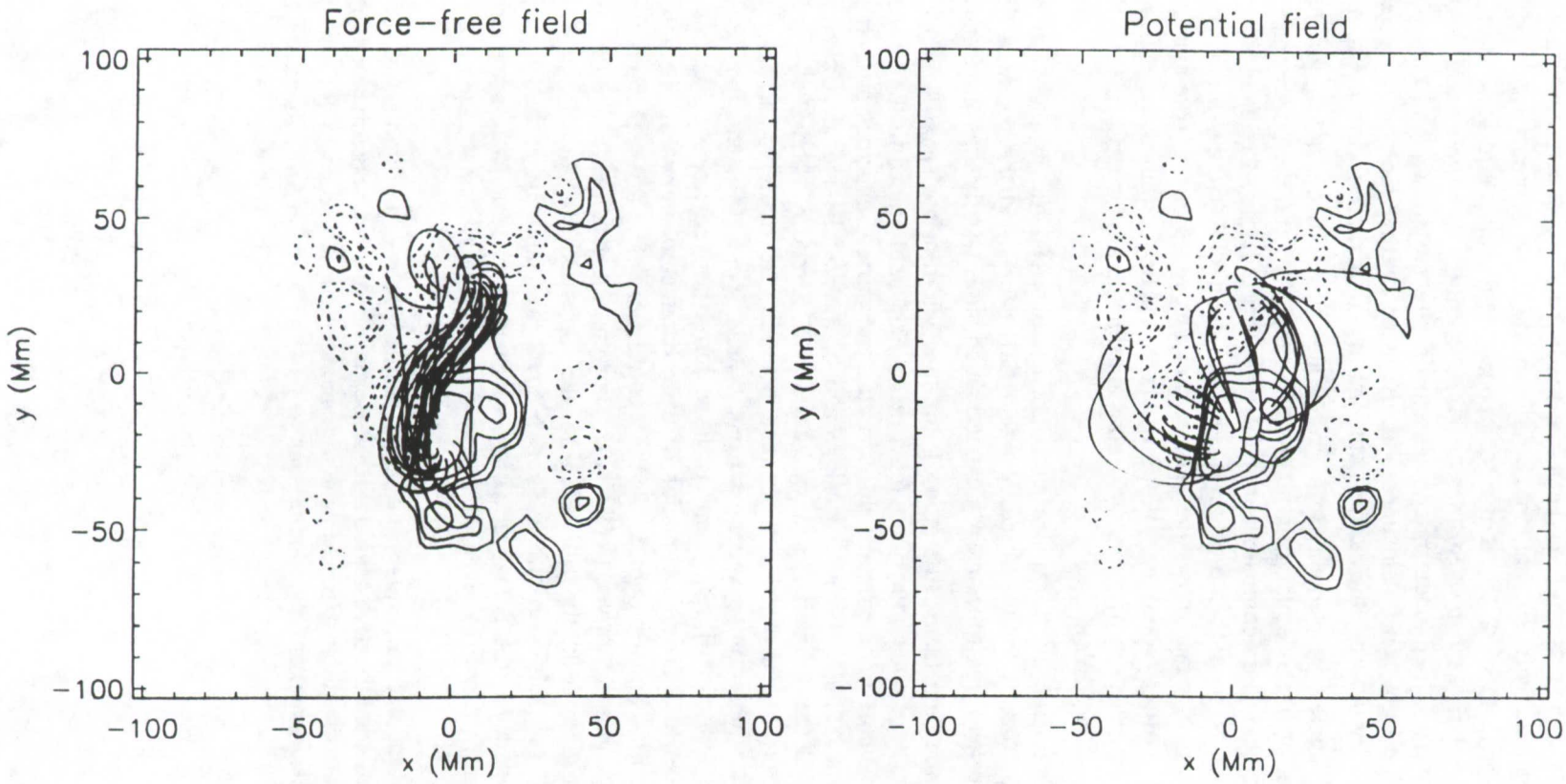

Fig 1

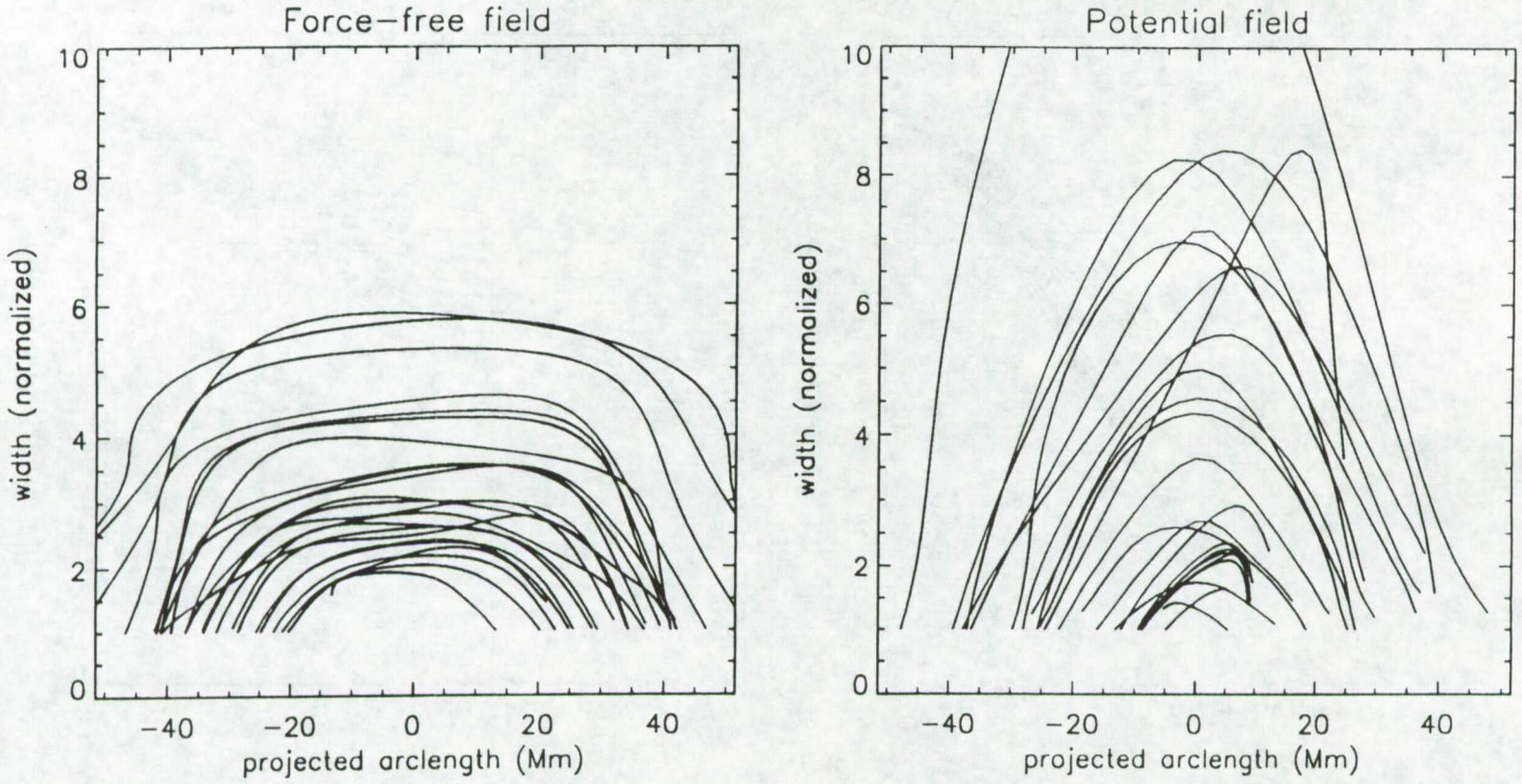
Force–free field
Potential field
width (normalized)
projected arclength (Mm)
0
2
4
6
8
10
−40
−20
0
20
40

Fig 2

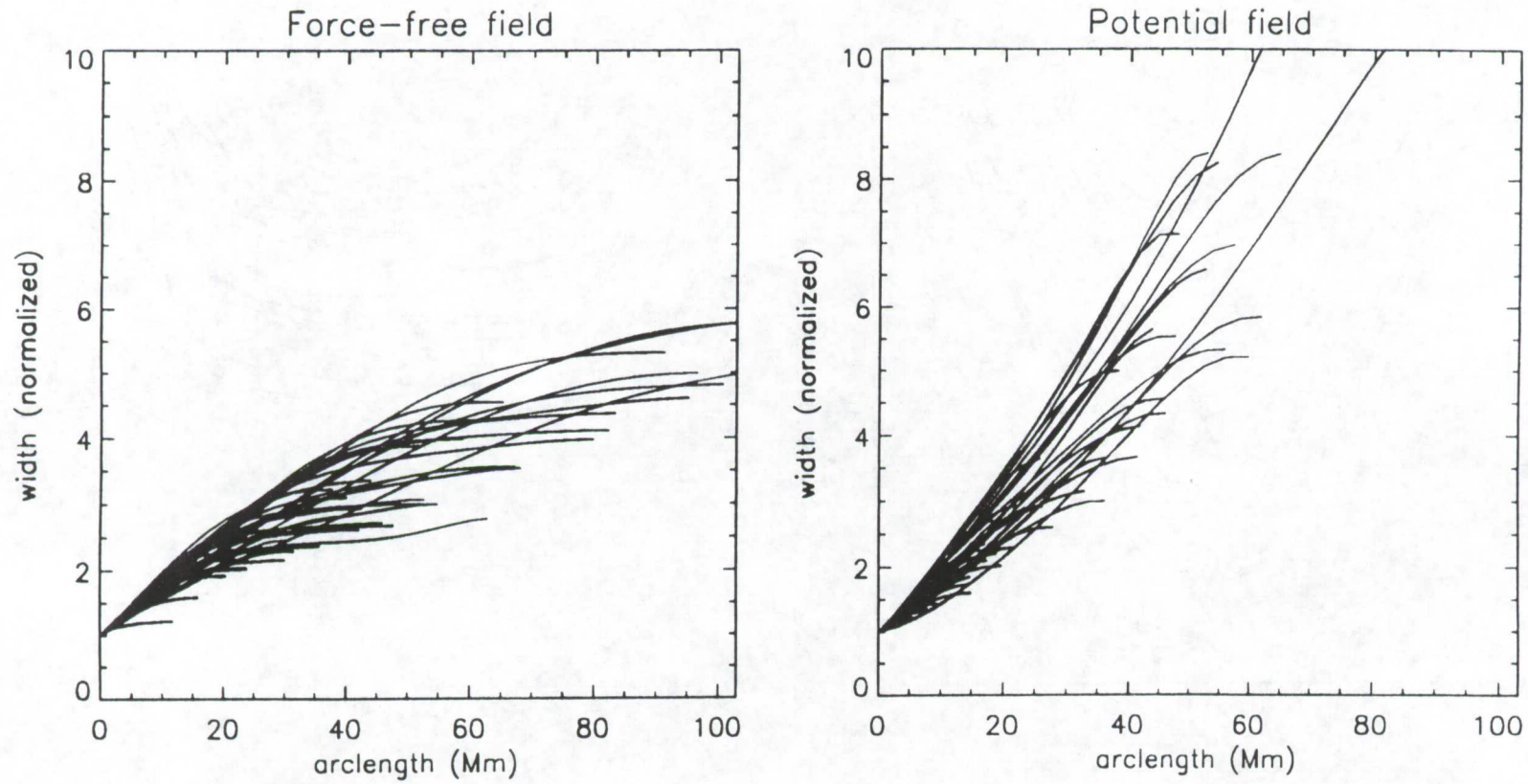
Force−free field
Potential field
width (normalized)
arclength (Mm)
0
2
4
6
8
10
0
20
40
60
80
100

Fig 2

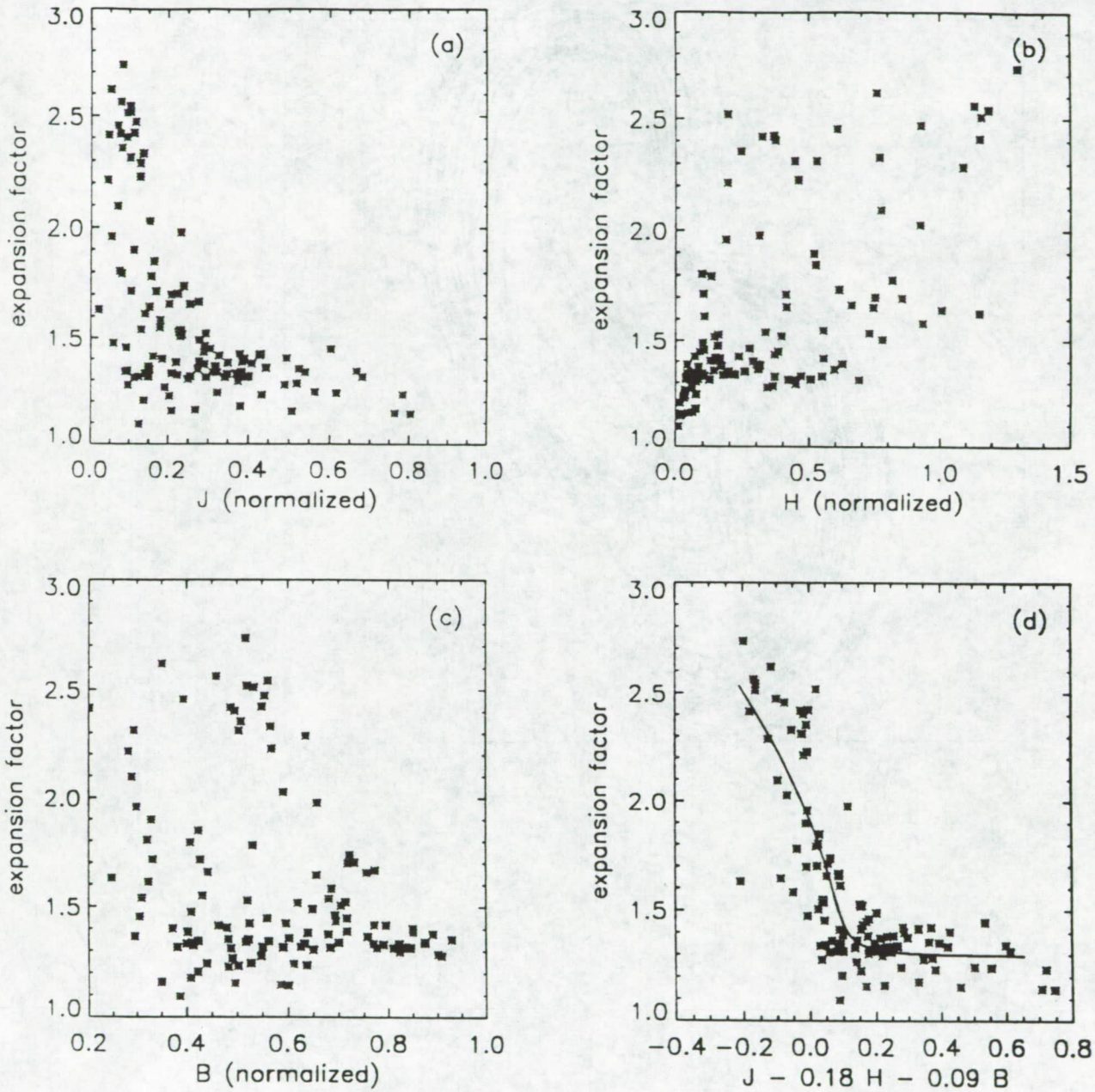
(a)
expansion factor
J (normalized)
(b)
H (normalized)
(c)
B (normalized)
(d)
J − 0.18 H − 0.09 B

Fig 4.

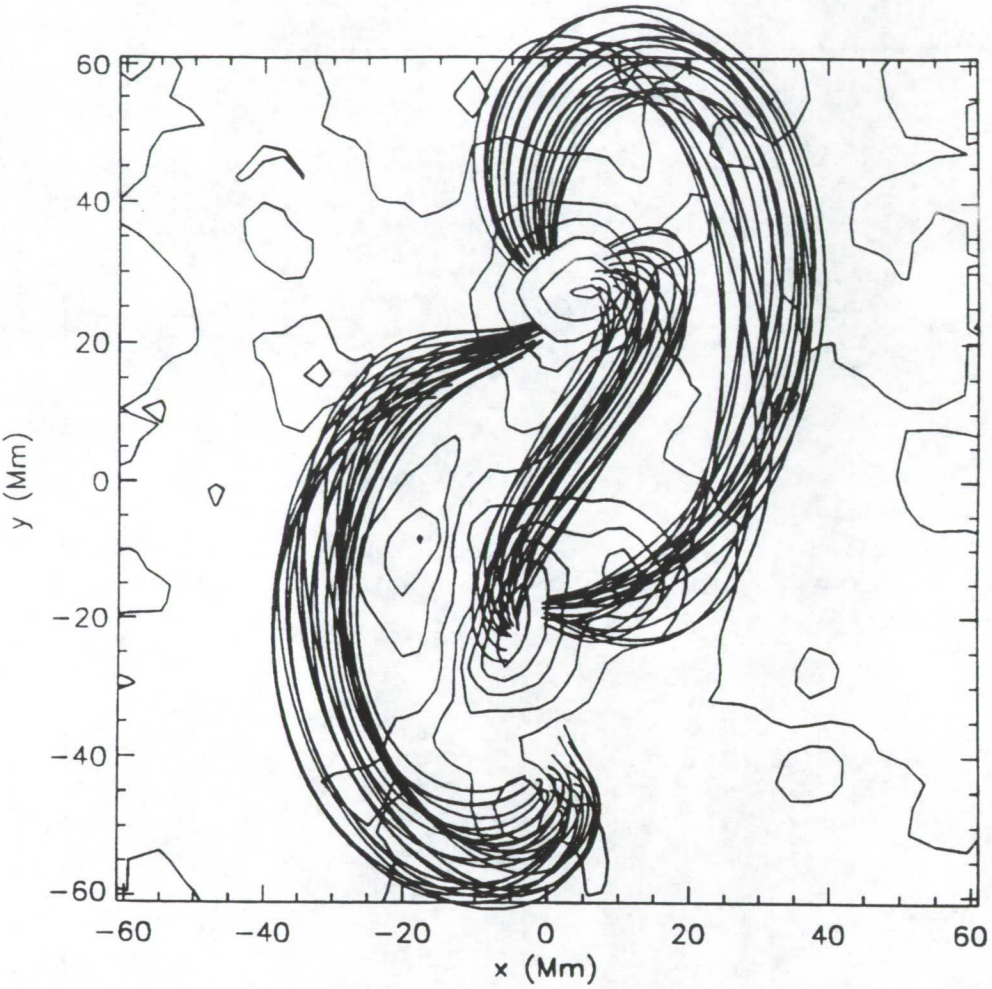

Fig 5a

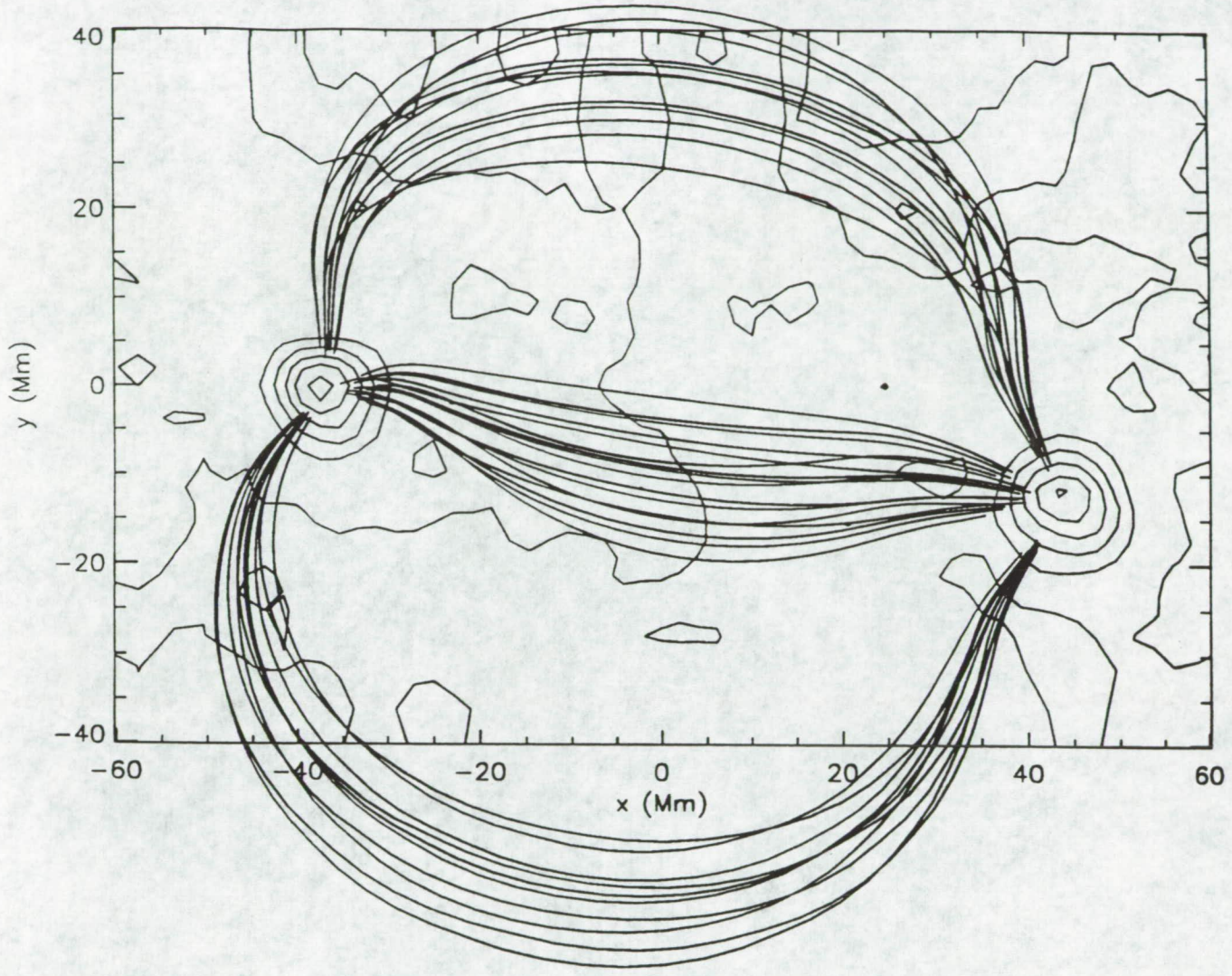

Fig5b

APPENDIX B:

PREPRINT

Mikić, Z., & Linker, J. A., "Disruption of Coronal Magnetic Field Arcades" accepted for publication in *Astrophysical Journal*, 1994.

DISRUPTION OF CORONAL MAGNETIC FIELD ARCADES

Zoran Mikić

Science Applications International Corporation

10260 Campus Point Drive

San Diego, California 92121

and

Jon A. Linker

Department of Electrical and Computer Engineering

University of California at San Diego

La Jolla, California 92093-0407

Received_____; accepted_____

ABSTRACT

The ideal and resistive properties of isolated large-scale coronal magnetic arcades are studied using axisymmetric solutions of the time-dependent magnetohydrodynamic (MHD) equations in spherical geometry. We examine how flares and coronal mass ejections may be initiated by sudden disruptions of the magnetic field. The evolution of coronal arcades in response to applied shearing photospheric flows indicates that disruptive behavior can occur beyond a critical shear. The disruption can be traced to ideal MHD magnetic nonequilibrium. The magnetic field expands outward in a process that opens the field lines and produces a tangential discontinuity in the magnetic field. In the presence of plasma resistivity, the resulting current sheet is the site of rapid reconnection, leading to an impulsive release of magnetic energy, fast flows, and the ejection of a plasmoid. We relate these results to previous studies of force-free fields and to the properties of the "open-field" configuration. We show that the field lines in an arcade are forced open when the magnetic energy approaches (but is still below) the open-field energy, creating a partially open field in which most of the field lines extend away from the solar surface. Preliminary application of this model to helmet streamers indicates that it is relevant to the initiation of coronal mass ejections.

Subject headings: MHD — Sun: magnetic fields — Sun: corona — Sun: flares

Suggested running head: DISRUPTION CORONAL ARCADES

1. INTRODUCTION

Coronal mass ejections and solar flares are spectacular manifestations of solar activity. It is believed that they are initiated by the sudden release of energy stored in the coronal magnetic field. The magnetic energy in the corona can be built up through shear introduced by photospheric motions. In principle, the free magnetic energy (that in excess of the energy in the potential field) is available for release. Although there is ample observational evidence for the existence of highly non-potential coronal magnetic fields in active regions (*e.g.*, Gary *et al.* 1987; Hagyard 1988; Canfield *et al.* 1993; Leka *et al.* 1993), which consequently have considerable free magnetic energy, it has been difficult to demonstrate theoretically that this energy can be released impulsively. In addition, since coronal mass ejections drive solar material out of the corona, at least some of the magnetic field lines must also be opened.

Many investigations have attempted to explain how energy can be released from the coronal magnetic field (Low 1981; Birn & Schindler 1981; Zwingmann 1987; Priest 1988; Priest & Forbes 1990; Forbes & Isenberg 1991; Forbes 1992; Isenberg, Forbes, & Démoulin 1993), including studies of force-free equilibria (Barnes & Sturrock 1972; Yang, Sturrock, & Antiochos 1986; Klimchuk, Sturrock, & Yang 1988; Klimchuk & Sturrock 1989; Finn & Chen 1990; Porter, Klimchuk, & Sturrock 1992; Klimchuk & Sturrock 1992; Roumeliotis, Sturrock, & Antiochos 1993), the dynamical evolution of arcades (Mikić, Barnes, & Schnack 1988; Biskamp & Welter 1989; Forbes 1990; Steinolfson 1991; Wu *et al.* 1991; Finn, Guzdar, & Chen 1992; Inhester, Birn, &

Hesse 1992; De Vore & Antiochos 1993), the equilibrium properties of open and partially open fields (Wolfson & Low 1992; Wolfson 1993; Low & Smith 1993), and the asymptotic properties of sheared coronal fields (Aly 1984, 1985, 1988, 1990). However, a basic problem remains unresolved. Aly (1984, 1991) and Sturrock (1991) have found that the energy in an open-field configuration[1] is an upper limit to the magnetic energy for all force-free equilibria.[2] Therefore, an impulsive transition from a closed, force-free configuration to an open field would appear to be energetically impossible. How then can a phenomenon such as a coronal mass ejection be initiated by magnetic energy release?

To answer this question we have investigated the dynamical evolution of an isolated arcade in axisymmetric spherical geometry using the ideal and resistive magnetohydrodynamic (MHD) models. Although this is an idealized model problem, it significantly extends previous models of coronal fields, and has allowed us to answer several important theoretical questions related to the disruption of coronal arcades. When a dipole field is subjected to a prescribed photospheric shear flow profile, its magnetic energy increases until it approaches the open-field energy, at which point the field configuration becomes very sensitive to additional shear, expanding considerably and producing a concentration of the electric current density. Past a critical level of shear, when the magnetic energy approaches, but is still

---

[1]An open field is a configuration in which one end of every field line intersects the photosphere, the other end extending out to infinity (*e.g.*, Barnes & Sturrock 1972; Sturrock 1991, and Section 5.2 of this paper).

[2]When the configuration has field lines which are not connected to the photosphere, the force-free field energy can exceed the open-field energy (*e.g.*, Priest & Forbes 1990).

below, the open-field energy, the configuration experiences ideal MHD magnetic nonequilibrium, leading to an opening of the field and the formation of a tangential discontinuity in the magnetic field. The assumption of quasi-static behavior (in which the field is assumed to evolve through a series of equilibrium states) breaks down when the critical shear is exceeded, since the equilibration time for the expanding field becomes long, requiring a *dynamical* model to describe the system properly. The appearance of a tangential discontinuity implies that even a small plasma resistivity becomes important. The resistive MHD evolution shows that finite resistivity resolves the tangential discontinuity into a current sheet at which there is rapid reconnection of the magnetic field, leading to the release of magnetic energy, fast flows, and the ejection of a plasmoid, demonstrating that magnetic energy can be released impulsively in a coronal arcade. The opening of the field, and the subsequent reconnection, have been predicted on the basis of the asymptotic properties of sheared force-free arcades (Aly 1985, 1990).

There is considerable confusion in the literature in the terminology that has been used to describe the phenomenon of "absence of MHD equilibrium." The terms "loss of equilibrium" and "magnetic nonequilibrium" have become popular. Although they are used synonymously at times, we wish to distinguish between them. We refer to *magnetic nonequilibrium* as the ideal MHD process by which a plasma with an initially smooth magnetic field evolves into a configuration with inevitable tangential discontinuities in the magnetic field (Parker 1972, 1979;

Priest 1981; Moffatt 1985; Vainshtein & Parker 1986; Vainshtein 1987[3]). In the presence of finite plasma resistivity these tangential discontinuities are resolved into thin layers called current sheets (*e.g.*, Parker 1986). For simplicity we shall loosely refer to both the tangential discontinuities which occur in ideal MHD and the current sheets which occur in resistive MHD simply as current sheets. The term *loss of equilibrium* has been used to describe the disappearance of solutions to the equilibrium equations in response to the variation of an external parameter. [The external parameter could define the magnetic field or pressure profile (*e.g.*, Low 1977; Birn & Schindler 1981), or the displacement of the magnetic field footpoints (*e.g.*, Priest & Milne 1980).] Loss of equilibrium is characterized by the disappearance of a local extremum in the potential energy of the system when the external parameter reaches a critical value. While this "critical" behavior has been interpreted as an eruption of the configuration (Birn & Schindler 1981), it does not necessarily have physical significance (Aly 1985; Klimchuk & Sturrock 1989; Finn & Chen 1990).

In the definition of loss of equilibrium there is no explicit reference to the smoothness of the magnetic field. It is this property that distinguishes magnetic nonequilibrium from loss of equilibrium. Since it is necessary to know the potential energy surfaces of the configuration to determine whether loss of equilibrium has occurred, in our dynamical approach it is not possible to explicitly identify loss of equilibrium. On the other hand, since we can detect when a current sheet forms, it *is possible* to identify the onset of

---

[3]Although this paper illustrates *magnetic nonequilibrium*, the phenomenon has unfortunately been translated from the original Russian as *loss of equilibrium*!

magnetic nonequilibrium. It is conceivable that magnetic nonequilibrium and loss of equilibrium might be related, *i.e.*, that magnetic nonequilibrium might result from loss of equilibrium, but this must be left as an open question.

The topic of true interest is how an arcade evolves subsequent to reaching the critical point. The most appropriate model in this case becomes a dynamical one, in which the time-dependent behavior is followed explicitly. The dynamical approach resolves many questions that have arisen from previous studies of sequences of equilibria. In Section 5.2 we illustrate how magnetic nonequilibrium arises during the dynamical evolution of an arcade in response to photospheric flow.

The main emphasis of this paper is to present a detailed study of the arcade disruption within the ideal MHD model and to indicate its relationship to previous theoretical work. However, we do discuss the general effect of finite plasma resistivity on the disruption in order to contrast it with ideal MHD behavior, and to emphasize the necessity of finite resistivity for impulsive energy release. The resistive behavior will be investigated more thoroughly in a future paper. In Sections 2, 3, and 4, we describe the plasma model, including the initial and boundary conditions and the plasma parameters. In Section 5 we describe our results, and in Section 6 we discuss the implications for the solar corona.

2. MODEL DESCRIPTION

Our motivation is to extend previous studies of the dynamical evolution of coronal arcades (Mikić *et al.* 1988; Biskamp & Welter 1989; Finn

et al. 1992). We adopt a spherical coordinate system, finite plasma pressure, mass evolution, and gravity, and we use nonuniform grid cells to minimize the effect of artificial computational boundaries. We solve the following time-dependent MHD equations numerically in spherical coordinates:

$$\nabla \times \mathbf{B} = \frac{4\pi}{c}\mathbf{J} , \tag{1}$$

$$\nabla \times \mathbf{E} = -\frac{1}{c}\frac{\partial \mathbf{B}}{\partial t} , \tag{2}$$

$$\mathbf{E} + \frac{1}{c}\mathbf{v} \times \mathbf{B} = \eta \mathbf{J} , \tag{3}$$

$$\frac{\partial \rho}{\partial t} + \nabla \cdot (\rho \mathbf{v}) = 0 , \tag{4}$$

$$\rho\left(\frac{\partial \mathbf{v}}{\partial t} + \mathbf{v} \cdot \nabla \mathbf{v}\right) = \frac{1}{c}\mathbf{J} \times \mathbf{B} - \nabla p + \rho \mathbf{g} + \nabla \cdot (\nu \rho \nabla \mathbf{v}) , \tag{5}$$

$$\frac{\partial p}{\partial t} + \nabla \cdot (p\mathbf{v}) = -(\gamma - 1)p\nabla \cdot \mathbf{v} + H, \tag{6}$$

where **B** is the magnetic field intensity, **J** is the electric current density, **E** is the electric field, **v** is the plasma velocity, p and ρ are the plasma pressure and mass density, $\mathbf{g} = -g_0 R_0^2 \hat{\mathbf{r}}/r^2$ is the gravitational acceleration, $g_0 = 2.74 \times 10^4$ cm s^{-2} is the surface gravity, $R_0 = 6.96 \times 10^5$ km is the solar radius, η is the plasma resistivity, ν is the kinematic plasma viscosity, and γ is the ratio of specific heats. In practice, we use the vector potential **A**, where $\mathbf{B} = \nabla \times \mathbf{A}$, to implement the algorithm. This model is applicable to both ideal MHD, in which we set $\eta = 0$, and to resistive MHD, when η is finite. The heating term in the energy equation (6) accounts for heating due to resistive and viscous dissipation, $H = (\gamma - 1)(\eta J^2 + \nu \rho \nabla \mathbf{v} : \nabla \mathbf{v})$. Since numerical resolution

constraints (see the Appendix) limit us to using enhanced values for the resistivity and viscosity compared to coronal values, the associated heating rate may be unphysically large. We therefore frequently neglect this heating by setting $H = 0$; this was done for the simulation described in Section 5.1. We have verified that the magnetic field evolution is insensitive to the presence of this heating term. The plasma beta, defined by $\beta = 8\pi p/B^2$, measures the ratio of plasma to magnetic pressure. These equations are solved in axisymmetric spherical coordinates (r,θ), in the domain $\{R_0 \le r \le R_1;$ $0 \le \theta \le 180°\}$, where r is the distance from the center of the Sun, and θ is the solar latitude (with $\theta = 0$ and $\theta = 180°$ representing the North and South poles). In this two-dimensional approximation all quantities are assumed to be independent of the solar longitude ϕ. In the future we plan to extend this model to problems in which quantities may vary in all three dimensions (r,θ,ϕ). The Alfvén speed is given by $v_A = B/\sqrt{4\pi\rho}$. Distances are normalized by R_0, and the time scale is normalized by the Alfvén time, $\tau_A = R_0/v_A$, corresponding to a length scale R_0, evaluated at the equator at the base of the corona ($r = R_0$, $\theta = 90°$).

The principal results in this paper were calculated using these full MHD equations. In order to understand the nature of the disruption, and to compare directly with previous theory of force-free fields, we have also used a subset of this model: in the *zero-beta* model we neglect the plasma pressure and gravitational forces by setting $p = 0$ and $\mathbf{g} = 0$, and we assume a fixed plasma density profile $\rho(\mathbf{r})$. This model approximates the behavior of the low-beta coronal plasma, and contains the same magnetic phenomena that are present in the full MHD equations. In particular, equilibria in the zero-

beta ideal MHD model are force-free ($\mathbf{J} \times \mathbf{B} = 0$), so that it is possible to compare our results directly to previous analytic and numerical calculations of force-free fields (see Section 5.2).

3. INITIAL CONDITIONS AND PLASMA PARAMETERS

The initial state is a plasma in hydrostatic equilibrium with a dipole magnetic field. The pressure and density profiles are chosen to be spherically symmetric, $p = p(r)$ and $\rho = \rho(r)$, with base values at $r = R_0$ given by p_0 and ρ_0, with a uniform entropy, $p\rho^{-\gamma} = p_0\rho_0^{-\gamma}$. The dipole magnetic field,

$$B_r = \frac{2B_0R_0^3\cos\theta}{r^3}, \quad B_\theta = \frac{B_0R_0^3\sin\theta}{r^3}, \quad B_\phi = 0,$$

is a potential field ($\mathbf{J} = 0$) outside the Sun, $r \geq R_0$. This initial state satisfies the static equations (1)–(6) with $\mathbf{v} = 0$ and $\mathbf{E} = 0$. The explicit solution for the pressure and density is

$$\rho = \rho_0\left[1 - \frac{(\gamma - 1)g_0R_0\rho_0}{\gamma p_0}\left(1 - \frac{R_0}{r}\right)\right]^{1/(\gamma - 1)},$$

$$p = p_0\left(\frac{\rho}{\rho_0}\right)^\gamma.$$

The "photospheric" boundary at $r = R_0$ is to be regarded as the base of the corona (just above the transition region), since we do not attempt to resolve the photospheric scale height; this assumption is appropriate because we are interested in modeling the large-scale ($\sim R_0$) behavior of the corona. The following boundary values (at $r = R_0$) were used: magnetic field strength at the equator $B_0 = 2.2$ G; mass density $\rho_0 = 1.67 \times 10^{-16}$ g cm^{-3} (corresponding to an ion and electron number density $n_0 = 10^8$ cm^{-3}); temperature $T_0 = 1.4 \times 10^6$ K (defined by the ideal gas law $p_0 = 2n_0kT_0$). The ratio of specific

heats is chosen as $\gamma = 1.05$ to produce a temperature which has little variation in the corona (Parker 1963). This hydrostatic atmosphere has plasma properties similar to the large scale corona, but does not include the solar wind. [The solar wind creates a helmet streamer configuration (Pneuman & Kopp 1971); the effects of shear motions on helmet streamer configurations (*e.g.*, Linker, Van Hoven, & Schnack 1990; Linker, Van Hoven, & McComas 1992) are discussed briefly in Section 6, and will be studied in detail in a future paper.] Figure 1 shows the variation of the thermodynamic variables in the hydrostatic equilibrium. At the equator, at $r = R_0$, these parameters give a sound speed $c_s = 157$ km s^{-1}, an Alfvén speed $v_A = 470$ km s^{-1}, and $\beta = 0.2$. At the poles, $v_A = 940$ km s^{-1} and $\beta = 0.05$. The Alfvén time is $\tau_A = 1{,}449$ sec (24.2 minutes).

The Lundquist number S is defined as the ratio of the resistive diffusion time $\tau_R = 4\pi R_0^2/\eta c^2$, to the Alfvén time τ_A. For the Spitzer value of the plasma resistivity at a temperature of 1.4×10^6 K, we find that $S = 5 \times 10^{14}$. This large value of S in the corona makes the *ideal* (*i.e.*, zero resistivity) MHD behavior of coronal fields a topic of interest. As will be shown by the results, our simulations with $\eta = 0$ approximate ideal behavior very closely. During the resistive computations, such a small value of the plasma resistivity cannot be treated accurately in a numerical simulation. For the mesh resolutions used in this paper we have been able to accurately simulate the resistive plasma evolution at the (much-enhanced) uniform resistivity corresponding to $S = 10^4$. The Appendix contains a discussion of the numerical diffusion in the algorithm and the extent to which ideal MHD behavior can be modeled by a numerical solution of the MHD equations. For

a uniform plasma viscosity, the viscous diffusion time is defined by $\tau_\nu = R_0^2/\nu$. Typically, we use a viscosity corresponding to $\tau_\nu = 10^2\tau_A$, although we have used viscosities as small as $\tau_\nu = 10^3\tau_A$.

4. GEOMETRY AND BOUNDARY CONDITIONS

In spherical geometry, two boundaries appear in the simulation: the physical inner radial boundary at $r = R_0$ and an artificial outer radial boundary at $r = R_1$, which we usually place in the range $50–200R_0$. In order to maintain high spatial resolution in particular regions while minimizing the effect of the artificial computational boundary we employ a nonuniform mesh in which the computational cells vary in size. The cell size varies very gradually, so that neighboring cell dimensions are stretched by only a few percent per cell. A typical computational mesh is shown in Figure 2. This mesh has 200×200 r–θ grid points; the outer radial boundary is at $r = 50R_0$; $\Delta\theta$ varies from 0.27° at the equator to 2.7° at the poles; $\Delta r = 0.01R_0$ at the solar surface, increasing gradually to $\Delta r \sim 0.03R_0$ at $r \sim 2R_0$, and to $\Delta r \sim 3R_0$ at $r = 50R_0$. (This mesh was used for the calculations described in Section 5.1.) As will be apparent from the results, a mesh with very small cells in certain regions is required to adequately resolve the steep gradients that form. While such high-resolution grids are desirable for accuracy, they result in stringent time step limitations if a traditional explicit time-integration technique is used. To overcome this difficulty we employ a semi-implicit time-integration scheme in which the time step is limited by accuracy, rather than by numerical stability considerations (see the Appendix).

We now discuss the boundary conditions at the radial boundaries.

Physically, the MHD equations (with finite viscosity) require boundary conditions on all components of the flow velocity, the tangential electric field, and the normal magnetic field. The build-up of magnetic energy in the corona is believed to be driven by flows in the photosphere. Because of the high photospheric mass density and conductivity, convective motions of the plasma in the photosphere tend to move the footpoints of the coronal magnetic field. This situation has been modeled with a "line-tied" boundary condition (Raadu 1972; Einaudi & Van Hoven 1981; Priest 1982). This line-tied boundary condition is implemented at the lower radial boundary by using the "frozen-in" condition given by the ideal Ohm's law,

$$\mathbf{E} + \frac{\mathbf{v}_p \times \mathbf{B}}{c} = 0 \ , \tag{7}$$

where $\mathbf{v}_p$ is the specified photospheric boundary velocity. Only the tangential components of $\mathbf{E}$ are advanced using this ideal Ohm's law at the boundary, since the normal component, E_r, is advanced self-consistently by the normal component of Ohm's law, equation (3), at the boundary (Mikić *et al.* 1988). Since we do not presently include the solar wind, the normal velocity v_r is set to zero, we set $v_\theta = 0$, $v_\phi = v_\phi{}^0$ is a specified shear profile, and p and ρ evolve self-consistently. Equation (7) implies that the tangential electric field at the boundary is given by $E_\theta = -v_\phi{}^0 B_r/c$ and $E_\phi = 0$, guaranteeing that the normal magnetic field (and hence the photospheric flux) is fixed, $\partial B_r/\partial t = 0$. Note that it is not necessary (nor is it appropriate) to specify boundary conditions on the tangential magnetic fields; they evolve self-consistently according to the specified flow. This implementation of boundary conditions is facilitated by the use of staggered grids. When the resistivity is zero, this boundary

condition causes the magnetic field footpoints to move with the applied flow velocity (as verified in Section 5.1); with finite resistivity, there is a small relative slip between the applied flow velocity and the motion of the magnetic field footpoints that is proportional to η (Mikić *et al.* 1988).

The upper radial boundary conditions are implemented to minimize the effect of the boundary on the solution. When solving the full MHD equations, we specify boundary conditions based on the gas characteristics (*e.g.*, Courant & Friedrichs 1948) with a non-reflecting condition for outgoing waves (Heastrom 1979). Neglecting the magnetic field in the characteristic boundary conditions is permissible since β is very high there (for the initial dipole field, $\beta \sim 10^5$ at $r = 50R_0$). The gas characteristics give boundary values for the pressure, density, and the normal (radial) velocity. The tangential electric field is determined using equation (7), and the tangential velocity is advected using the normal velocity. This boundary condition has been found to work well under both subsonic and supersonic outflow conditions—in simulations of helmet streamers an ejected plasmoid propagates out of the upper radial boundary without reflection. In the case of the zero-beta MHD equations, we use a simple outward advection scheme, in which all quantities are advected at the local radial velocity when the flow is directed outward. This *ad-hoc* condition is an improvement over a solid perfectly conducting wall which allows plasma to leave the domain. Since the upper radial boundary is placed far from the Sun ($r = 200R_0$ is almost at the position of the Earth!), we find that the evolution is not sensitive to the exact boundary conditions used (see Section 5.3 for a discussion of the quantitative effect of the upper radial boundary). In general, it ought to be possible to implement

boundary conditions based on the full MHD characteristics (Hu & Wu 1984).

The internal boundaries at $\theta = 0$ and 180° are treated using appropriate geometrical conditions required of analytic functions. Even though all the results presented in this paper have been found to be symmetric with respect to the equator $\theta = 90°$, all the calculations employed a full domain in the region $0 \le \theta \le 180°$, so that anti-symmetric modes were not explicitly excluded.

A shearing motion is introduced by specifying the following longitudinal flow profile v_ϕ^0 at the photosphere:

$$v_\phi^0 = v_0(t)\Theta \exp\left[(1-\Theta^4)/4\right], \tag{8}$$

where $\Theta = (\theta - 90)/\Delta\theta_m$, and $v_0(t)$ is a function which is used to specify the time profile; typically we turn the flow on and off smoothly using a linear ramp over 20–50τ_A. The width of the profile is controlled by $\Delta\theta_m$; the flow is anti-symmetric about the equator $\theta = 90°$, with a minimum $v_\phi^0 = -v_0$ at $\theta = 90 - \Delta\theta_m$, and a maximum $v_\phi^0 = v_0$ at $\theta = 90 + \Delta\theta_m$. We have used $\Delta\theta_m = 20°$, which concentrates the flow near the neutral line (at the equator), and localizes the shear within the region ~ 50°–130°. This flow profile is shown in Figure 3, and is practically identical to that used by Steinolfson (1991), except that it has continuous derivatives for all θ. For $v_0 > 0$, the field lines near the equator in the Northern hemisphere are moved in the $-\phi$ direction, while those in the Southern hemisphere are moved in the $+\phi$ direction. Figure 4 shows a three-dimensional view of the sheared field lines. This flow is not intended to represent observed large-scale flows; it is merely an idealized flow which produces shear near the neutral line. It is convenient to quantify the applied shear using the distance

$$\Delta s_{max} = \int_0^t v_0(t')\, dt' \ , \tag{9}$$

which is seen to be the maximum distance that a field line footpoint moves in the longitudinal direction. For the shear profile given by equation (8), the field line with footpoints at $\theta = 90 \pm \Delta\theta_m$ therefore has a total displacement between its footpoints equal to $2\Delta s_{max}$ along the Sun's surface in the ϕ direction.

5. RESULTS

In this section we describe the evolution of coronal arcades. In Section 5.1 we contrast the ideal and resistive MHD evolution, and we show that resistive evolution can lead to the disruption of an arcade. In Section 5.2 we use the zero-beta MHD equations to identify the cause of the disruption, and in Section 5.3 we analyze the results using the virial theorem.

5.1. *Arcade Evolution and Disruption*

We first discuss the evolution of an arcade for a typical calculation. The photospheric flow velocity $v_0(t)$ was increased from zero (linearly in time) to 1.9 km s^{-1} from $t = 0$ to $t = 20\tau_A$; it was kept constant until $t = 500\tau_A$, when it was decreased to zero (linearly in time) at $t = 520\tau_A$; the flow remained zero for $t \geq 520\tau_A$. The full MHD equations (1)–(6) were solved, starting from the initial conditions described in Section 3. The outer radial boundary was placed at $r = 50R_0$. We describe two calculations which contrast the difference between the ideal and resistive evolution. Case 1 is an ideal MHD run (with $\eta = 0$), which was run until $t = 900\tau_A$. Case 2 is identical to case 1 until $t = 520\tau_A$, but a uniform resistivity corresponding to $S = 10^4$ is

introduced at $t = 520\tau_A$ (when the photospheric flow has been turned off).

Figure 5 shows contours of the flux function $\psi = r\sin\theta A_\phi$ during the ideal evolution (case 1). Contours of ψ correspond to projections of the magnetic field lines in the r–θ plane. The field lines rise in response to the applied photospheric shear (Figs. 5*a*–*c*) as electric current is induced in the corona and a longitudinal field B_ϕ develops. As the shear approaches $\Delta s_{max} = 1.8R_o$ (Fig. 5*d*), the field lines begin to rise dramatically when additional shear is applied. This expansion of the upper field lines is accompanied by a squeezing of the lower field lines near the equator in the region $r = 2$–$3R_o$, as seen in Figure 5, and a corresponding concentration of the azimuthal current density J_ϕ. It will be shown in Section 5.2 that this sensitivity is indicative of a fundamental change in the properties of the equilibrium magnetic field. The state at $t = 520\tau_A$ and beyond has $\Delta s_{max} = 2.0R_o$. Once the shear is tuned off, the configuration does not change significantly in the strong-field regions (Figs. 5*e*–*f*).

When a finite resistivity is introduced at $t = 520\tau_A$ (case 2), the subsequent resistive evolution is markedly different from the ideal evolution. Figure 6 shows the flux contours during the resistive evolution, demonstrating that the state with $\Delta s_{max} = 2.0R_o$ is susceptible to rapid magnetic reconnection. The reconnection causes an X-point to form, creating an island (O-point) in the flux. The field lines in this "plasmoid" lose their connection to the photosphere, causing the plasmoid to travel upward (Figs. 6*e*–*f*). (In our two-dimensional model this plasmoid is an axisymmetric torus of helical field lines.) The reconnection is accompanied by a current sheet and fast flows, resulting in the dissipation of a substantial fraction of the

magnetic energy. Contours of the current density J_ϕ are plotted in Figure 7 at $t = 549.3\tau_A$ (corresponding to the flux plot shown in Fig. 6*d*), showing the equatorial current sheet at the reconnection site. Figure 8 shows the poloidal $(r-\theta)$ component of the flow in the vicinity of the reconnection site, superimposed on the flux contours, at the same instant. The flow is seen to jet out of the reconnection region in the familiar manner, with a maximum speed that approaches 600 km s^{-1}. Figure 9 shows the magnetic energy W for cases 1 and 2, normalized by the potential field energy, $W_{pot} = B_0^2 R_0^3/3$. Note the stark difference between the ideal and resistive results: whereas the ideal MHD evolution shows that the magnetic energy remains approximately constant after the shear is turned off, the resistive MHD evolution shows that a significant fraction of the free magnetic energy is dissipated. Figure 10 shows the large increase in kinetic energy K during the reconnection.

We have computed the energy conservation as a check on the accuracy of the numerical method. For the ideal MHD run, the total energy (magnetic, thermal, and kinetic) is conserved to within –0.2% (when account is taken of energy that leaves or enters the domain, dissipation, and work done against gravity). There is a large reservoir of thermal energy that does not change substantially during the arcade evolution; when measured in terms of W_{pot}, the energy error is –2.7%. This demonstrates the good energy conservation properties of the code, since the magnetic energy increases by 64% of W_{pot} during the ideal evolution. Energy conservation deteriorates during the resistive run, as expected, since the resolution is not as good during the impulsive phase of the run when fast flows and a current sheet appear; the total energy error is –0.7% (*i.e.*, –9% of W_{pot}). These negative energy errors

indicate that there is additional (numerical) diffusion in the algorithm, as expected from the upwind treatment of advective terms (see the Appendix). This numerical diffusion indicates that the effective Lundquist number during the impulsive phase is closer to $S = 7 \times 10^3$, rather than the assumed value $S = 10^4$. During the resistive run, the magnetic energy that is lost (34% of W_{pot}) and the thermal energy that is lost or flows out of the domain (7%) is distributed as follows: 18% is dissipated resistively, 4% is dissipated viscously, 0.5% goes into kinetic energy, 9.5% does work against gravity, and 9% is presumably dissipated by numerical diffusion. [In this run we neglected the heating due to resistive and viscous dissipation by setting $H = 0$ in equation (6). Therefore, the dissipated energy does not appear as heat, but is lost from the system, though it is accounted for in the energy conservation check.]

As one test of how closely the simulation approximates ideal behavior with $\eta = 0$, and to check the accuracy with which the line-tied boundary conditions have been implemented, we have explicitly traced the field lines at the end of the ideal MHD evolution at $t = 900\tau_A$. Figure 11 shows a comparison between the actual longitudinal field line footpoint positions and the positions expected due to the applied flow. The applied shear is $\Delta s_{max} = 2.0R_0$, which implies that the maximum longitudinal displacement between field line footpoints ought to equal $4.0R_0$ (for the field line with footpoints at $\theta = 70°$ and 110°), as shown in Figure 11. Note the excellent agreement between the expected and actual footpoint positions (maximum error $\lesssim 0.05R_0$), indicating that the line-tied boundary conditions have been implemented accurately. When we perform a simulation in which a

nonzero η is present during the shearing phase, some slippage of the field lines does occur (Mikić *et al.* 1988), and the magnetic energy build-up is slightly smaller. When η is nonzero, there is some slippage which is proportional to η. (The slippage velocity is on the order of $10^{-4}v_A$ at $S = 10^4$, which is small compared to the maximum drive velocity.) However, the qualitative evolution of the arcade (and, in particular, the disruption) is similar to the case shown.

When the applied shear is smaller than the critical shear (which we estimate as approximately $\Delta s_{max} \sim 1.6R_0$), the evolution of the arcade is quasi-static; *i.e.*, if at any point we turn off the shear velocity and allow the system to relax to an equilibrium, the configuration changes very little. When v_0 is well below v_A, the magnitude of the shear velocity determines only how quickly a particular state is reached, but does not affect the nature of the equilibrium for a given applied shear. We have verified that when $\Delta s_{max} \leq 1.6R_0$, the configuration settles to an equilibrium when $\eta = 0$. In the presence of finite resistivity, the currents in the configuration diffuse at a rate that is directly proportional to η. There is no impulsive dynamical behavior.

At larger values of the shear, the solutions undergo a dramatic transition. The configuration becomes very sensitive to additional shear, and the higher field lines rise significantly. At this point the configuration is susceptible to magnetic reconnection when resistivity is present, as described above. When the applied shear is close to the critical shear the resistive disruption proceeds slowly; however, when the critical shear is exceeded significantly, the onset of reconnection is more rapid, and the reconnection itself becomes increasingly more vigorous. A detailed study of this

reconnection (in particular, its rate as a function of S) will be deferred to a future investigation.

These results indicate that, in the presence of resistivity, an isolated arcade disrupts when sufficient shear is applied, with significant liberation of magnetic energy, resulting in fast flows and ejection of a plasmoid. In the next section we investigate the underlying cause of the disruption within the context of the ideal, zero-beta MHD model, and we explore its relation to previous work on force-free equilibria.

5.2. *Zero-Beta Model*

Solution of the zero-beta resistive MHD equations shows that the evolution of the magnetic field is qualitatively similar to that found using the full MHD equations, as described in the previous section, indicating that the phenomenon leading to the disruption of the arcade is magnetic in nature. The evolution for small shear is quasi-static, and the field disrupts beyond a critical shear threshold.

We have generated a sequence of ideal MHD force-free equilibria by applying a velocity $v_0 = 0.94$ km s^{-1} for different durations to achieve shears of $\Delta s_{max} = 1.2, 1.4, 1.6, 1.8, 2.0$, and $2.2R_0$. After the flow velocity was turned off, the simulations were run until the field approached a steady state. The outer radial boundary was placed at $r = 200R_0$. Since our primary intention in this section is to determine force-free equilibria, we chose a (fixed) density profile $\rho = \rho_0(R_0/r)^4$, which produces an Alfvén speed that is approximately uniform for an open field. This density profile is similar in the lower corona to that for hydrostatic equilibrium, but falls off more rapidly at larger r, so that the equilibration rate of the weak magnetic fields in the outer corona is

enhanced. (By using different density profiles we found that the qualitative behavior to be described does not depend on the detailed form the density profile, although the time scales may be affected by the Alfvén speed.) Figure 12 shows contours of ψ for these equilibria. A transition in the nature of the equilibria is evident: when $\Delta s_{max} \leq 1.8R_o$, all the field lines are closed, but at higher shears "open" field lines appear. [Although these field lines may not be strictly open, *i.e.*, they may close at infinity or at a large distance from the Sun, they can be considered to be open for all intents and purposes (Sturrock 1991).] The corresponding contours of J_ϕ (Fig. 13) show that this transition is accompanied by the formation of a current sheet, *i.e.*, a tangential discontinuity in the magnetic field; Figure 14 shows that B_r approaches a function which has a discontinuity on the equator. Note that the magnitude of the maximum current density shown in Fig. 13 increases dramatically as the field opens; the current density would be infinite at a true discontinuity in B_r. It is not usually possible to find ideal MHD numerical solutions with discontinuities unless special care is taken. In the absence of resistivity, a current sheet usually collapses to the mesh size and generates unphysical oscillations, terminating the simulation. Fortunately, we have been able to exploit the symmetry in the present configuration (the current sheet appears exactly on the equator) to carefully formulate the solution across the equator, allowing B_r to approach a discontinuous solution (see the Appendix).

It is important to note that we have not proved conclusively that the magnetic field becomes discontinuous. In our numerical scheme we cannot rule out the possibility that the magnetic field changes over a narrow layer (of finite, rather than zero, width), although it is not readily apparent what

physical process would set the width of this layer. The fact that the field approaches the open field (which has a true discontinuity in the magnetic field) leads us to adopt the hypothesis that the field approaches a true discontinuity.

The "open-field" configuration has been introduced as the asymptotic state of highly sheared force-free equilibria (Barnes & Sturrock 1972; Aly 1984, 1991; Yang *et al.* 1986; Sturrock 1991). For a given force-free field, the corresponding open field is defined as the field with the same photospheric flux, but in which the ends of all field lines that intersect the photosphere extend to infinity [see Barnes & Sturrock (1972) for a specific example]. The magnetic field in the open configuration is potential everywhere except in isolated regions in which current sheets (tangential discontinuities in the magnetic field) separate oppositely directed field lines. The energy in an open-field configuration is an upper limit to the magnetic energy for all force-free equilibria (Aly 1984, 1991; Sturrock 1991). For the particular case of a dipole flux distribution, we have computed the open field using the expedient (involving a monopole field) suggested by Barnes & Sturrock (1972). This open field has a discontinuity in B_r at the equator, and has a magnetic energy $W_{open} = 1.662 W_{pot}$. The field lines in the open field are compared to those in the equilibrium with $\Delta s_{max} = 2.2 R_0$ in Figure 15.

Figure 16 shows the height of several field lines in the force-free equilibria as a function of applied shear. The field line height increases steadily with shear, but becomes very sensitive to shear when a critical shear is approached, corresponding to the transition described above. Several aspects of this transition should be noted. First, although a fundamental

change occurs in the magnetic configurations for the higher shear cases, there is no impulsive release of magnetic energy when resistivity is absent. Beyond a critical shear, in the ideal MHD model the field lines slowly expand outward, opening the field and creating a current sheet (Figs. 12 and 13). Second, the reconnection which occurs during the resistive MHD evolution is directly related to the transition in the ideal equilibria. There is no disruption below the critical shear, whether or not resistivity is present. Third, although a current sheet forms in the cases with $\Delta s_{max} = 2.0$ and $2.2R_o$, the magnetic energy remains below the open-field energy throughout the evolution. Figure 17 shows the magnetic energy in the force-free equilibria as a function of applied shear. Note that magnetic energy approaches the open-field energy for large shear, and that the field begins to open (at $\Delta s_{max} = 2.0$ and $2.2R_o$) while W is still below W_{open}, so that these fields represent *partially open* magnetic configurations. The case with $\Delta s_{max} = 2.2R_o$ has closed field lines corresponding to ~ 3% of the flux (these are the low-lying field lines near the equator in Fig. 15*a*). We have made conservative error estimates of W for the cases with $\Delta s_{max} = 2.0$ and $2.2R_o$ (indicated by the error bars in Fig. 17), since the fields have not reached a complete steady state by the end of the runs. Our results for the magnetic energies of force-free equilibria are therefore in agreement with those of Aly (1984, 1991) and Sturrock (1991).

It is illuminating to examine the evolution of the toroidal (B_ϕ) and poloidal (B_r, B_θ) components of the magnetic field in response to the applied shear. Figure 18 shows the evolution of the "partial magnetic energies" W_r, W_θ, and W_ϕ, where we have defined $W_r = \int B_r^2 \, dV/8\pi$, and similarly for W_θ and W_ϕ, for the case $\Delta s_{max} = 2.0R_o$. Initially, as the field is sheared, poloidal

field is converted into toroidal field (*i.e.*, W_θ decreases and W_ϕ increases); however, as additional shear is applied, the expansion of the arcade causes W_ϕ to decrease (Aly 1990), and W_r to increase, as the field becomes more radial. The partially open field has a small residual toroidal field (in the closed-field region). For comparison, note that the fully open field has $W_r = 1.597 W_{pot}$, $W_\theta = 0.065 W_{pot}$, and $W_\phi = 0$.

The presence of gravity in the full MHD equations would be expected to impede the opening of the field. This is evident from Figures 5 and 12, which show that whereas a shear of $\Delta s_{max} = 2.0 R_0$ is sufficient to open the field in the zero-beta model, the corresponding full MHD configuration (with gravity) has closed field lines. When the shear is large, the full (ideal) MHD model shows that the configuration also approaches an open field. (This is of purely theoretical interest, since it is the resistive evolution that is relevant to the Sun, and we have already shown in Section 5.1 that the arcade disrupts within the full MHD model.)

5.3. *Application of the Virial Theorem*

The transition in behavior past the critical shear can be analyzed using the scalar virial theorem (*e.g.*, Aly 1984). A force-free field in equilibrium must satisfy the following equality:

$$\int_V \frac{B^2}{2} dV = -\int_S \left((\mathbf{B}\cdot\hat{\mathbf{n}})(\mathbf{B}\cdot\mathbf{r}) - \frac{B^2}{2}(\mathbf{r}\cdot\hat{\mathbf{n}}) \right) dS \ , \qquad (10)$$

where V is the volume of the domain, S is the surface bounding the volume, and $\hat{\mathbf{n}}$ is the unit outward normal. We refer to the right-hand-side of equation (10) as the surface term. In our spherical domain with boundaries at $r = R_0$ and $r = R_1$ we can thus write:

$$W \equiv \int_V \frac{B^2}{8\pi} dV = S(R_0) - S(R_1) \ , \tag{11}$$

where

$$S(r) = \frac{r^3}{4} \int_0^\pi (B_r{}^2 - B_\theta{}^2 - B_\phi{}^2) \sin\theta \, d\theta \ . \tag{12}$$

How closely W and the surface term match each other is a measure of how close a configuration is to equilibrium at a given time. Figure 19 shows the evolution of W and the surface term for the case with $\Delta s_{max} = .0 R_0$. During the early part of the evolution, W and the surface term match closely, verifying that the evolution is quasi-static, but at $t \sim 925 \tau_A$ (when Δs_{max} begins to exceed $1.8 R_0$), the two curves start to diverge, indicating that the system is no longer in equilibrium. This has been identified as the onset of magnetic nonequilibrium (Section 5.2). The two curves approach each other as the system equilibrates, although the equilibration time is long. Figure 20, which shows the evolution of the height of selected field lines at the equator, indicates that the upper field lines rise slowly as the field opens. The long equilibration time can be attributed to the slow expansion of the weak upper magnetic fields in a region with small Alfvén speed.

The expansion which occurs during the opening of the field in the full MHD model is also characterized by a long equilibration time, as a result of the small Alfvén speed in the outer corona. It takes thousands of Alfvén times for the field to equilibrate ($1000 \tau_A$ corresponds to 16.8 days), implying that the quasi-static approximation is no longer valid once the critical shear is reached, even for small photospheric flow speeds. (The field equilibrates on the *local* Alfvén time scale, which can be much longer in the weak-field regions in the outer corona than the "characteristic Alfvén time scale" τ_A.)

An accurate estimate of the equilibration time depends on the thermodynamic model of the outer corona. In particular, a solar wind solution has a smaller density in the outer corona than that predicted by the hydrostatic model. An important consequence of this slow equilibration is that *nonequilibrium* magnetic fields with energies exceeding W_{open} may form in the corona. We have verified that W_{open} can be exceeded in the full MHD model when the arcade is driven continuously with a photospheric shear velocity $v_0 = 0.94$ km s^{-1}.

In order to illustrate the approach to equilibrium when the critical shear is not exceeded, Figure 21 shows W and the surface term for the case $\Delta s_{max} = 1.8R_0$. The evolution is seen to be quasi-static at all times, with the field settling to equilibrium relatively quickly when the shear flow is turned off at $t = 950\tau_A$, as shown by the evolution of the field line height (Fig. 22). The residual difference ($\sim 5 \times 10^{-4} W_{pot}$) that remains between the W and surface term curves in Figures 19 and 21 is a measure of the differencing error involved in the computation of the various terms.

The quantitative influence of the upper radial boundary on the solution can be measured by comparing the relative sizes of the three terms in equation (11). For the case $\Delta s_{max} = 2.0R_0$, we find that $S(R_1)$ remains negligibly small during the quasi-static evolution, increasing as the field begins to open. Even then, its maximum value (at $t \sim 1700\tau_A$) is only $10^{-3} W_{pot}$ (*i.e.*, W and $S(R_0)$ balance to within 1 part in 10^3), indicating that it plays a minimal role in the energetics of the field. This demonstrates that the upper radial boundary is sufficiently far away so as to have a negligible effect on the computed solution.

6. DISCUSSION

The results presented in detail in the preceding section can be summarized as follows. A sheared arcade responds to slow photospheric flows quasi-statically, evolving through sequences of equilibria with increasing magnetic energy. With increasing shear, the field lines rise dramatically. When a critical shear is exceeded the arcade suffers magnetic nonequilibrium: the arcade expands outward from the Sun in a process that opens magnetic field lines and forms a current sheet. The current sheet results from a tangential discontinuity in the magnetic field which separates the two regions of opposite polarity. In the ideal MHD model this opening of the field is not very impulsive, and does not produce a large change in magnetic energy. It is characterized by a long equilibration time, since it involves expansion of weak outer magnetic fields. In marked contrast, when finite resistivity is present there is a violent disruption of the configuration resulting from magnetic reconnection at the current sheet, leading to Alfvénic flows, considerable dissipation of magnetic energy, and the ejection of a plasmoid. This disruption occurs in both the full MHD model and the zero-beta model; therefore, it is a property of the magnetic configuration of the arcade.

For the force-free equilibria found in the zero-beta model, the magnetic energy remains below the open-field energy (Aly 1984, 1991; Sturrock 1991). The critical shear at which magnetic nonequilibrium occurs corresponds to a magnetic energy $W_{crit} \sim 1.62 W_{pot}$, which is slightly (but definitely) below the open-field energy, $W_{open} = 1.662 W_{pot}$. Thus, following magnetic nonequilibrium, the field reaches a partially open configuration in which the

majority of the field lines open, with a small fraction of the low-lying field lines remaining closed. When the critical shear is exceeded the arcade evolution is not quasi-static, indicating that a sequence of equilibria may not model coronal evolution accurately during this phase.

In a study of ideal MHD force-free equilibria of an axisymmetric model of a sunspot, Barnes & Sturrock (1972) and Yang *et al.* (1986) did not identify the critical behavior described here. As we have noted, within the ideal MHD model the consequences of magnetic nonequilibrium are not very dramatic—the field expands slowly toward an open configuration, with the eventual formation of a current sheet. The equilibration time for this expansion can be long compared to the characteristic Alfvén time at the base of the arcade. [The critical behavior may be even less apparent in a numerical calculation of the equilibrium field: the current sheet may be artificially broadened by the finite resolution of the grid; the expansion of the field may be inhibited by the proximity of computational boundaries; and the long equilibration time may result in slow convergence toward the open field. These complications were recognized by Porter *et al.* (1992): the large uncertainties in the magnetic energy estimates of computed force-free equilibria were attributed to limited spatial resolution and the proximity of computational boundaries.] It is entirely possible that this sunspot field may also experience magnetic nonequilibrium when the magnetic field energy approaches W_{open}. It may prove worthwhile to revisit the study of the ideal and especially the resistive MHD properties of this configuration in light of the present results.

The disruptive behavior exhibited by a sheared arcade is not unlike that seen in previous computations of arcade evolution in Cartesian

coordinates. In a very idealized model (which had an artificial array of periodic arcades), it was found that arcades disrupted when a critical shear was exceeded (Mikić *et al.* 1988). In that case the mechanism which initiated the disruption was ideal MHD instability in a highly symmetric equilibrium, although a similar effect was also observed in nonsymmetric arcades (Biskamp & Welter 1989). Finn *et al.* (1992) have discussed the effect of symmetry on the relationship between instability and loss of equilibrium in coronal arcades. These studies have shown that coronal arcades can disrupt through resistive reconnection of magnetic field lines in the presence of plasma resistivity. Biskamp & Welter (1989) concluded that "single" arcades did not experience disruptive behavior in Cartesian geometry (*i.e.*, with translational symmetry), in contrast with the disruption observed in groups of adjacent arcades, although this conclusion was not based on an exhaustive parameter study. In contrast, we have shown that a "single" arcade can indeed disrupt. In the (infinitely periodic) configuration studied by Mikić *et al.* (1988), the corresponding open-field energy is infinite (even when measured per arcade, per unit length in the ignorable direction); this is a direct consequence of the assumption of translational symmetry. It is thus not possible to interpret that disruption as the approach of the magnetic energy towards the open-field limit.

A significant disagreement between our results and those of Steinolfson (1991) should be noted. Since our dynamical model is similar to that used by Steinolfson, our results ought to give a comparable description of arcade evolution. The differences in the results must be attributed to differences in the numerical solution of the same physical equations.

Steinolfson notes that the evolution of an arcade is very different depending on which particular scheme is used to advance the tangential field B_ϕ at the photospheric boundary (in one case the field disrupts and in another it does not). As noted in Section 4, a boundary condition on B_ϕ is not allowed in a proper formulation; when line-tying is specified properly, B_ϕ must be evolved self-consistently at the boundary. We have verified that our line-tied boundary condition has been implemented accurately (see Figure 11). The nature of the eruptive behavior reported by Steinolfson is different from the disruption we have described: Steinolfson (1991, Figs. 3, 8, and 9) shows that the magnetic energy increases by many orders of magnitude when the field disrupts, whereas we have shown that the magnetic field is the source of energy for the disruption, so that the magnetic energy *decreases* (as shown in Fig. 9). Steinolfson does not identify the nature of his disruption, nor does he explain the source of energy; in contrast, we have explicitly traced the cause of the disruption to magnetic nonequilibrium (Section 5.2), and we have checked that energy is conserved (Section 5.1). Therefore, the physical relevance of Steinolfson's result must be questioned.

The analytic MHD properties of an idealized model of a coronal arcade with an embedded filament have been studied previously (Priest & Forbes 1990; Forbes & Isenberg 1991). Forbes and Isenberg (1991) found that a filament can experience loss of equilibrium in ideal MHD when the flux in the filament is varied, although the energy release associated with this event is small (less than ~ 1% change in magnetic energy). Forbes & Isenberg (1991) and Forbes (1991) have recognized that it is not necessarily the ideal MHD energy release associated with loss of equilibrium that drives a coronal mass

ejection; it is the subsequent reconnection that releases a substantial amount of magnetic energy. As we have demonstrated, once a current sheet forms even a small plasma resistivity is effective in dissipating magnetic energy and causing plasmoid ejection. Finn & Guzdar (1993) have examined the relationship between loss of equilibrium and reconnection in laboratory and solar plasmas.

Although the present model is highly idealized, it is just this type of magnetic energy conversion and plasmoid ejection that is required to explain coronal mass ejections. In order to make a detailed comparison with observations of coronal mass ejections it will be necessary to further refine this model. In particular, we will add the important effect of the solar wind (Parker 1963). The solar wind opens some of the outer field lines, creating a helmet streamer configuration (Pneuman & Kopp 1971; Linker *et al.* 1990, 1992). Our preliminary results indicate that a similar disruption also occurs in a sheared helmet streamer configuration. In this regard, we conjecture that coronal mass ejections are most frequently observed to occur in helmet streamer configurations because the field is already partially open in such a configuration (by the effect of the solar wind), so that a smaller amount of shear may be required to disrupt the field. In future work we will study in detail the effect of shear on helmet streamers.

It does not appear to be necessary for the coronal arcade to have dimensions comparable to the solar radius for this disruption to occur (as is the case in the model problem described here). We therefore speculate that active-region-sized arcades ought to exhibit similar behavior.

In closing, we note that this example offers a good illustration of the

mechanism of topological dissipation through magnetic nonequilibrium (Parker 1972). It shows that continuous long-wavelength displacements of field line footpoints of a magnetic field configuration (which initially has no neutral points) eventually lead to the formation of a tangential discontinuity, as a consequence of constraints imposed by ideal MHD equilibrium. In the presence of finite resistivity the resulting current sheet is seen to be the site of rapid reconnection, and leads to dissipation of magnetic energy.

ACKNOWLEDGMENTS

We thank Dr. Samuel Vainshtein for his hospitality during a visit by one of us (ZM) to the University of Chicago, and for his suggestion of using the virial theorem to diagnose magnetic nonequilibrium. We thank our colleague Dr. Dalton Schnack for many helpful suggestions. It is a pleasure to acknowledge stimulating discussions with Drs. S. Antiochos, J. Finn, T. Forbes, A. Hassam, J. Klimchuk, E. Parker, G. Roumeliotis, G. Van Hoven, and R. Wolfson. This research was supported by NSF grant ATM-9296165 to UCSD and SAIC, by NASA Supporting Research and Technology contract NASW-4728 to SAIC, and by NASA Space Physics Theory grant NAG5-1492 to UCSD. Computational facilities were provided by NSF at the San Diego Supercomputer Center, and by the U. S. Department of Energy at the National Energy Research Supercomputer Center.

APPENDIX

In this appendix we describe some details of the numerical simulation code. The MHD equations (1)–(6) are integrated using finite differences in space and time. A leapfrog time integration scheme is used, combined with a semi-implicit method. The semi-implicit method allows the time step to exceed the Courant limit, which can make the computation more efficient than one employing an explicit method. In the semi-implicit method (Harned and Kerner 1985; Schnack *et al.* 1987; Mikić *et al.* 1988) the time step is chosen according to accuracy constraints, rather than by numerical stability limitations. Unconditional stability (to wave-like modes) is achieved by introducing an implicit linear operator in the momentum equation which modifies the dispersion properties of high-k modes (where k is the spatial wave vector). These are the modes which are not represented accurately by the spatial differencing. This scheme is particularly efficient when the slow evolution involves long wavelengths (which are treated accurately), but a high-resolution mesh is present to capture the strong gradients that form during a subsequent impulsive phase. This is precisely the situation that occurs in the arcade evolution. The field evolves quasi-statically in response to slow, long-wavelength photospheric flows, but eventually a current sheet forms, and, in the resistive case, reconnection produces large flows. A relatively large time step can thus be used during the quasi-static phase, with a corresponding reduction during the impulsive phase. The (explicit) advection time step limit provides a natural control of the time step, since it automatically reduces the time step when flows become large. The size of the

semi-implicit term depends on the size of the time step; it vanishes when the time step satisfies the Courant condition. In addition, since the semi-implicit term involves a time derivative, it does not affect the steady-state solutions of the equations. The matrices arising from the semi-implicit and fully implicit viscosity operators are inverted using a preconditioned conjugate gradient method (Mikić and Morse 1985).

As a particular example, for the mesh used in Section 5.1 (shown in Fig. 2), the explicit Courant limit for Alfvén waves is $\Delta t < 0.004\tau_A$. Thus, to integrate the equations for $2000\tau_A$ (as was necessary) would require 500,000 time steps. Clearly, the evolution does not suggest that this level of accuracy is required. With the semi-implicit method we were able to use a time step in the range $\Delta t = 0.025$–$0.1\tau_A$ during the quasi-static evolution, with sufficient accuracy and a substantial savings of computer time. We did not find significant differences in selected computations when we varied the time step.

Staggered spatial meshes, in which the various fields are defined at different (staggered) locations with respect to each other, were employed. Such meshes facilitate the implementation of boundary conditions, since it is not necessary to specify quantities that do not require a boundary condition, and preserve the vector identities $\nabla\cdot\nabla\times\mathbf{A} = 0$ and $\nabla\times\nabla\phi = 0$ in discretized form, leading to strict separation of longitudinal and transverse components of a vector. In particular, this implies that $\nabla\cdot\mathbf{B} = 0$ is maintained to within roundoff error during the entire computation.

We now discuss how numerical diffusion is controlled in the code. When numerical solutions of the ideal MHD equations are attempted, the

following question inevitably arises: how accurately is it possible to maintain the constraints imposed by $\eta = 0$? The answer depends to a large extent on the design of the simulation code and the physics of the problem being studied. In general, if the evolution generates gradients that are steeper than can be resolved on the mesh, the numerical solution will cease to be valid: typically, oscillations will develop, causing the simulation to terminate. Sometimes it is preferable to avoid this termination by introducing numerical diffusion to prevent the gradients from steepening beyond that allowed by the mesh resolution, in which case the solution does not represent the ideal evolution, but one with small, but finite, resistivity.

Numerical diffusion in our code can be introduced by using upwind (rather than centered) differences of advective terms. Typically we use upwind differences when advecting velocity, pressure, and mass, which introduces numerical diffusion that has the effect of diffusing steep gradients in momentum, mass, and energy. When studying ideal MHD we use centered differences to advect the vector potential, to prevent the introduction of numerical diffusion in Ohm's law. As a consequence, the ideal MHD constraints prohibiting reconnection are preserved. However, if the ideal evolution causes a current sheet to form, the simulation will terminate unless a specialized treatment is used in the regions where the magnetic field becomes discontinuous. When we use the resistive model, we find that it is sometimes beneficial to use upwind differencing when advecting the vector potential, which introduces a small amount of additional diffusion in Ohm's law. This is the source of most of the energy error discussed in Section 5.1.

In the present arcade evolution, the current sheet that forms with the onset of magnetic nonequilibrium occurs exactly on the equator, and is characterized by a discontinuity in B_r; however, the symmetry of the situation can be exploited. The field approaches an open field, in which this discontinuity is in force balance: although B_r changes sign discontinuously across the equator (*i.e.*, B_r jumps from $-B_e$ to $+B_e$), the magnetic pressure B_e^2 remains continuous across the equator. This implies that the part of the θ-component of the $\mathbf{J} \times \mathbf{B}$ force which equals $-(B_r/r)\partial B_r/\partial\theta$ ought to be differenced in the form $-(1/2r)\partial B_r^2/\partial\theta$, with a choi of staggering in which the B_r mesh-points straddle (but do not fall on) the equator. When the equations are differenced in this form, the approach to a discontinuous solution can be accommodated in the ideal MHD model without introducing numerical diffusion in Ohm's law.

That this technique can successfully handle a current sheet on the equator is illustrated by the stark difference between the ideal and resistive evolution (see Fig. 9), which indicates that the reconnection is controlled by the physical resistivity. We have found that in the ideal model, numerically induced reconnection is absent when this technique (and sufficient resolution) is used.

The code has been designed to run on supercomputers (we used Cray-YMP and Cray-YMP/C90 machines), and takes anywhere from a few minutes to many hours of CPU time, depending on the parameters.

REFERENCES

Aly, J. J. 1984, ApJ, 283, 349

———. 1985, A&A, 143, 19

———. 1988, A&A, 203, 183

———. 1990, Comput. Phys. Comm., 59, 13

———. 1991, ApJ, 375, L61

Barnes, C. W., & Sturrock, P. A. 1972, ApJ, 174, 659

Birn, J., & Schindler, K. 1981, in Solar Flare Magnetohydrodynamics, ed. E. R. Priest (London: Gordon & Breach), p. 337

Biskamp, D., & Welter, H. 1989, Sol. Phys., 120, 49

Canfield, R. C., de La Beaujardière, J.-F., Fan, Y., Leka, K. D., McClymont, A. N., Metcalf, T. R., Mickey, D. L., Wülser, J.-P., & Lites, B. W. 1993, ApJ, 411, 362

Courant, R., & Friedrichs, K. O. 1948, Supersonic Flow and Shock Waves (New York: Wiley-Interscience)

De Vore, C. R., & Antiochos, S. K. 1993, Trans. AGU, 74, 242

Einaudi, G., & Van Hoven, G. 1981, Phys. Fluids, 24, 1092

Finn, J. M., & Chen, J. 1990, ApJ, 349, 345

Finn, J. M., Guzdar, P. N., & Chen, J. 1992, ApJ, 393, 800

Finn, J. M., & Guzdar, P. N. 1993, Phys. Fluids B, submitted

Forbes, T. G. 1990, J. Geophys. Res., 95, 11919

———. 1991, Geophys. Ap. Fluid Dyn., 62, 15

———. 1992, in Eruptive Solar Flares (Proc. 133rd IAU Colloquium, Iguazu, Argentina) ed. Z. Svestka, B. V. Jackson, & M. E. Machado (Berlin:

Springer-Verlag), p. 79

Forbes, T. G., & Isenberg, P. A. 1991, ApJ, 373, 294

Gary, G. A., Moore, R. L., Hagyard, M. J., & Haisch, B. M. 1987, ApJ, 314, 782

Hagyard, M. J. 1988, Sol. Phys., 115, 107

Harned, D. S., & Kerner, W. 1985, J. Comput. Phys., 60, 62

Hedstrom, G. W. 1979, J. Comput. Phys., 30, 222

Hu, Y. Q., & Wu, S. T. 1984, J. Comput. Phys., 55, 33

Inhester, B., Birn, J., & Hesse, M. 1992, Sol. Phys., 138, 257

Isenberg, P. A., Forbes, T. G., & Démoulin, P. 1993, ApJ, 417, 368

Klimchuk, J. A., Sturrock, P. A., & Yang, W.-H. 1988, ApJ, 335, 456

Klimchuk, J. A., & Sturrock, P. A. 1989, ApJ, 345, 1034

———. 1992, ApJ, 385, 344

Leka, K. D., Canfield, R. C., McClymont, A. N., de La Beaujardière, J.-F., Fan, Y., & Tang, F. 1993, ApJ, 411, 370

Linker, J. A., Van Hoven, G., & Schnack, D. D. 1990, Geophys. Res. Lett., 17, 2281

Linker, J. A., Van Hoven, G., & McComas, D. J. 1992, J. Geophys. Res., 97, 13733

Low, B. C. 1977, ApJ, 212, 234

———. 1981, ApJ, 251, 352

Low, B. C., & Smith, D. F. 1993, ApJ, 410, 412

Mikić, Z., & Morse, E. C. 1985, J. Comput. Phys., 61, 154

Mikić, Z., Barnes, D. C., & Schnack, D. D. 1988, ApJ, 328, 830

Moffatt, H. K. 1985, J. Fluid Mech., 159, 359

Parker, E. N. 1963, Interplanetary Dynamical Processes (New York: Wiley-Interscience)

———. 1972, ApJ, 174, 499

———. 1979, Cosmical Magnetic Fields (Oxford: Clarendon)

———. 1986, Geophys. Ap. Fluid Dyn., 35, 277

Pneuman, G. W., & Kopp, R. A. 1971, Sol. Phys., 18, 258

Porter, L. J., Klimchuk, J. A., & Sturrock, P. A. 1992, ApJ, 385, 738

Priest, E. R. 1981, in Solar Flare Magnetohydrodynamics, ed. E. R. Priest (London: Gordon and Breach), p. 142 and p. 150

———. 1982, Solar Magnetohydrodynamics (Dordrecht: Reidel)

———. 1988, ApJ, 328, 848

Priest, E. R., & Milne, A. M. 1980, Sol. Phys., 65, 315

Priest, E. R., & Forbes, T. G. 1990, Sol. Phys., 126, 319

Raadu, M. A. 1972, Sol. Phys., 22, 425

Roumeliotis, G., Sturrock, P. A., & Antiochos, S. 1993, ApJ, (submitted)

Schnack, D. D., Barnes, D. C., Mikić, Z., Harned, D. S., & Caramana, E. J. 1987, J. Comput. Phys., 70, 330

Steinolfson, R. S. 1991, ApJ, 382, 677

Sturrock, P. A. 1991, ApJ, 380, 655

Vainshtein, S. I., & Parker, E. N. 1986, ApJ, 304, 821

Vainshtein, S. I. 1987, Soviet Phys. JETP, 65, 1154

Wolfson, R., & Low, B. C. 1992, ApJ, 391, 353

Wolfson, R. 1993, ApJ, (to appear Dec. 10)

Wu, S. T., Song, M. T., Martens, P. C. H., & Dryer, M. 1991, Sol. Phys., 134, 353

Yang, W.-H., Sturrock, P. A., & Antiochos, S. K. 1986, ApJ, 309, 383

Zwingmann, W. 1987, Sol. Phys., 111, 309

FIGURE CAPTIONS

Fig. 1.—Radially symmetric profiles of pressure p, mass density ρ, and temperature T, in the initial hydrostatic equilibrium. The base values at $r = R_0$ are given in the text.

Fig. 2.—The mesh cells for a typical calculation. The upper radial boundary is at $r = 50R_0$. The inset shows the detail of the mesh near the solar surface.

Fig. 3.—The normalized longitudinal shear velocity profile $v_\phi{}^0$ that is applied at the photosphere.

Fig. 4.—A three-dimensional view of the sheared magnetic field lines for $\Delta s_{max} = 1.6R_0$. At $t = 0$, in the dipole field, the selected field lines lie in the $(r-\theta)$ plane.

Fig. 5.—Evolution of the projected field lines (contours of constant flux ψ) in the ideal MHD case. The applied shear at the times indicated in the sequence (a)–(f) is $\Delta s_{max} = 0$, 1.0, 1.4, 1.8, 2.0, and $2.0R_0$. (The shear flow is turned off at $t = 520\tau_A$.) The field lines in the initial dipole field are shown in (a). Note the sensitivity of the field line height to shear as Δs_{max} approaches $1.8R_0$. The contour values in this and all subsequent ψ-plots correspond to 19 uniformly spaced values between $0.05\psi_0$ and $0.95\psi_0$, inclusive, where $\psi_0 = B_0R_0{}^2$ is the maximum flux.

Fig. 6.—Evolution of the projected field lines during the resistive MHD case. The reconnection of field lines creates an O-point in the flux and ejects a

plasmoid.

Fig. 7.—Contours of the longitudinal component of the electric current density J_ϕ at $t = 549.3\tau_A$, corresponding to the flux contours shown in Fig. 6*d* for the resistive case. A current sheet appears at the equator, with a maximum current density equal to $31.2(cB_0/4\pi R_0)$.

Fig. 8.—Detail of the reconnection region at $t = 549.3\tau_A$, showing the poloidal projection of the flow vectors, with the field lines superimposed. The maximum flow speed approaches 600 km s^{-1}.

Fig. 9.—Evolution of the magnetic energy W for the ideal and resistive MHD cases. The shear flow is turned off at $t = 520\tau_A$. In the resistive case, reconnection dissipates a large fraction of the free magnetic energy. In contrast, in the ideal case the magnetic energy changes little after the shear is turned off. The solid symbols and open circles indicate the values of time at which the flux is shown in Figs. 5 and 6, respectively.

Fig. 10.—Evolution of the kinetic energy K for the ideal and resistive MHD cases. The shear flow is turned off at $t = 520\tau_A$. The kinetic energy increases considerably during the reconnection. The solid symbols and open circles indicate the values of time at which the flux is shown in Figs. 5 and 6, respectively.

Fig. 11.—Comparison of the computed and exact longitudinal field line footpoint displacements at the end of the ideal MHD run at $t = 900\tau_A$. The solid line shows the exact footpoint displacements expected from the applied flow profile; the symbols denote the displacements computed by tracing

individual field lines. The agreement shows that the line-tied boundary conditions have been implemented accurately.

Fig. 12.—Contours of the flux ψ for ideal force-free MHD equilibria as a function of applied shear. The outer field lines open when $\Delta s_{max} \gtrsim 2.0 R_0$.

Fig. 13.—Contours of the longitudinal component of the electric current density J_ϕ corresponding to the flux contours shown in Fig. 12 for ideal force-free MHD equilibria. The maximum is expressed in units of the normalizing current density, $cB_0/4\pi R_0$. A current sheet appears when $\Delta s_{max} \gtrsim 2.0 R_0$.

Fig. 14.—Radial magnetic field B_r in the force-free field with $\Delta s_{max} = 2.2 R_0$ (corresponding to Figs. 12*f* and 13*f*) at $r = 3R_0$, showing that B_r approaches a function which has a discontinuity at the equator $\theta = 90°$. This is the location of the current sheet in the open field. The symbols show the locations of the θ mesh points.

Fig. 15.—Comparison of the projected field lines (contours of the flux ψ) for (*a*) the force-free field with shear $\Delta s_{max} = 2.2 R_0$, and (*b*) the open field configuration. The force-free field corresponds to a *partially open* field, with a small fraction of closed low-lying field lines near the equator. The contour values are the same in both plots, and correspond to the usual 19 uniformly spaced values of ψ; a contour at $\psi = 0.98\psi_0$ has been added in both plots to emphasize the closed field lines in (*a*).

Fig. 16.—Height of selected field lines in the ideal MHD equilibria as a function of the applied shear. The field lines are labeled by the corresponding flux value ψ, in terms of the maximum flux ψ_0. The field line height rises

sharply as the critical shear ($\Delta s_{max} \sim 1.8R_0$) is approached. For $\Delta s_{max} \gtrsim 2.0R_0$, as the field opens, the higher field lines (with $\psi = 0.95$, 0.9, and $0.8\psi_0$) are characterized by $h \to \infty$.

Fig. 17.—Magnetic energy W of force-free equilibria as a function of applied shear Δs_{max}. Note that W approaches the open-field energy for large shear, but that the field opens while W is still below W_{open} (at $\Delta s_{max} = 2.0$ and $2.2R_0$). The error bars indicate uncertainties in W since the indicated states are not in a complete steady state.

Fig. 18.—Evolution of the "partial magnetic energies" W_r, W_θ, and W_ϕ, which are defined as the energies in the r, θ, and ϕ components of the magnetic field, for the case $\Delta s_{max} = 2.0R_0$. The shear flow is turned off at $t = 1050\tau_A$.

Fig. 19.—Evolution of the magnetic energy W and the surface term in the virial theorem comparison for the case $\Delta s_{max} = 2.0R_0$. The two curves match closely during the quasi-static evolution. The magnified view in the inset shows that the curves depart when magnetic nonequilibrium occurs. The subsequent equilibration occurs over a long time scale. The "bump" in the surface term at $t \sim 1600\tau_A$ occurs when the expanding upper field lines reach the upper radial boundary.

Fig. 20.—Evolution of the height of selected field lines at the equator ($\theta = 90°$) for the case $\Delta s_{max} = 2.0R_0$. The field lines are labeled by the corresponding flux value ψ, in terms of the maximum flux ψ_0. The shear flow is ramped down to zero starting at $t = 1000\tau_A$ and ending at $t = 1050\tau_A$,

with zero flow thereafter. When the critical shear is exceeded the upper field lines rise to large heights as the field begins to open. The slow asymptotic rise of the upper field lines indicates a long equilibration time. The evolution of the low field lines indicates that there is a closed-field region in the resulting partially open field.

Fig. 21.—Evolution of the magnetic energy W and the surface term in the virial theorem comparison for the case $\Delta s_{max} = 1.8R_0$. The magnified view in the inset shows that the curves remain close at all times, indicating quasi-static evolution, in contrast with the case when the critical shear is exceeded (Fig. 19).

Fig. 22.—Evolution of field line height for the case $\Delta s_{max} = 1.8R_0$. When the shear flow is ramped down to zero, starting at $t = 900\tau_A$ and ending at $t = 950\tau_A$, the field lines equilibrate quickly, in contrast to the behavior observed when the critical shear is exceeded (Fig. 20).

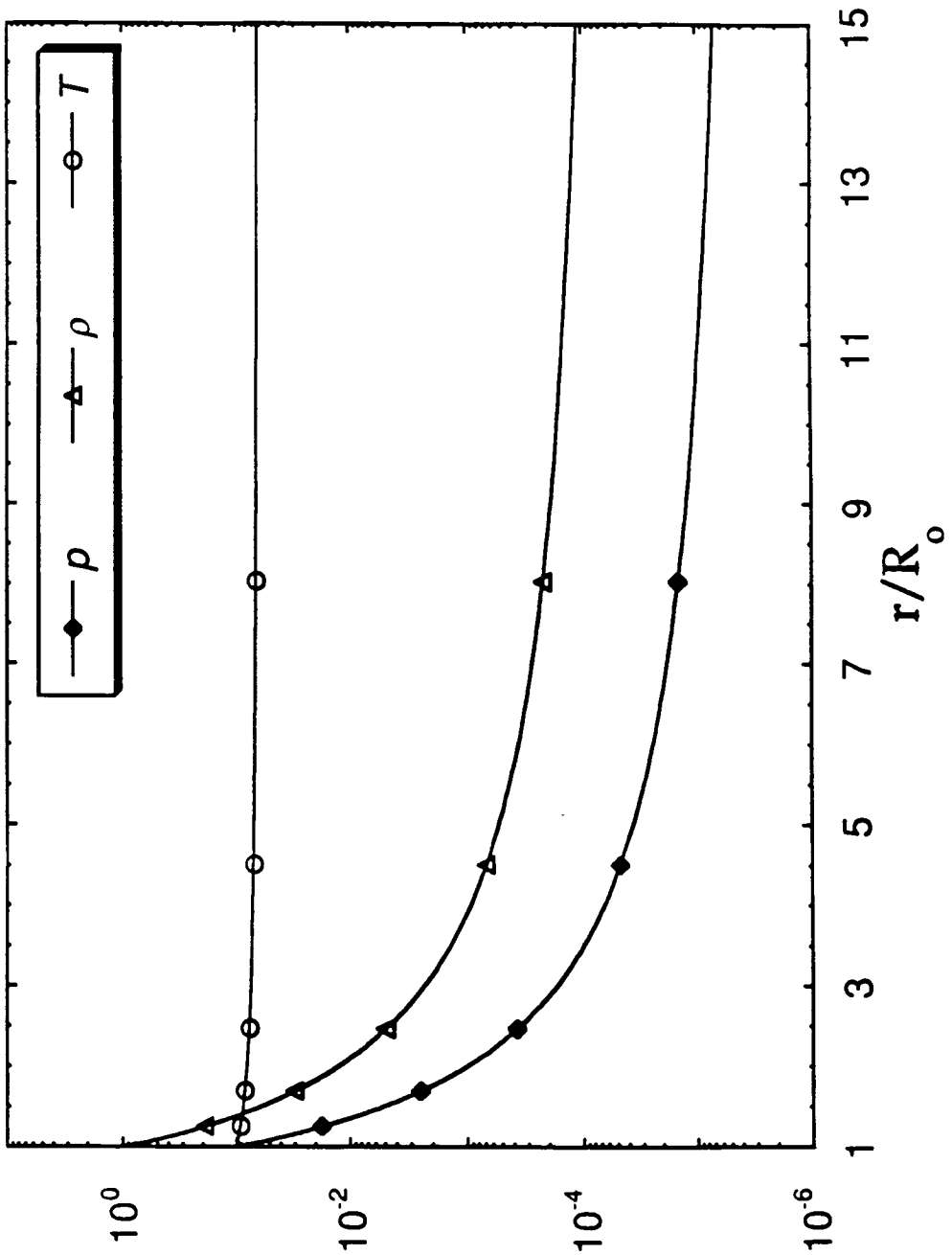

Fig. 1

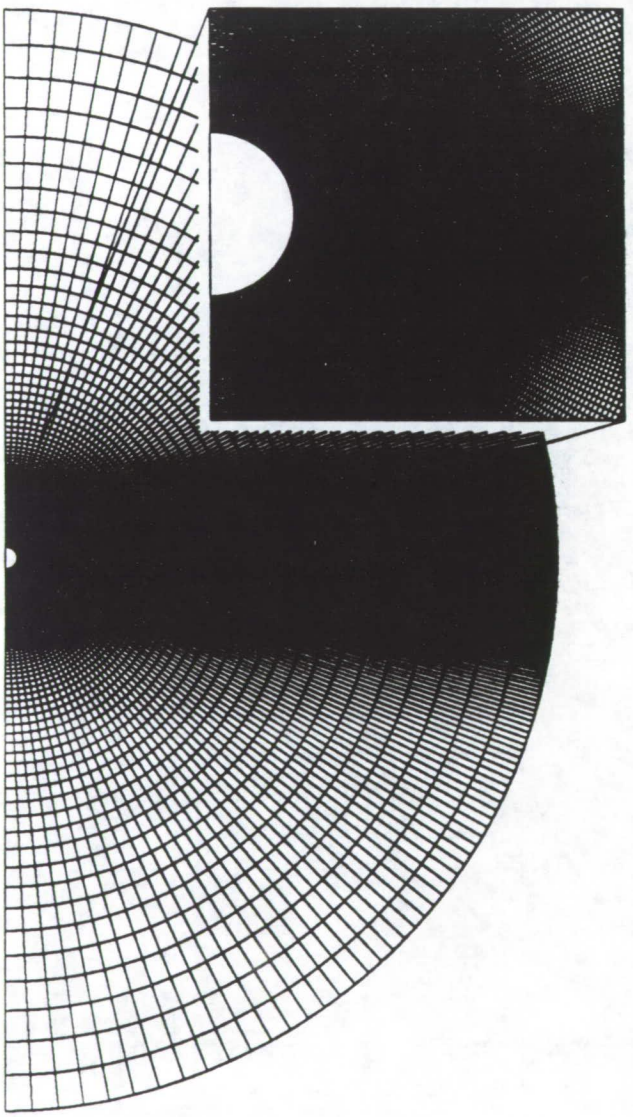

Fig. 2

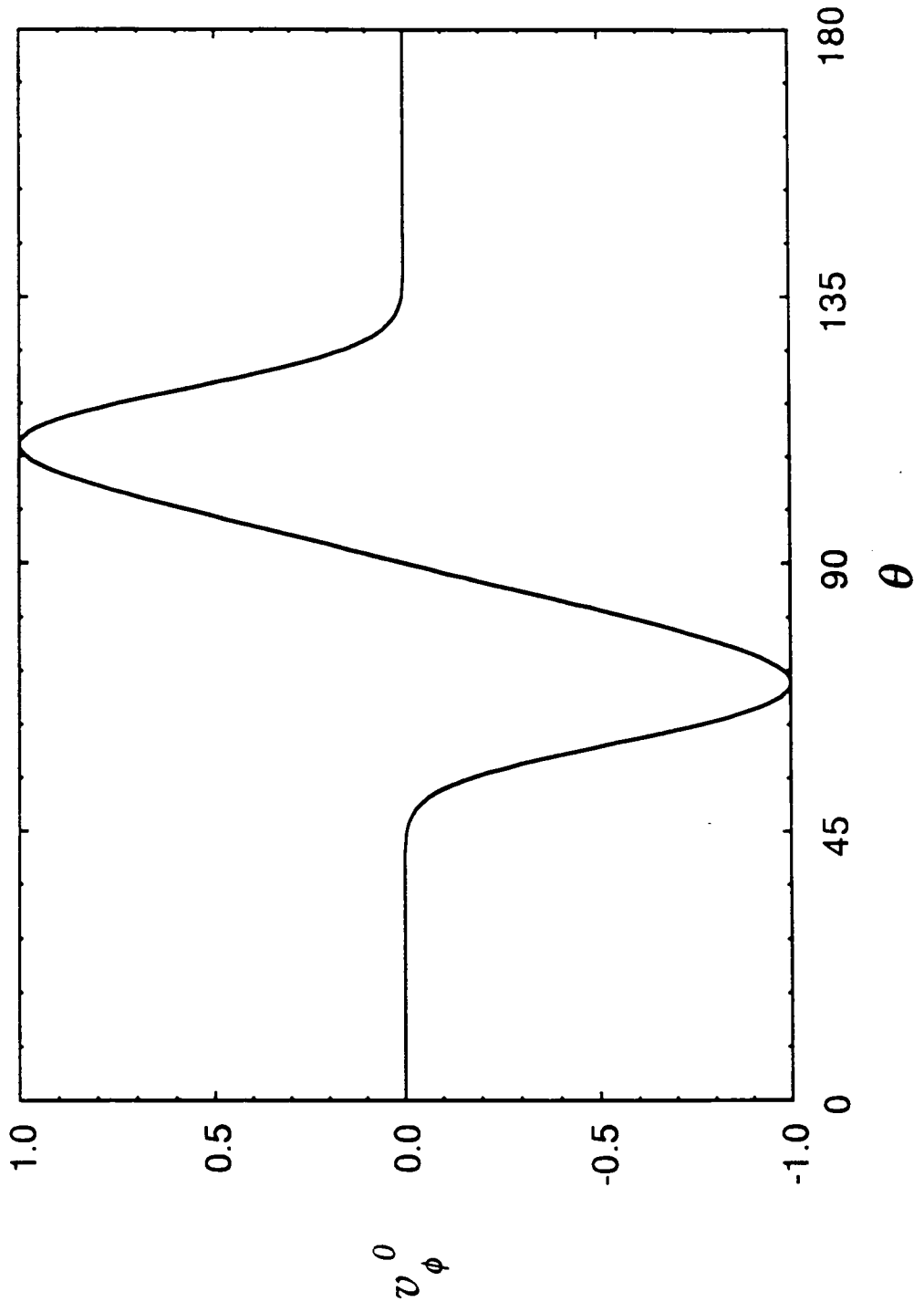

Fig. 3

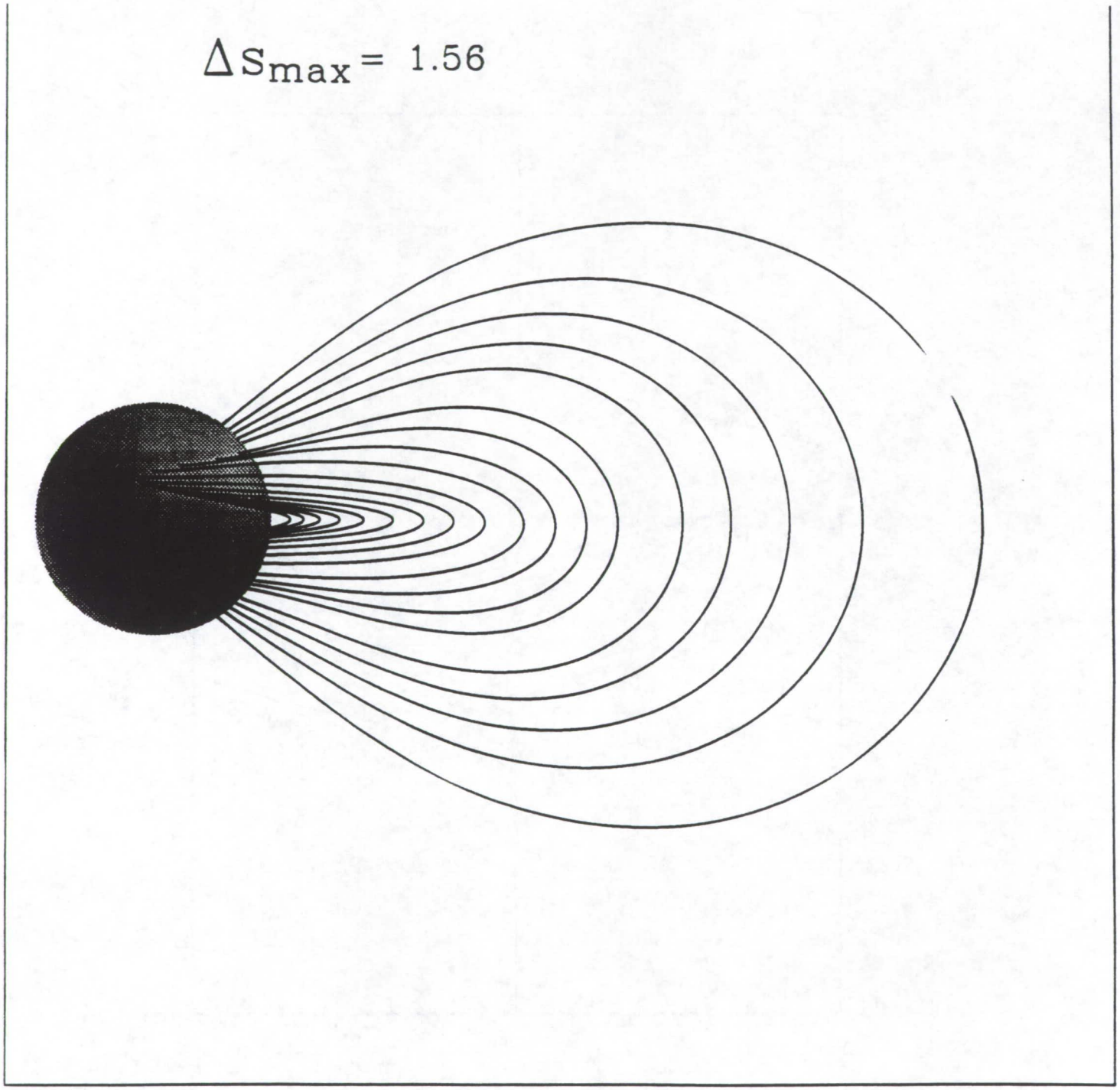

Fig. 4

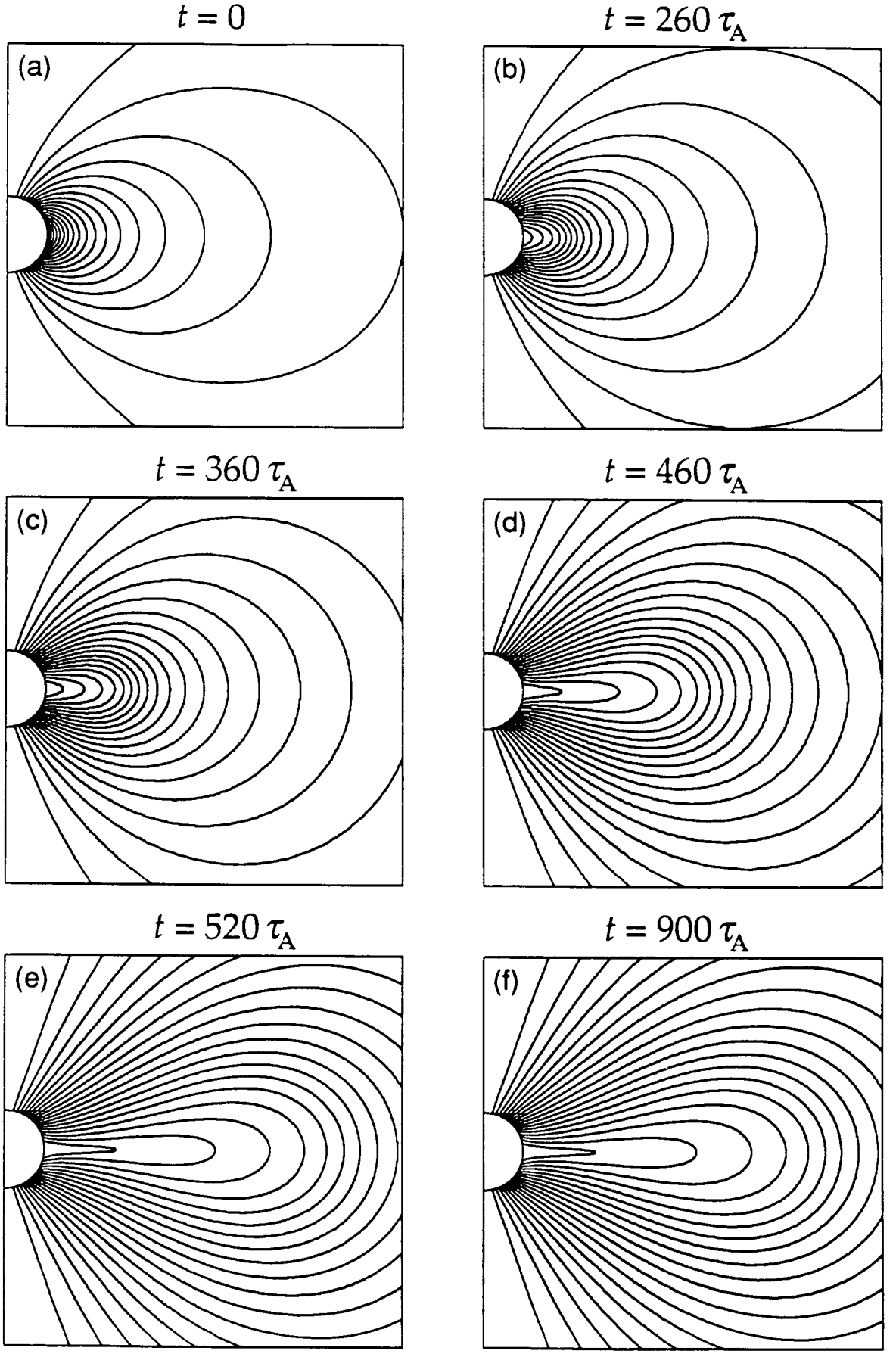

Fig. 5

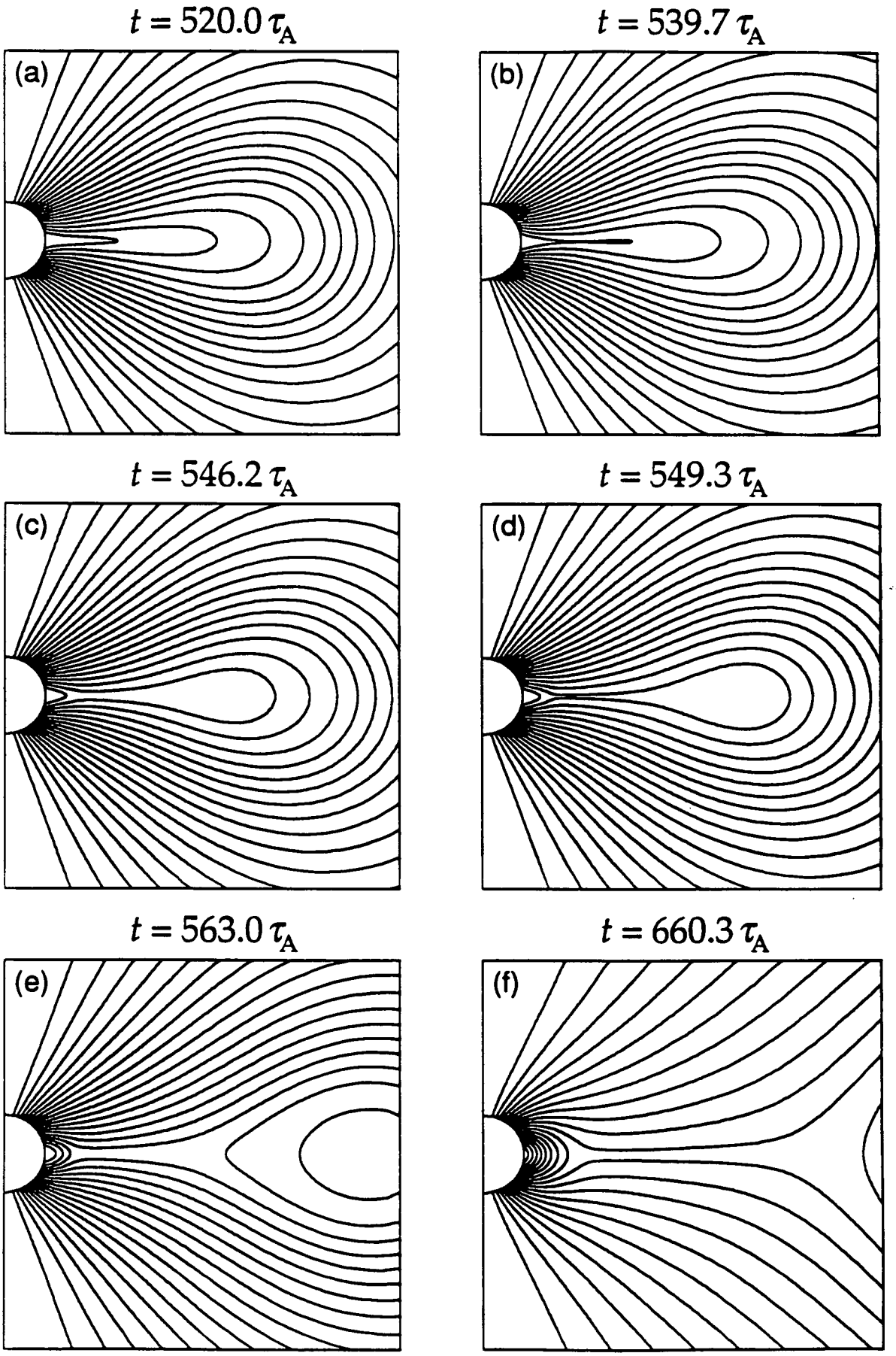
$t = 520.0\,\tau_A$
(a)
$t = 539.7\,\tau_A$
(b)
$t = 546.2\,\tau_A$
(c)
$t = 549.3\,\tau_A$
(d)
$t = 563.0\,\tau_A$
(e)
$t = 660.3\,\tau_A$
(f)

Fig. 6

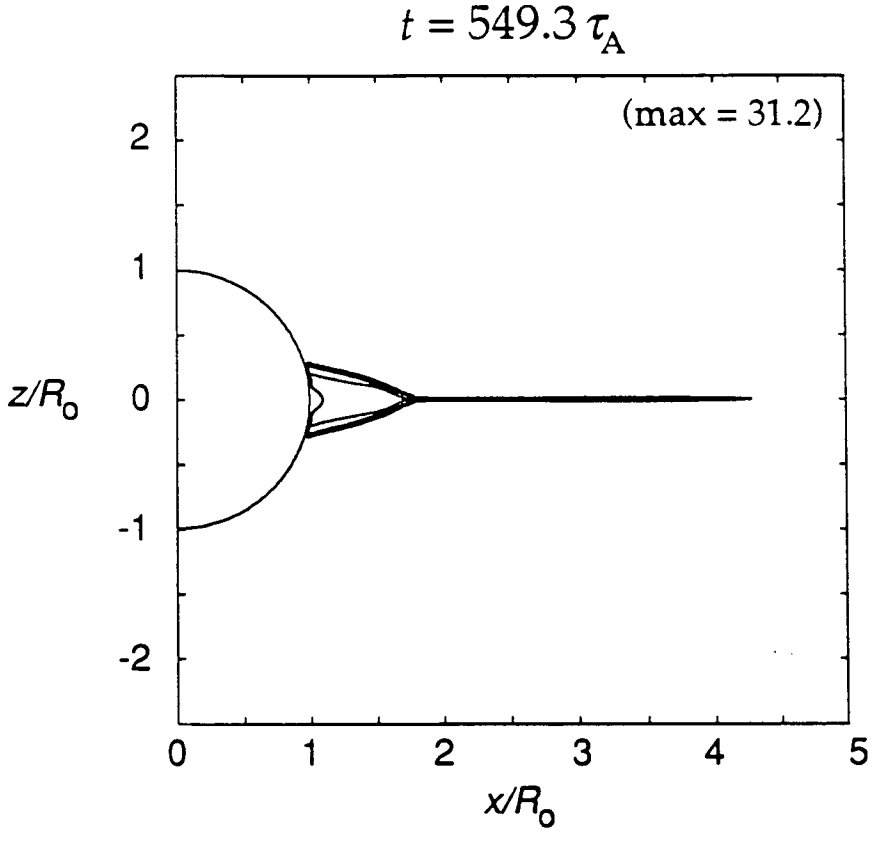

Fig. 7

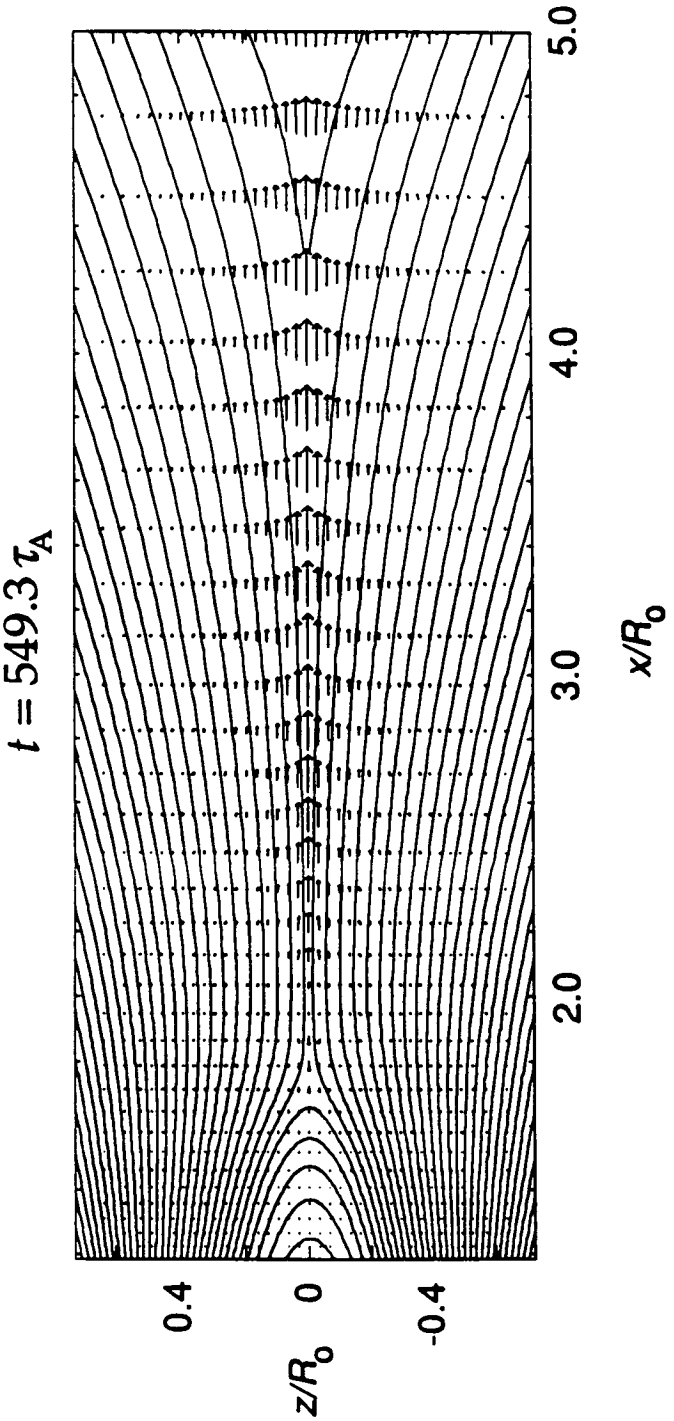

Fig. 8

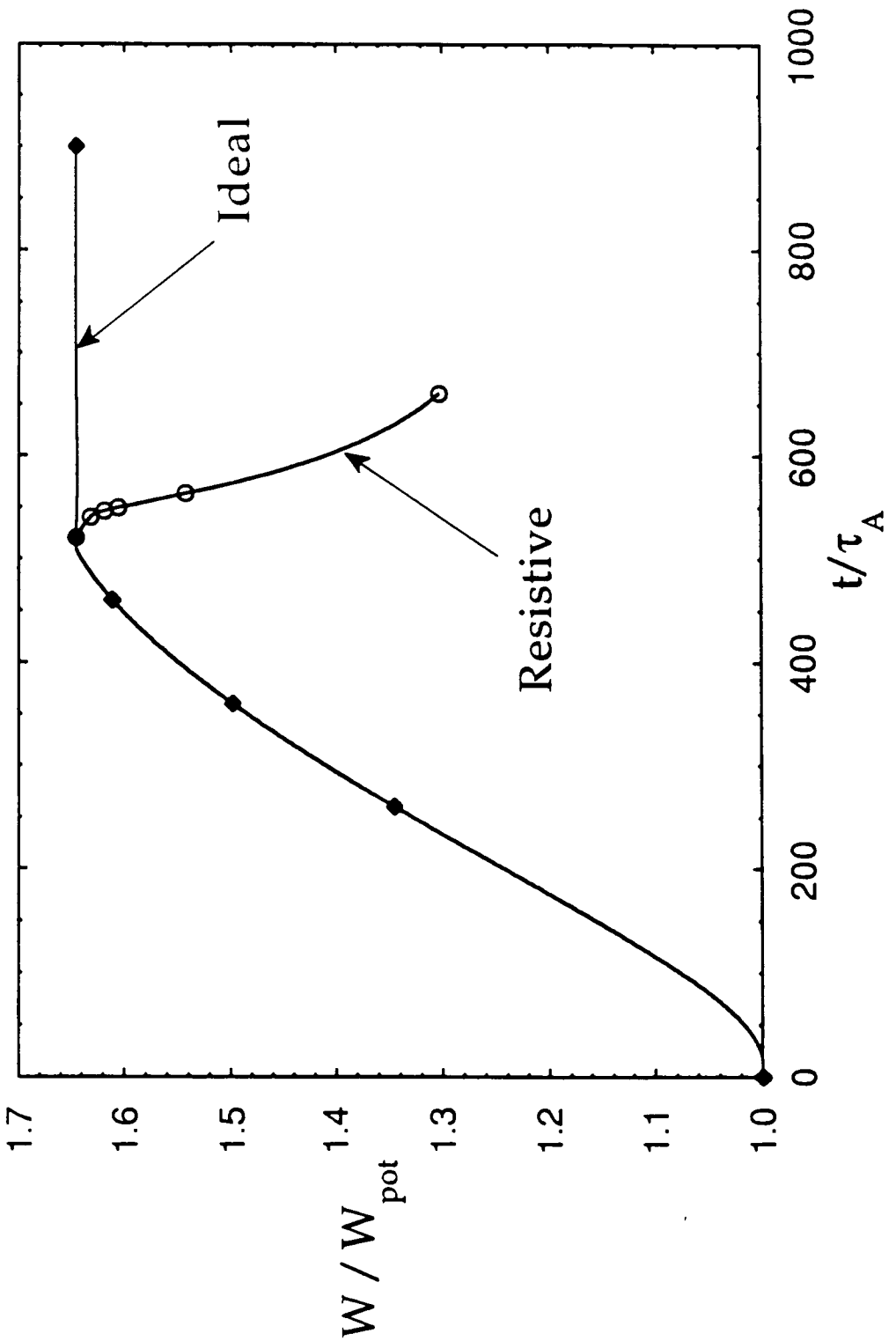
Ideal
Resistive
W / W pot
t/τ A
1.7
1.6
1.5
1.4
1.3
1.2
1.1
1.0
0
200
400
600
800
1000

Fig. 9

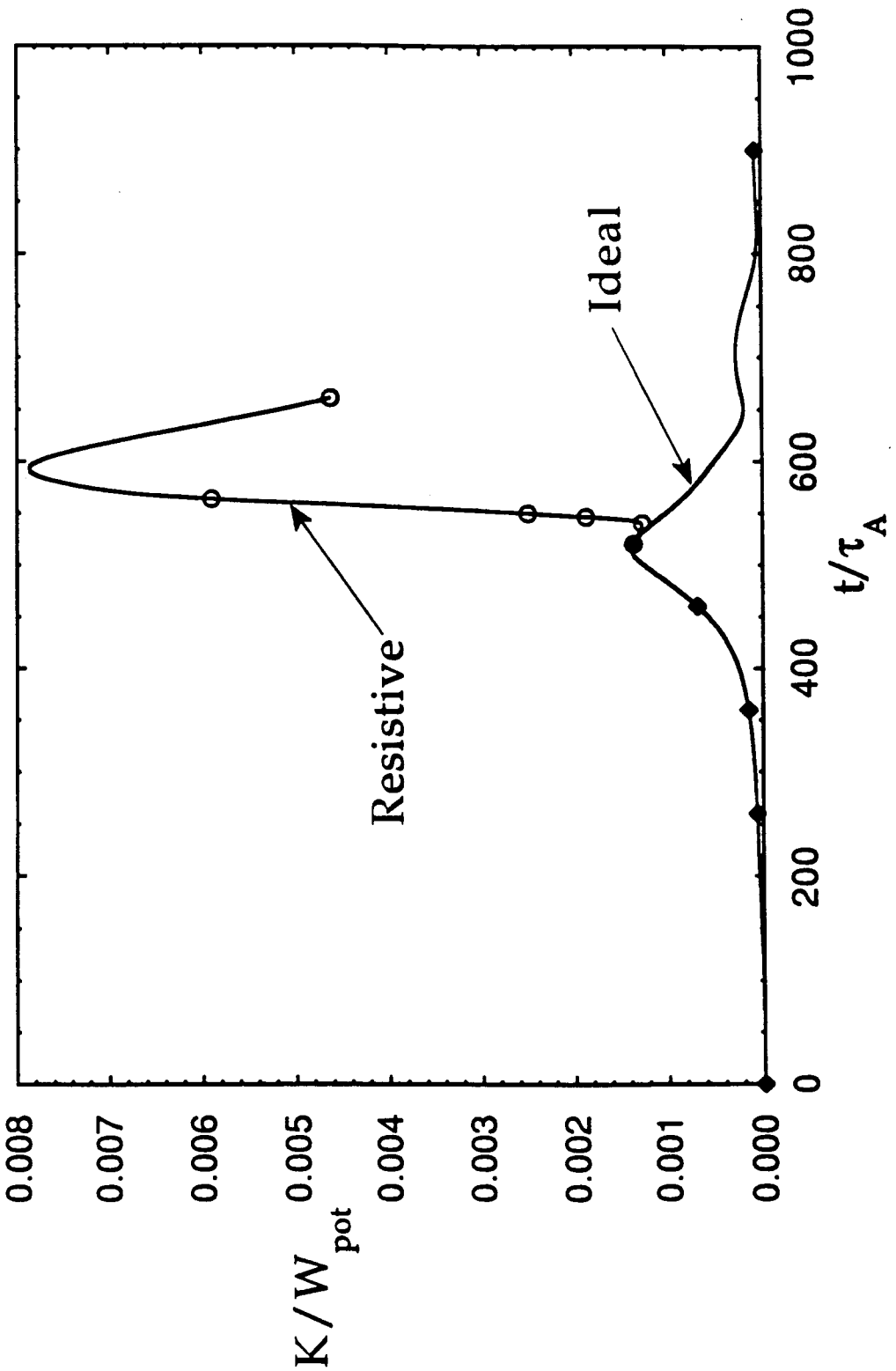
0.008
0.007
0.006
0.005
0.004
0.003
0.002
0.001
0.000
K / W pot
0
200
400
600
800
1000
t/τA
Resistive
Ideal

Fig. 10

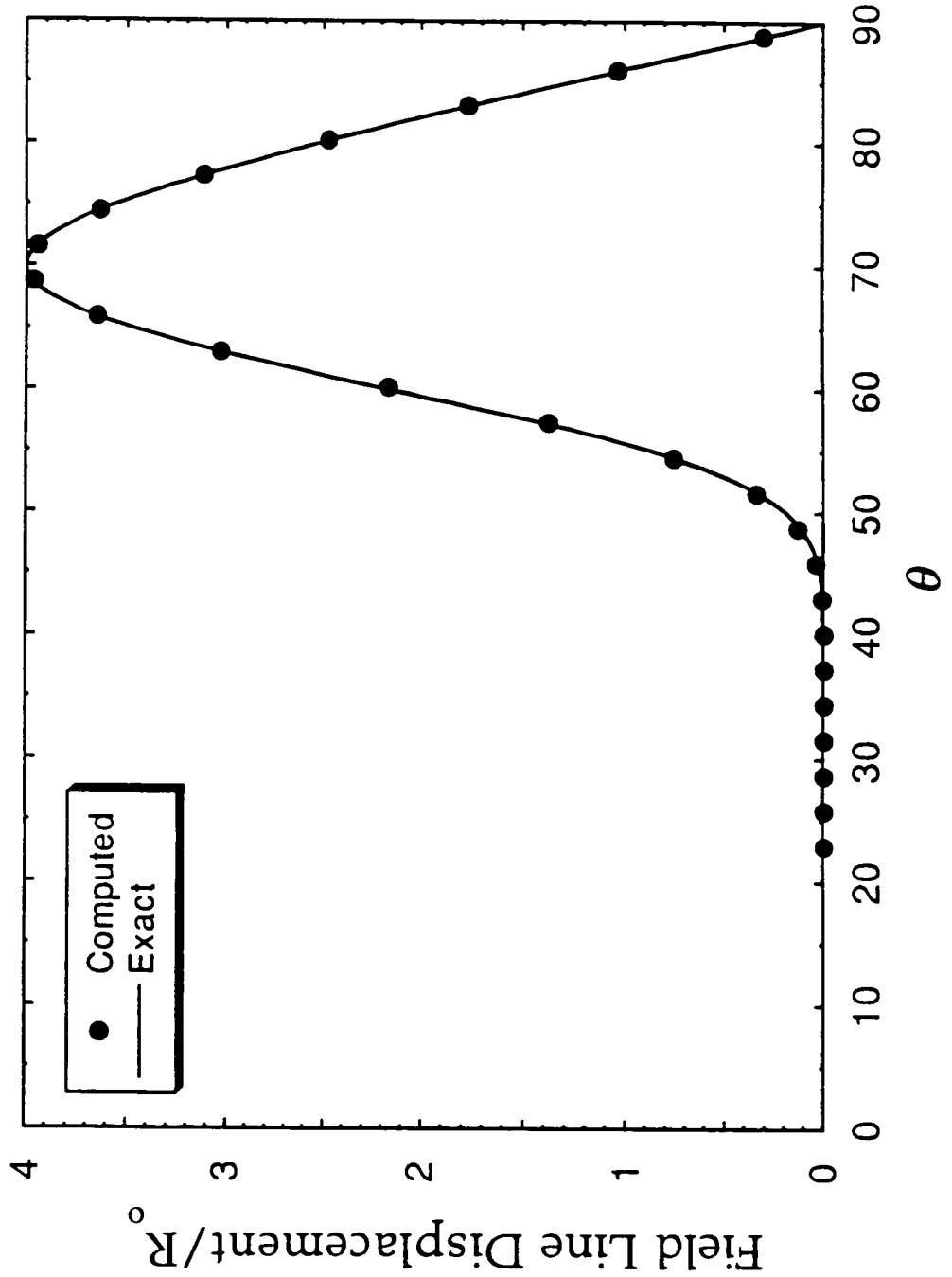
Field Line Displacement/R$_o$
θ
Computed
Exact
0
1
2
3
4
0
10
20
30
40
50
60
70
80
90

Fig. 11

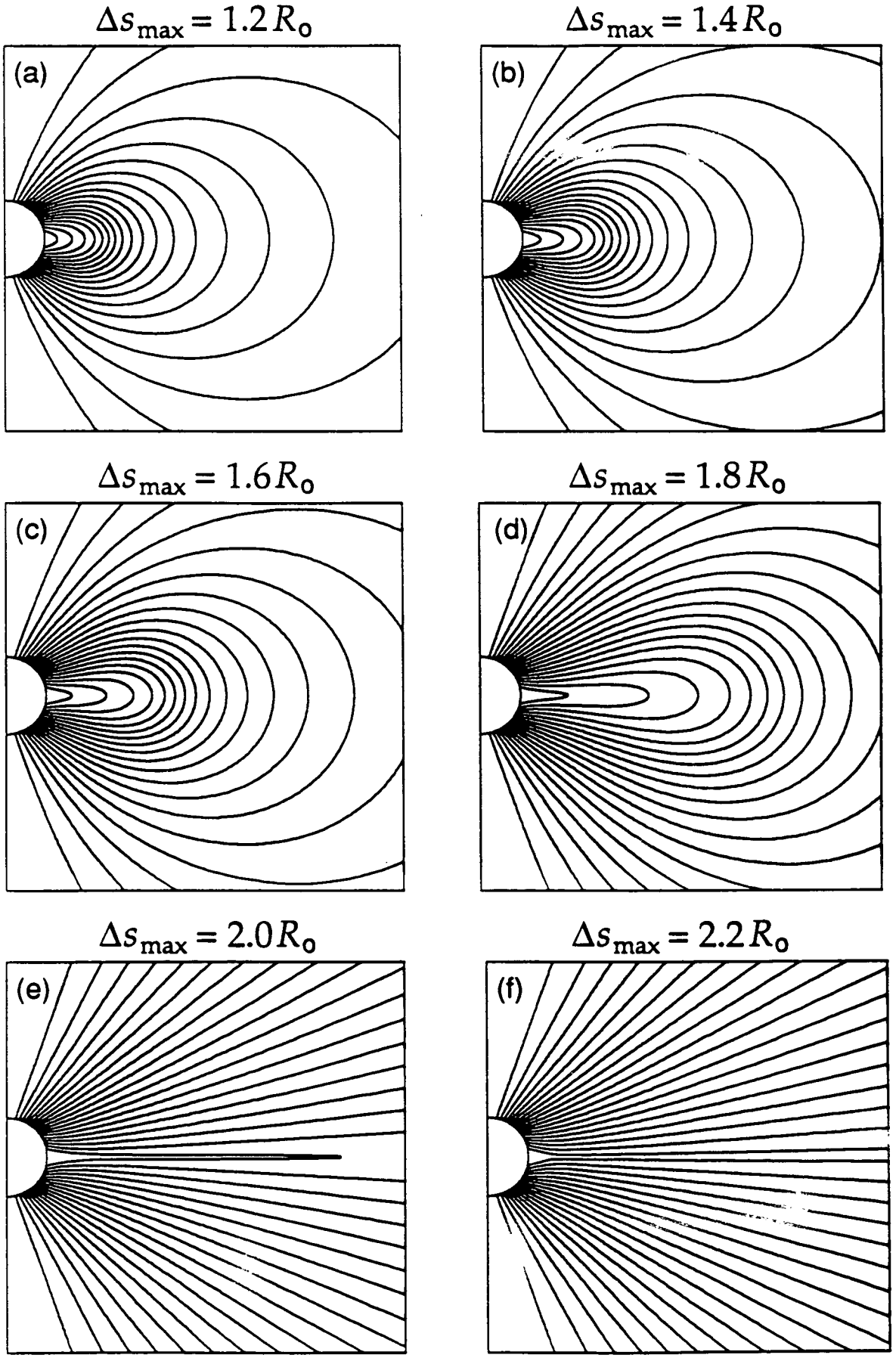
$\Delta s_{max} = 1.2 R_o$
(a)
$\Delta s_{max} = 1.4 R_o$
(b)
$\Delta s_{max} = 1.6 R_o$
(c)
$\Delta s_{max} = 1.8 R_o$
(d)
$\Delta s_{max} = 2.0 R_o$
(e)
$\Delta s_{max} = 2.2 R_o$
(f)

Fig. 12

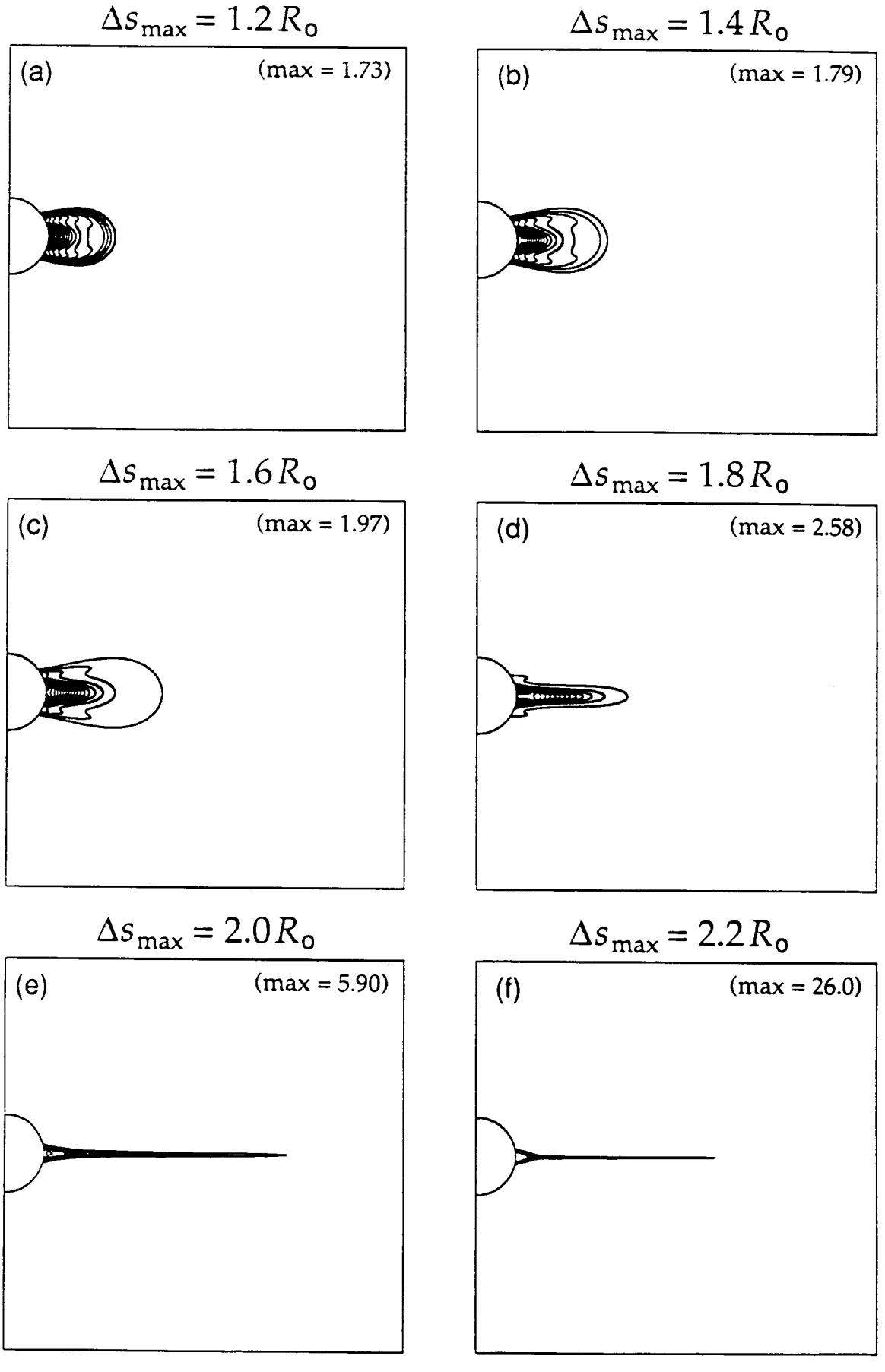
$\Delta s_{max} = 1.2 R_o$
(a)
(max = 1.73)
$\Delta s_{max} = 1.4 R_o$
(b)
(max = 1.79)
$\Delta s_{max} = 1.6 R_o$
(c)
(max = 1.97)
$\Delta s_{max} = 1.8 R_o$
(d)
(max = 2.58)
$\Delta s_{max} = 2.0 R_o$
(e)
(max = 5.90)
$\Delta s_{max} = 2.2 R_o$
(f)
(max = 26.0)

Fig. 13

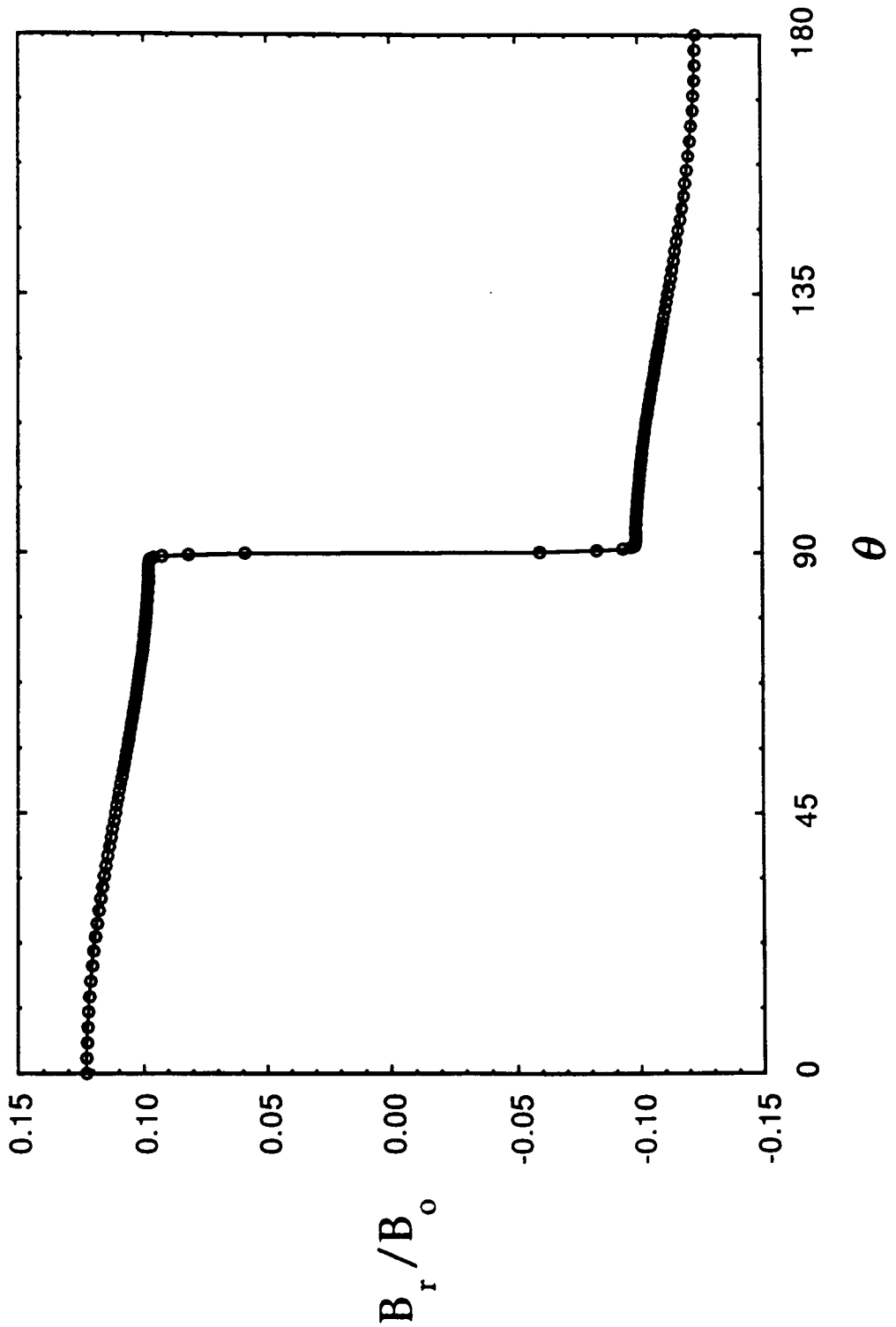

Fig. 14

$\Delta s_{max} = 2.2 R_o$

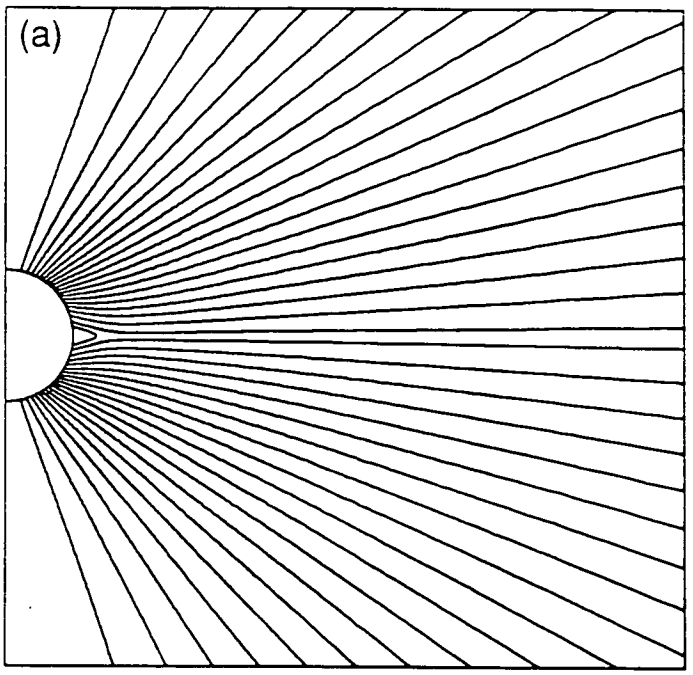

Open Field

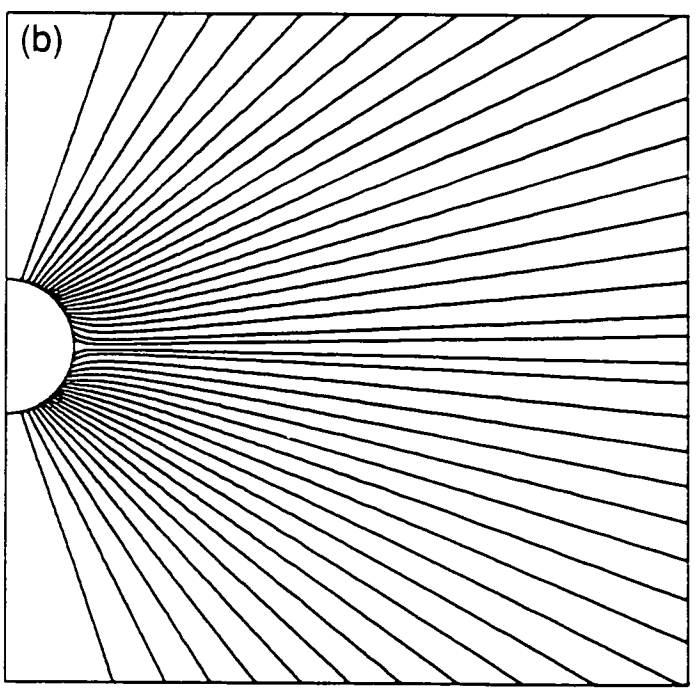

Fig. 15

C-2

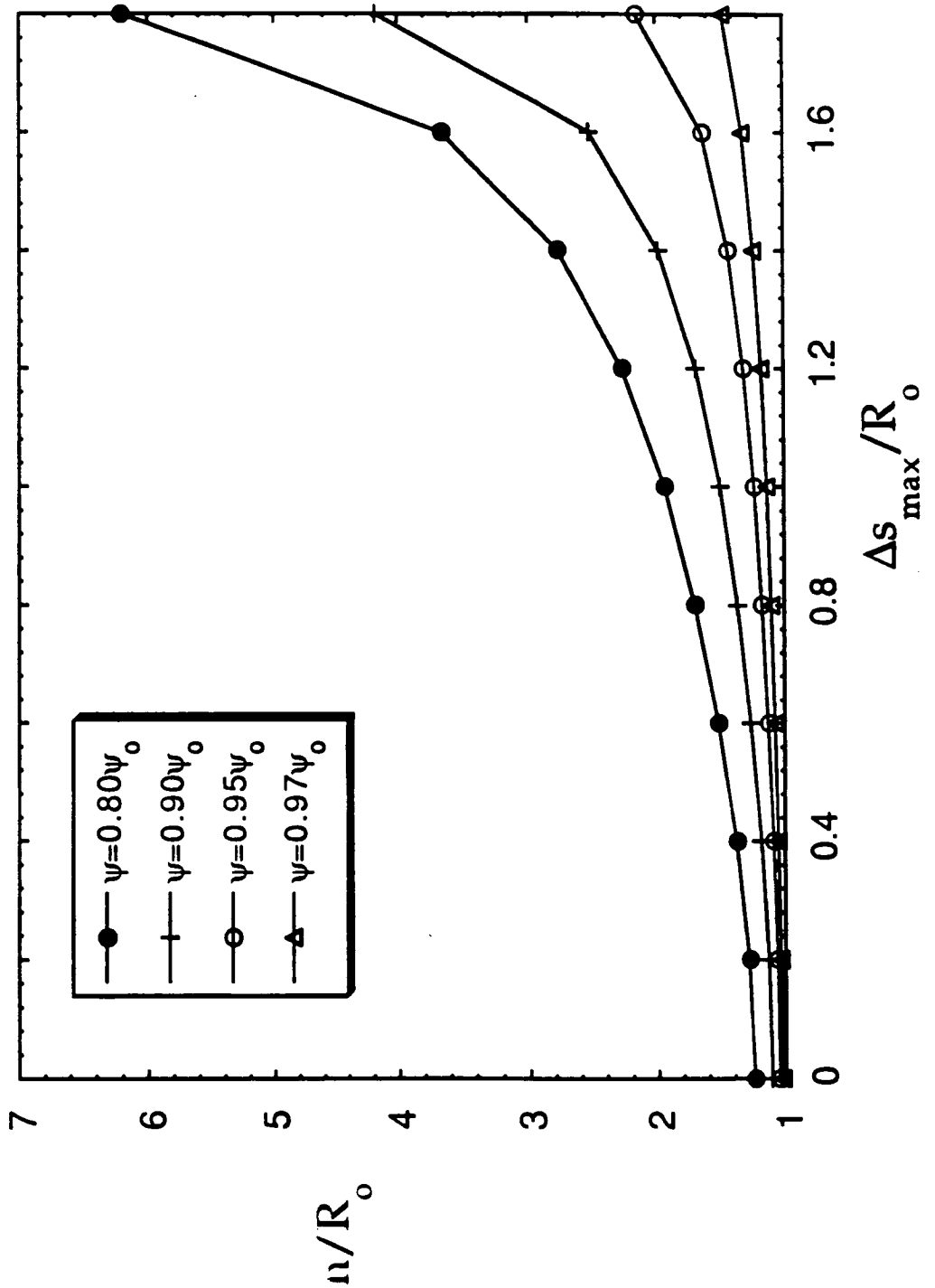
ψ=0.80ψo
ψ=0.90ψo
ψ=0.95ψo
ψ=0.97ψo
r/Ro
Δsmax/Ro
0
0.4
0.8
1.2
1.6
1
2
3
4
5
6
7

Fig. 16

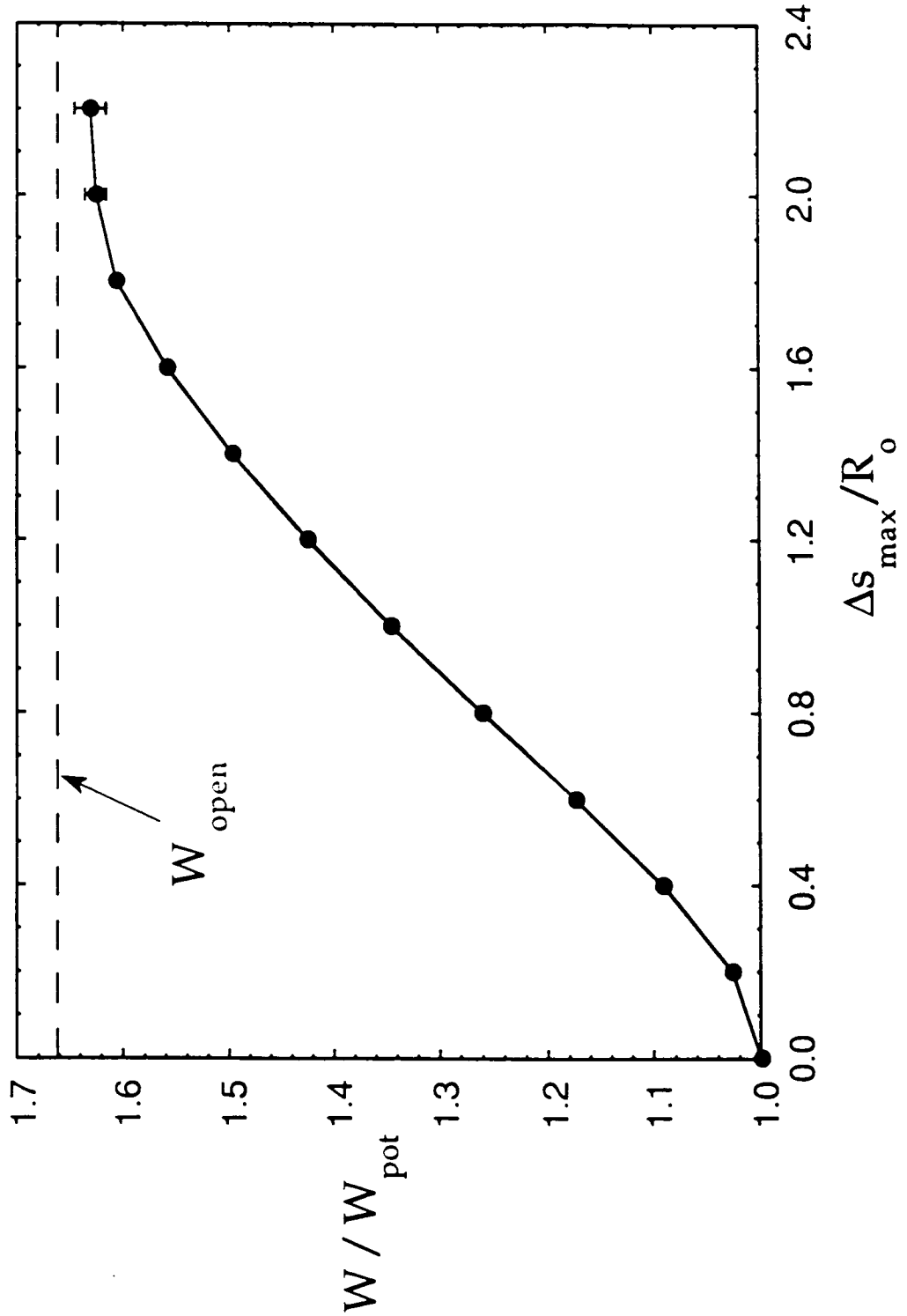

Fig. 17

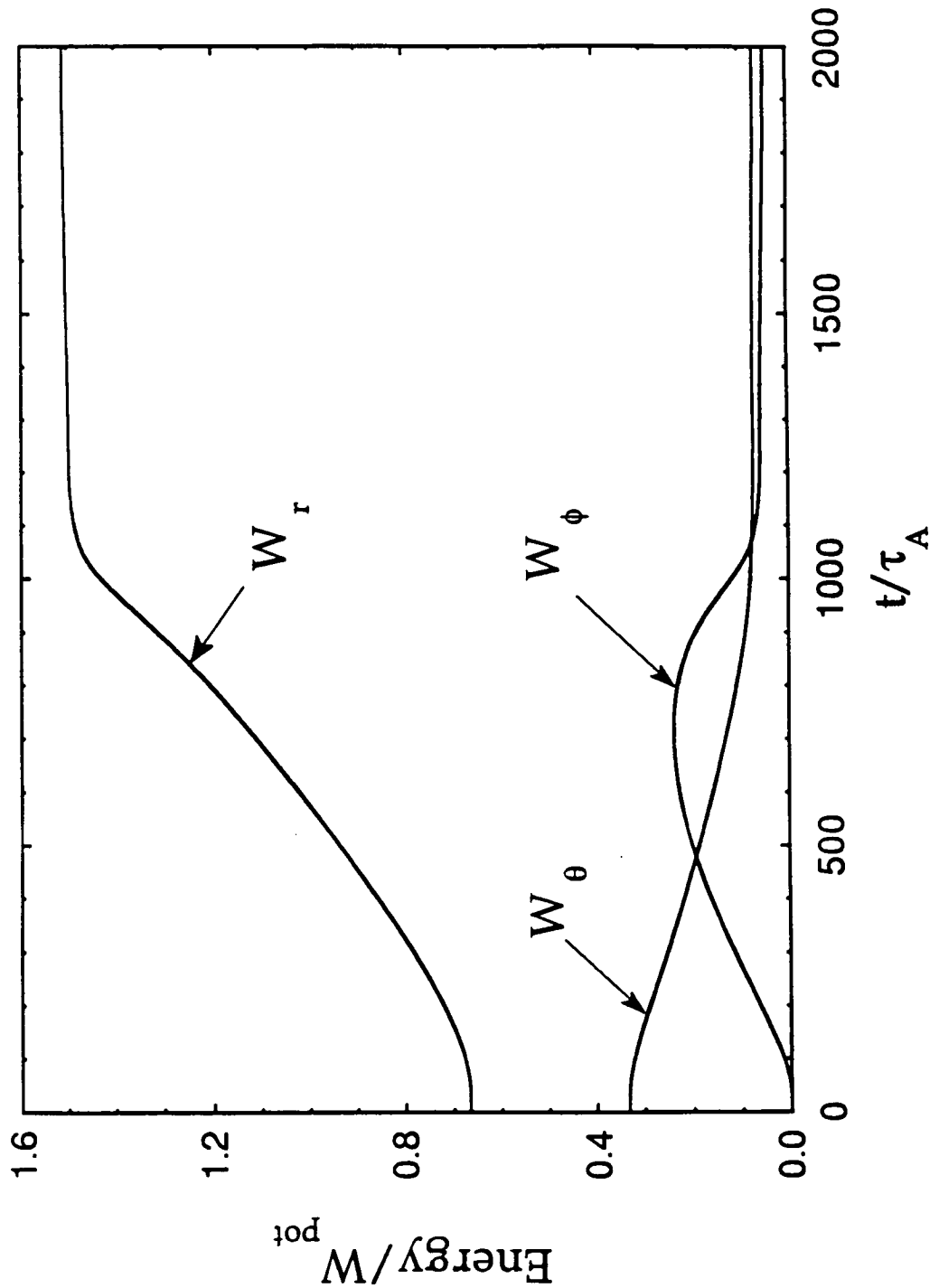

Fig. 18

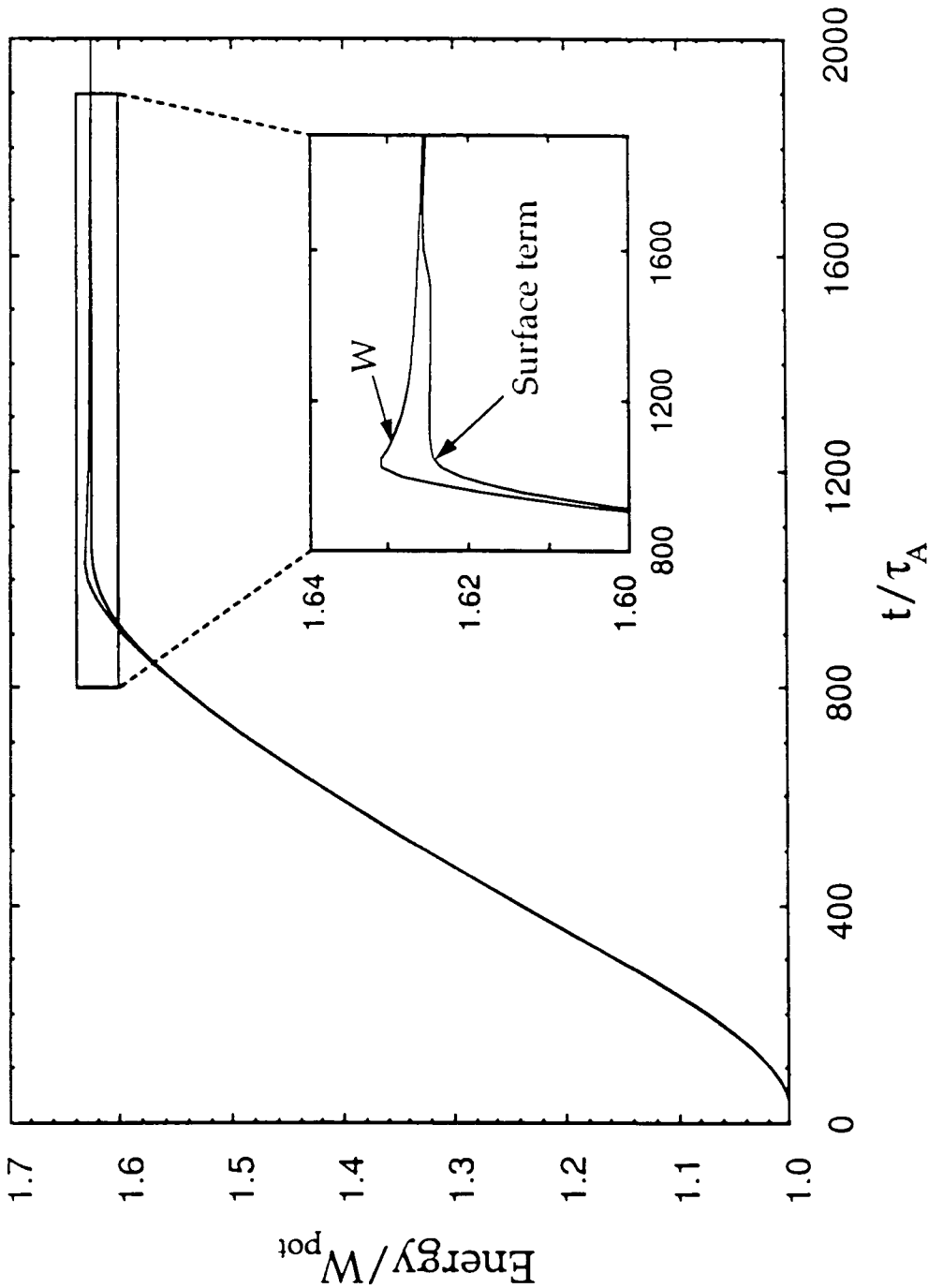
Energy/W_pot
t/τ_A
W
Surface term
1.7
1.6
1.5
1.4
1.3
1.2
1.1
1.0
0
400
800
1200
1600
2000
1.64
1.62
1.60
800
1200
1600

Fig. 19

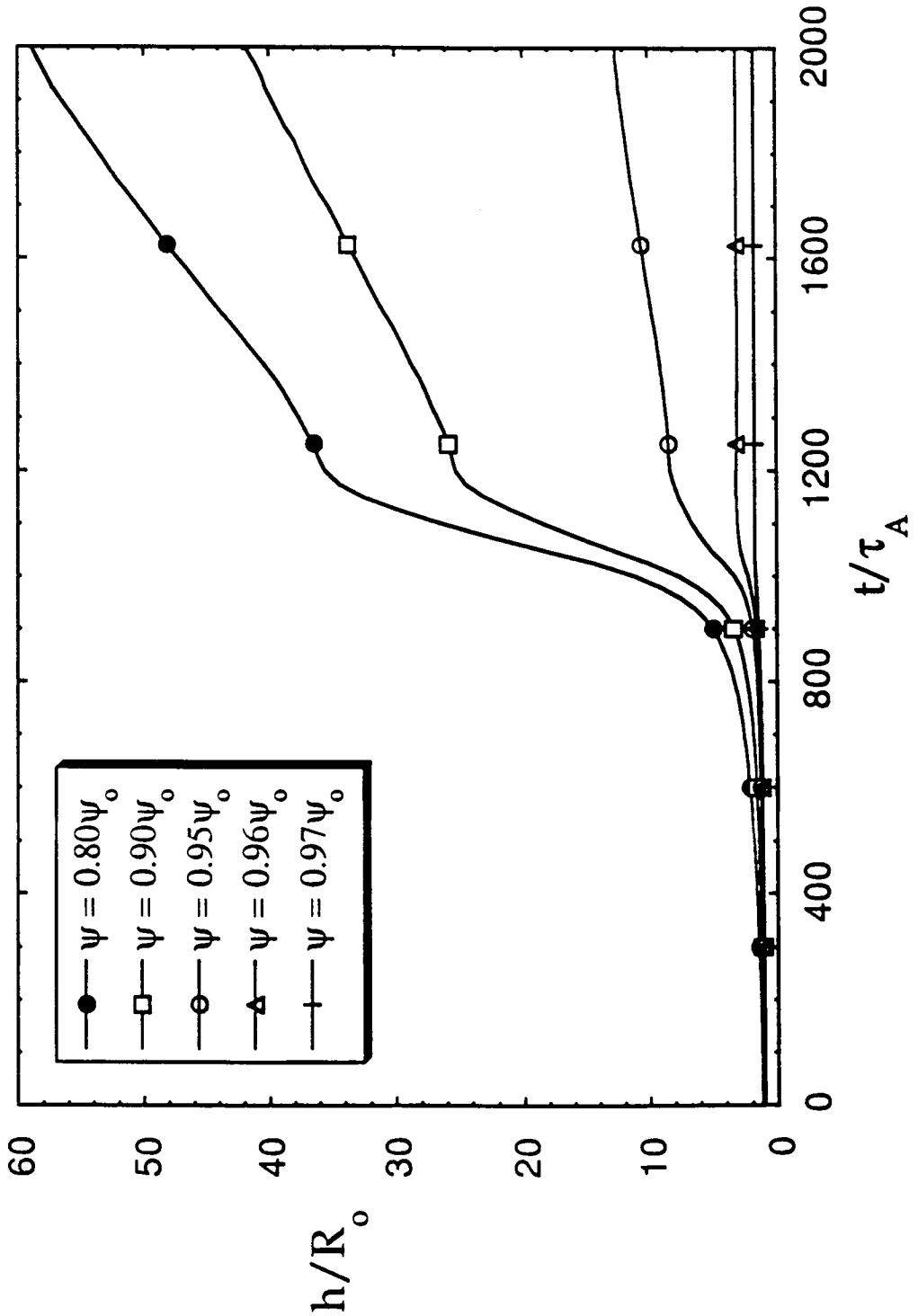
h/R$_o$
t/τ$_A$
0
10
20
30
40
50
60
0
400
800
1200
1600
2000
ψ = 0.80ψ$_o$
ψ = 0.90ψ$_o$
ψ = 0.95ψ$_o$
ψ = 0.96ψ$_o$
ψ = 0.97ψ$_o$

Fig. 20

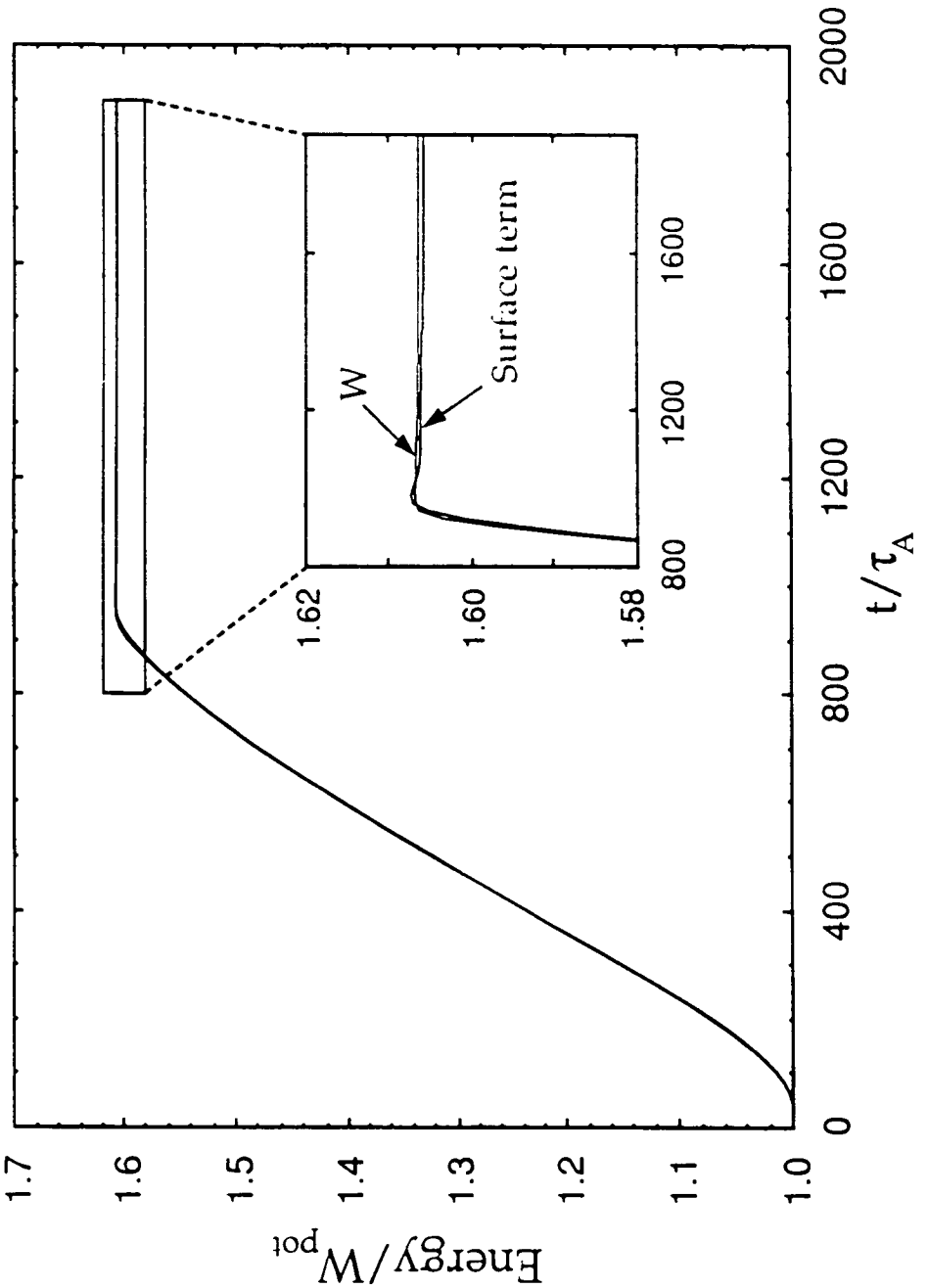
Energy/W$_{pot}$
1.7
1.6
1.5
1.4
1.3
1.2
1.1
1.0
0
400
800
1200
1600
2000
t/τ_A
1.62
1.60
1.58
800
1200
1600
W
Surface term

Fig. 21

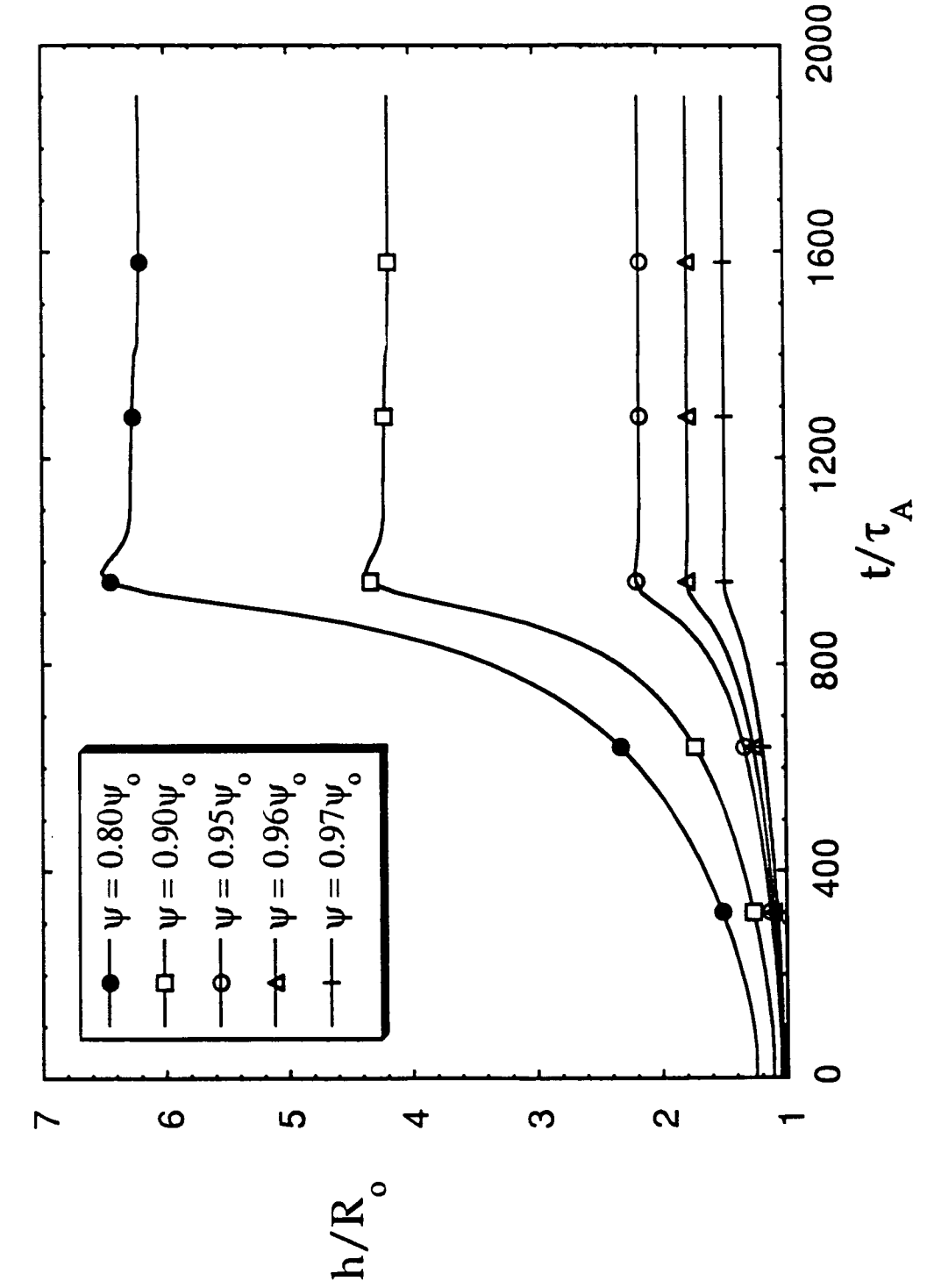
h/R$_o$
t/τ$_A$
ψ = 0.80ψ$_o$
ψ = 0.90ψ$_o$
ψ = 0.95ψ$_o$
ψ = 0.96ψ$_o$
ψ = 0.97ψ$_o$
1
2
3
4
5
6
7
0
400
800
1200
1600
2000

Fig. 22